공학박사학위논문

재사용 무인 우주비행체의 개념설계를 위한 효율적인 다학제간 최적 설계 기법 개발

Development of an Efficient Multidisciplinary Optimization Method for the Conceptual Design of Reusable Unmanned Spacecraft

2023 년 8 월

서울대학교 대학원

기계항공공학부

정 종 호

재사용 무인 우주비행체의 개념설계를 위한 효율적인 다학제간 최적 설계 기법 개발

Development of an Efficient Multidisciplinary Optimization Method for the Conceptual Design of Reusable Unmanned Spacecraft

지도교수 이 관 중

이 논문을 공학박사 학위논문으로 제출함

2023 년 5 월

서울대학교 대학원

기계항공공학부

정 종 호

정종호의 공학박사 학위논문을 인준함

2023 년 6 월

위 원 장 : 김 규 홍

부위원장 : 이 관 중

위 원 : 정 신 규

위 원 : 이 융 교

위 원 : 권 기 범

Abstract

Development of an Efficient Multi-disciplinary Optimization Method for the Conceptual Design of Reusable Unmanned Spacecraft

Jongho Jung
School of Mechanical and Aerospace Engineering
The Graduate School
Seoul National University

This study develops an efficient approach to design reusable unmanned spacecraft, which is in increasing demand in these days. In various analyses for the design, the calculations of the aerodynamic force, heat flux, and motion are conducted by enormous times while the geometry definition, weight estimation, and propulsion analysis are performed by few times. It is because the former calculations are executed for each instance of trajectory. Thus, this study develops an efficient method to adjust the time step for an analysis. The developed method adjust the time step based on the current state. The developed method is applied to the heat-flux calculation for validating the method. The adaptive-time-step method includes a dynamic factor that adjusts the time step between each instance of heat-flux calculation. Under low-heat-flux conditions, the time step using this factor increases, resulting in a decrease of approximately one-tenth in the number of heat-flux

calculations required with over 90% accuracy. Therefore, the efficiency of heat-flux calculation are improved with high accuracy by adopting the adaptively-determined time step according to this dynamic factor.

In addition, a new method that adaptively adjusts the design space by considering the actual solution distribution of a problem is developed to overcome the limitations of conventional design-space adaptation methods that typically assume a normal distribution of solutions, which is rarely the case for real-world problems. To validate the effectiveness of the developed adaptive design-space method, it is applied to nineteen multiobjective test functions that are commonly used to evaluate optimization approaches. The results show that the method adapted the design space to a suitable range where the probability of solution existence is high. Furthermore, the optimization performance achieved using the developed adaptive design-space method is better than that of the conventional methods.

To validate the effectiveness of the developed methods, the efficient methods for heat-flux calculation and adaptive design space were utilized in MDO for reusable unmanned spacecraft. The MDO framework combines a variety of spacecraft analysis technologies, including weight, propulsion, aerothermodynamics, and trajectory analyses. The weight of the spacecraft is predicted using a modified hypersonic aerospace sizing analysis (HASA), while the entry weight is used to estimate the required thrust and weight of engines. Aerodynamic properties are calculated using modified Newtonian theory and Digital DATCOM, and approximate convective-heating equations are used to determine heat-flux. The spacecraft trajectory is modeled using three degree-of-freedom equation of motion. To enable optimization, the MDO is integrated with a multiobjective genetic

algorithm (MOGA). The MDO results demonstrate that the Pareto solutions obtained using the developed method are superior to those obtained using conventional methods.

Data mining is also conducted with analysis of variance (ANOVA), parallel chart, and self-organizing map (SOM) to investigate why the optimized shapes exhibited superior performance by extracting geometric features that impact the performance of the unmanned spacecraft. The data mining results indicated a trade-off relationship between weight and heat flux. Additionally, the nose radius, total length, and root chord were identified as significant variables for spacecraft performance.

Keywords : Reusable unmanned spacecraft, Conceptual design, Multidisciplinary optimization (MDO), Multiobjective genetic algorithms (MOGA), Time step adaptation, Design-space adaptation

Student Number : 2017-38109

Table of Contents

Nomenclature

English symbols

a	Parameter of adaptive time step for heat-flux calculation
A_j	Probability densities of the jth subspace for the control distribution
AR	Aspect ratio
b	Parameter of adaptive time step for heat-flux calculation
C	Factor for adaptive time step
C_m	Moment coefficients
C_{p}	Pressure coefficients
$C_{p_{max}}$	Maximum value of the pressure coefficient
D_{be}	Body equivalent diameter
d_i	Distance between the solutions and analytical solutions
$\widehat{\boldsymbol{e}_{\mathrm{s}}}$	Unit vectors in the direction of the streamline
$\widehat{\boldsymbol{e}_{\perp}}$	Unit vectors in the direction of perpendicular to the streamline on the surface
erf^{-1}	Inverse of the error function
$\boldsymbol{F}$	Represented surface of the body
g	Acceleration of gravity
H	Enthalpy
h	Metric coefficients correspond to β
h_{s}	Metric coefficients correspond to ξ

i	Variable number
Isp_{oms}	Specific impulse of OMS
Isp_{rcs}	Specific impulse of RCS
j	Subspace number
L	Total number of variables
L_{f}	Fuselage length
M_{∞}	Free stream Mach number
m_i	Median of the ith design variable
mf	Modifying factor
N	The number of methods (solution sets)
$\boldsymbol{n}$	Normal vector
n	The number of subspace
N_{gen}	The number of generations
$N_{i,j}$	The number of solutions in $[x_{i,j-1},\ x_{i,j}]$ for the ith design variable
N_{ind}	The number of individuals
n_p	The number of Pareto solutions
N_{pa}	The numbers of primary RCS for aft
N_{pf}	The numbers of primary RCS for front
N_{total}	Total number of solutions
N_{va}	The numbers of vernier RCS for aft
N_{vf}	The numbers of vernier RCS for front
$p_{i,j}$	Proportion of solutions in the jth subspace for the ith variable

$P_{\mathrm{oms_{press}}}$	Pressure of the pressurization system for OMS
$P_{\mathrm{oms_{tnk}}}$	Pressure of the tank for OMS
$P_{\mathrm{rcs_{press}}}$	Pressure of the pressurization system for RCS
$P_{\mathrm{rcs_{tnk}}}$	Pressure of the tank for RCS
Pr	Prandtl number
q_{max}	Maximum dynamic pressure
$\dot{q}$	Heat flux
R	Nose radius
R^*	Union of all Pareto solutions
r_i	The number of Pareto solutions obtained from each optimization
r_i^*	The number of Pareto solutions present in R_1^*
R_1^i	Pareto solutions
R_1^*	New Pareto solutions of R^*
R_{oms}	Ratio of OMS engine thrust to weight
R_{p}	Ratio of primary RCS thrust to weight
R_{v}	Ratio of vernier RCS engine thrust to weight
Re_θ	Momentum thickness Reynolds number
s	Streamline length
S	Current state
S_{btot}	Fuselage wetted surface area
S_{ref}	Reference wing area
t/c	Wing thickness to chord ratio
$T_{\mathrm{req_{oms}}}$	Required thrust of OMS

$T_{\mathrm{req_p}}$	Required thrust of primary RCS
$T_{\mathrm{req_v}}$	Required thrust of vernier RCS
TRF	Technology reduction factor
ULF	Ultimate load factor
$\boldsymbol{V}_{\infty}$	Free stream velocity
$V_{\mathrm{oms_{fuel}}}$	Volumes of fuel for OMS
$V_{\mathrm{oms_{ox}}}$	Volumes of oxygen for OMS
$V_{\mathrm{oms_{press}}}$	Volume of Helium required as pressurant for OMS
$V_{\mathrm{oms_{tnk}}}$	Volume of the tank for OMS
$V_{\mathrm{rcs_{fuel}}}$	Volumes of fuel for RCS
$V_{\mathrm{rcs_{ox}}}$	Volumes of oxygen for RCS
$V_{\mathrm{rcs_{press}}}$	Volume of Helium required as pressurant for RCS
$V_{\mathrm{rcs_{tnk}}}$	Volume of the tank for RCS
V_{tot}	Fuselage volume
W_{elect}	Electrical system weight
W_{emp}	Vehicle empty weight
W_{eng}	Total weight for engine
W_{entry}	Entry weight
W_{f}	Fuselage weight
W_{fuel}	Total fuel weights
W_{gear}	Landing gear weight
W_{gtot}	Total vehicle gross weight
W_{hydr}	Hydraulics weight

W_{land}	Landing weight
W_{oms}	OMS weight
$W_{\mathrm{oms_{eng}}}$	OMS engine weight
$W_{\mathrm{oms_{fuel}}}$	Fuel weight for OMS propellant
$W_{\mathrm{oms_{install}}}$	Installation weight for OMS
$W_{\mathrm{oms_{ox}}}$	Oxygen weight for OMS propellant
$W_{\mathrm{oms_{prop}}}$	Total OMS propellant weight
$W_{\mathrm{oms_{prop_{ascent}}}}$	OMS propellant weight for ascent
$W_{\mathrm{oms_{prop_{de-orbit}}}}$	OMS propellant weight for de-orbit
$W_{\mathrm{oms_{prop_{orbit}}}}$	OMS propellant weight for orbit maneuvers
$W_{\mathrm{oms_{press}}}$	Weight of the pressurization system for OMS
$W_{\mathrm{oms_{tnk}}}$	The weight of OMS tank
W_{ox}	Total oxygen weight
W_{rcs}	RCS weight
$W_{\mathrm{rcs_{fuel}}}$	Weights of the fuel for RCS
$W_{\mathrm{rcs_{install}}}$	Installation weight for RCS
$W_{\mathrm{rcs_{ox}}}$	Weights of the oxygen for RCS
$W_{\mathrm{rcs_{pa}}}$	Weights of primary RCS for aft
$W_{\mathrm{rcs_{pf}}}$	Weights of primary RCS for front
$W_{\mathrm{rcs_{press}}}$	Weight of the pressurization system for RCS
$W_{\mathrm{rcs_{prop}}}$	Total RCS propellant weight
$W_{\mathrm{rcs_{prop_{entry}}}}$	RCS propellant weight for entry

$W_{\mathrm{rcs}_{\mathrm{prop}_{\mathrm{orbit}}}}$	RCS propellant weight on orbit
$W_{\mathrm{rcs}_{\mathrm{va}}}$	Weights of vernier RCS for aft
$W_{\mathrm{rcs}_{\mathrm{vf}}}$	Weights of vernier RCS for front
$W_{\mathrm{rcs}_{\mathrm{tnk}}}$	The weight of RCS tank
W_{pay}	Payload weight
W_{prop}	Total propellant weight
W_{pros}	Total propulsion weight
W_{tavcs}	Avionics weight
W_{str}	Total structural weight
W_{sub}	Total subsystem weight
W_{tnk}	Total weight of tank
W_{tps}	TPS weight
W_{w}	Wing weight
x_i	i^{th} design variables
$x_{i,\mathrm{extreme}}$	Extreme solutions of the ith design variables
$x_{i,\mathrm{lower}}$	Lower bound of ith variable
$x_{i,\mathrm{upper}}$	Upper bound of ith variable
$\hat{y}$	Output variables

Greek symbols

α	Angle of attack
β	Position perpendicular to the streamline
γ	Specific heat ratio
σ_i	Standard deviation i^{th} design variable

$\hat{\sigma}_i^2$	Variance related to the design variable x_i
$\hat{\sigma}_{\text{total}}^2$	Variance of output variables
$\Delta V_{\text{oms}_{\text{ascent}}}$	Total velocity change using OMS for ascent
$\Delta V_{\text{oms}_{\text{de-orbit}}}$	Total velocity change using OMS for de-orbit
$\Delta V_{\text{oms}_{\text{orbit}}}$	Total velocity change using OMS for orbit maneuvers
$\Delta V_{\text{rcs}_{\text{entry}}}$	Total velocity change using RCS for entry
$\Delta V_{\text{rcs}_{\text{orbit}}}$	Total velocity change using RCS on orbit
Δt_{h}	Time steps of the heat flux calculation
Δt_{t}	Time steps of the trajectory
ζ	Lees-Dorodnisyn transformation parameter
η_{vol}	Vehicle volumetric efficiency
η_t	Confidence level
θ	Angle between the direction of free stream velocity and the surface of the vehicle
θ_{L}	Laminar momentum thickness
$\bar{\theta}_{\text{L}}$	Mean laminar momentum thickness
λ	Taper ratio
$\lambda_{1/2}$	Mid-chord sweep angle
μ	Viscosity
μ_i	Mean value of the ith design variable
$\hat{\mu}_i$	Degree of impact of the design variable x_i on the objective function
$\hat{\mu}_{\text{total}}$	Total mean of output variables

ξ	The position along the streamline
ρ	Density
$\bar{\psi}$	Velocity gradient parameter

Subscripts

aw	Adiabatic wall
e	Boundary layer edge
L	Laminar
s	Stagnation point
w	Wall (surface)
ε	Epsilon curve

Superscripts

*	Eckert's reference enthalpy relation

Abbreviations

ANOVA	Analysis of variance
BFCS	Body-fixed coordinate system
CFD	Computational fluid dynamics
CRGA	Changing range genetic algorithm
DOF	Degree of freedom
ECEF	Earth-centered, Earth-fixed coordinate system
ECI	Earth-centered inertial coordinate
FRSI	Fibrous refractory composite insulation
GCS	Geographic coordinate system
GD	Generational distance

HASA	Hypersonic aerospace sizing analysis
HRSI	High-temperature reusable surface insulation
LES	Large eddy simulation
MDA	Multidisciplinary analysis
MDO	Multidisciplinary optimization
MOGA	Multiobjective genetic algorithm
NASA	U.S. National Aeronautics and Space Administration
NFE	The number of function evaluations
OMS	Orbital maneuvering system
PI	Proportional integral
PID	Proportional integral derivative
RANS	Reynolds-averaged Navier Stokes
RCC	Reinforced carbon–carbon
RCS	Reaction control system
RK	Runge-Kutta
SD	Standard deviation
SM	Static margin
SOM	Self-organizing map
TPS	Thermal protection system
WFG	Walking fish group problems
ZDT	Zitzler-Deb-Thiele problems

List of Figures

List of Tables

Chapter 1

Introduction

1.1 Backgrounds

These days, many report and investigator expect that the space industry will grow up continuously. Euroconsult estimates that the spacecraft market has reached 370 and 464 billion dollars in 2021 and 2022, respectively, and is expected to grow by more than 737 billion dollars by 2032, as shown in Fig. 1.1 [1,2]. In addition, According to Morgan Stanley's analysis, the revenue generated by the global space industry has the potential to exceed a trillion dollars by the year 2040, as illustrated in Fig. 1.2 [3].

To occupy these space market, private enterprises such as SpaceX, Virgin Galactic, and Blue Origin are developing launch vehicles and spacecraft. SpaceX's goal is to reduce the cost of space transportation and colonize Mars. To achieve this, they are developing both launch vehicles and spacecraft. Virgin Galactic, on the other hand, is focusing on creating commercial spacecraft for space tourists. The company has already succeeded in manned spaceflight, including with their founder. Blue Origin is working on developing rocket-powered vertical takeoff and landing vehicles to access suborbital and orbital space. These efforts suggest that space development has shifted from the government to the commercial sector, with the aim of increasing profits through the use of reusable spacecraft and diversifying flight purposes.

Specially, Boeing is developing X-37 as a reusable unmanned spacecraft, and it

was first launched in 2010. The X-37 is launched into space by a launch vehicle and then lands on Earth as a spaceplane after re-entering the atmosphere. Korea also makes an effort to develop a reusable unmanned spacecraft through grants, such as the Reusable Unmanned Space Vehicle Research Center (ReUSV) by Korea Research Institute for Defense Technology Planning and Advancement (KRIT). However, since the spacecraft development of Korea is in the early stage, a various configuration of spacecraft should be analyzed. Therefore, the development of an efficient method to conceptually design reusable unmanned spacecraft is necessary.

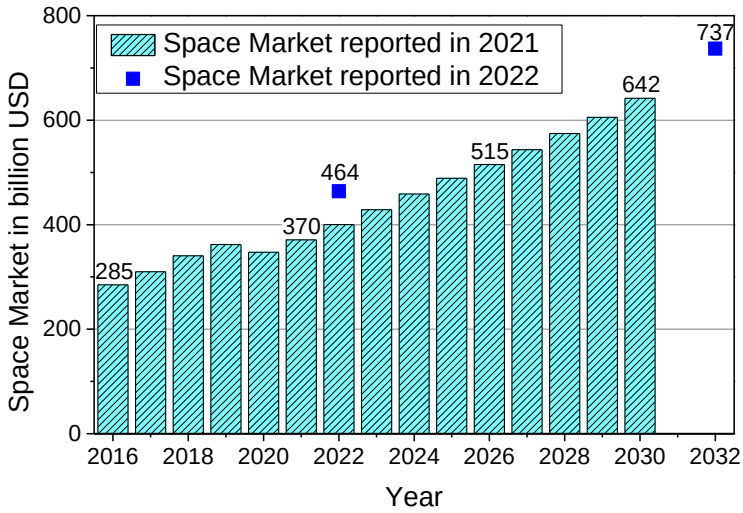

Fig. 1.1 Space market reported by Euroconsult [1,2]

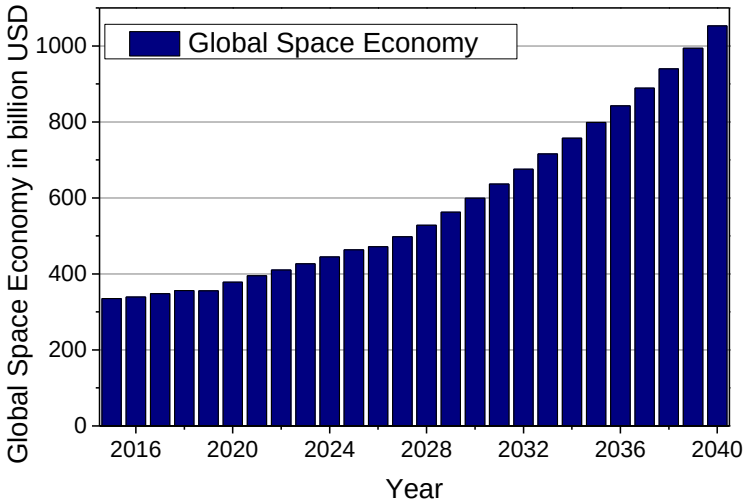

Fig. 1.2 Global space economy estimated by Morgan Stanley [3]

1.2 Previous studies for adaptive time-step method for MDO

In order to develop a high-performance reusable spacecraft, various technologies must be utilized: Geometry definition, weight analysis, propulsion analysis, aerothermodynamic analysis, trajectory analysis, and so on. To simultaneously consider these various analyses in the conceptual design, multidisciplinary optimization (MDO) should be established. Various efficient methods for each analysis in MDO was developed, such as hypersonic aerospace sizing analysis (HASA) for weight analysis [4], equations to estimate the required thrust for propulsion analysis [5], approximate convective-heating equation based on modified Newtonian theory for aerothermodynamic analysis [6], and three degree-of-freedom equation of motion.

The calculations of the aerodynamic force, heat flux, and motion are conducted by enormous times while the geometry definition, weight estimation, and propulsion analysis are performed by few times. It is because the former calculations are executed for each instance of trajectory. While the aerodynamic-force and motion calculations for an instance need a very short computational time (approximately 0.01 second), the heat-flux calculations take approximately a few second [7]. Therefore, the reduction of the number of heat-flux calculation can make more efficient MDO.

The heat flux are calculated in several million evaluations in a multidisciplinary optimization process because the heat flux should be evaluated along the entire trajectory of a vehicle, which may result in over a thousand evaluation stages and the heat-flux evaluations along the trajectory are typically simulated over a thousand times during vehicle shape optimization [8–11]. The enormous number of heat-flux

evaluations required for MDO makes this process time-consuming. Therefore, it is essential to develop an efficient method for calculating heat flux along the entire trajectory for multidisciplinary optimization.

To reduce computational costs, one practical solution is to increase the time step for trajectory analysis. As the heat flux is calculated along the entire trajectory, increasing the time step can decrease the number of calculations required and thereby relieve the computational cost. Various adaptive time-step methods have been suggested to address time-dependent problems, including the utilization of a simple equation [12–14] or a proportional-integral (PI) [15–20] or proportional-integral-derivative (PID) controller [21–23]. These methods control the time step according to the error (the rate of change for solutions). Thus, these methods are more suited for steady-state problems, in which the error decreases over time due to the convergence of solutions, and are not appropriate for trajectory analysis.

Another possible approach to reduce the computational cost in multidisciplinary analysis, including the evaluation of heat flux along a trajectory, is to split the time step into individual time steps for each analysis. This is because the required time steps for accurate computations differ among individual analyses. When the same time step is applied for all analyses, the minimum required time step is selected to ensure accurate results. However, if the time step differs for each analysis, the number of calculations decreases, leading to a reduction in computational cost. Although this method has been attempted before [24–27], the ratio of time steps between individual analyses was constant, which may not lead to a drastic reduction in computational cost since each individual time step is not controllable using the changes in the conditions for each analysis.

Therefore, a method that adjusts each individual time step for heat-flux calculation is required.

1.3 Previous studies for adaptive design space

Currently, optimization problems have become more complicated with the incorporation of multiple disciplines, such as the design of reusable unmanned spacecraft. In addition, the optimization problems take various multiobjective functions, and complexly constraints. These complexity have made it challenging to discover solutions and analyze the correlations between the quantity of interest and design variables in a straightforward manner. To address these challenges, population-based optimization methods like genetic algorithms [28] and particle swarm optimization [29] have emerged. These methods can explore a design space using multiple populations without relying on gradient information and offer several design candidates known as "Pareto solutions" [30–36]. Thus, population-based optimization is an attractive alternative for dealing with such complex problems.

Population-based methods typically seek solutions within a predefined design space that consists of the upper and lower bounds of the design variables. Because the design space is typically predetermined and remains unchanged throughout the entire optimization process, selecting an appropriate design space for the given problem is crucial. Without an appropriate design space, the optimization algorithm may fail to find desirable solutions. The selection of a suitable design space heavily relies on the prior knowledge and experience of the engineers, making it challenging to select an appropriate design space for a new type of problem that is beyond the engineer's domain of expertise. If the design space does not include the desired solutions, the optimization process will not succeed. To prevent this, engineers may choose to set a larger than necessary design space, but this may result in decreased optimization efficiency due to the stochastic processes of population-based

optimization methods, which generally operate within a fixed design space throughout the process.

To address these problems, Amirjanov [37,38] proposed a changing range genetic algorithm (CRGA). The CRGA adjusts the center of the design space to be at the mean value of the design variables of the solutions. It decreases the size of the design space by a predetermined ratio until the ratio of the current design space to the initial design space becomes below a specific value. However, sometimes the CRGA may make the design space excessively small, resulting in a failure to find the optimal solution. Amirjanov [39,40] proposed an enhancement to the previous method by introducing an algorithm that modifies the center of the design space without decreasing its size after the ratio reaches a specific value. Moreover, Amirjanov proposed a technique to determine the reduction ratio by analyzing the solution behaviors during the generation [41,42], and this approach was extended to particle swarm optimization [43]. However, for multiobjective optimization problems, this approach is not suitable as it reduces the design space size by a constant value, ignoring the distributions of the solutions of multiple objective functions. In such problems, the solutions are not unique, and the design variable distributions of the solutions converge to a range of the design space, rather than a single point. Therefore, adapting the design space for multiobjective optimization problems requires considering the distributions of the design variables of multiple objective functions.

Various researchers have endeavored to adjust design spaces by taking into account the distributions of the design variables. Adaptive search region methods have been proposed by Jeong *et al.* [44], Kitayama *et al.* [45], and Arakawa *et al.*

[46,47], which assume that the design variables have normal distributions. On the other hand, Oyama *et al.* [48–50] suggested a method that sets the cumulative distribution functions of normal distributions as genotype of genetic algorithm. The cumulative distribution functions is iteratively updated the means and standard deviations of the design variable. Initially, this method was designed for single-objective functions, but it was later improved for multi-objective function applications by utilizing a plateau region [51–53]. This method has been implemented in numerous engineering fields, such as aerodynamic design [54], conceptual design [55], turbomachinery [56], fluid-structure interaction [57], vehicle occupant restraint systems [58], and energy systems [59]. Although the widespread use of the normal distribution assumption, the design variable distributions in real-world problems are rarely normal distributions. If a design variable is not normally distributed, the variance could be exaggerated, leading to a larger design space that includes infeasible regions. This weakens the effectiveness of the design-space adaptation method because optimization efficiency is decreased with the inclusion of infeasible regions. Consequently, it is preferable to have a design-space adaptation method that takes into account the actual distributions of the solutions.

1.4 Motivation and scope of the dissertation

This study develops a novel approach to enhance the efficiency of MDO for reentry vehicles. To achieve this goal, an adaptive time-step method for each analysis in the MDO based on the current state is developed. To validate this method, the method is applied to the heat-flux calculations in the MDO for the conceptual design of reusable spacecraft. The developed approach reduces the number of heat-flux calculations required along a trajectory. A dynamic factor is introduced to adjust the time step between each heat flux calculation, resulting in a decreased time step when a large amount of heat flux is generated and an increased time step when a small amount of heat flux is generated. This method aims to increase the efficiency of MDO while obtaining detailed information on heat flux in high-heat-flux conditions.

In addition, this study develops a novel approach for adaptively adjusting the design space based on the actual distribution of solutions. This is achieved by dividing the design space into equally-sized subspaces and calculating the proportion of solutions in each subspace to the total number of solutions. The effectiveness of this method is evaluated using nineteen commonly-used multiobjective test functions to analyze its characteristics and performance.

To validate the effectiveness of the developed methods for adjusting time step for heat-flux calculation and adjusting design space, this study utilizes the developed efficient methods for heat-flux calculation and adaptive design space to perform MDO for reusable unmanned spacecraft. The optimized shapes are examined to identify the geometric features that contribute to the improved performance through data mining. The analysis of variance (ANOVA) [60], parallel chart [61], and self-organizing map (SOM) [62] methods are utilized as data mining techniques.

This dissertation is organized as follows:

Chapter 2 introduces a method to adjust the time step for an analysis in MDO based on the current state. The developed method is applied to calculate heat flux along a trajectory. For the efficient calculation, the time step for MDO are split by the time steps for heat flux and trajectory. First, the ratio of the time steps is set to constant values as previous studies to validate its effectiveness for heat-flux calculations. Then, the ratio is varied by dynamic factor that is determined using the heat flux of the stagnation point.

Chapter 3 presents the development of an adaptive design-space method that considers the actual distribution of solutions to find a suitable design space. The performance and characteristics of this method are evaluated by solving nineteen test problems. To verify the adaptive design-space method, the initial design space are shifted from the design space of the analytical solutions. Furthermore, to quantitatively validate the effectiveness of the developed method, the solutions from optimizations using the developed method and conventional method are compared by two metrics.

In Chapter 4, the MDO for reusable unmanned spacecraft are employed to validate the developed methods for heat-flux calculations and adaptive design space. The MDO is established by combining the geometry definition and the analyses of weight, propulsion, aerothermodynamics, and trajectory with the developed methods. Then, the results of the MDO using the adaptive design-space method are compared to those obtained from other design-space methods. Finally, the geometry and performance of the extreme solutions in a Pareto solution are compared to evaluate the effectiveness of the method. In addition, the geometric features that affect the

performance of the unmanned spacecraft are extracted using data mining techniques.

Lastly, Chapter 5 provides the conclusion of the dissertation.

Chapter 2

Adaptive Time-Step Method for MDO

Various analyses are implemented in the multidisciplinary optimization for the conceptual design of the reusable spacecraft. Reducing the number of calculations of analyses in MDO are necessary for the efficient optimization. To do that, adjusting the time step for each analysis in MDO is needed. Since the heat-flux calculation is time-consuming analysis in MDO for the spacecraft, diminishing the number of the heat-flux calculations has a large effect for the efficiency of the MDO.

In the MDO, a number of the heat-flux calculations are required to estimate the heat flux for entire positions of the trajectory, as illustrated in Fig. 2.1. In addition, the trajectory analysis is performed by several iterations to converge coupling variables owing to inter-relations between analyses. As a result, more than a thousand evaluations of heat flux were required to estimate the heat flux during the flight.

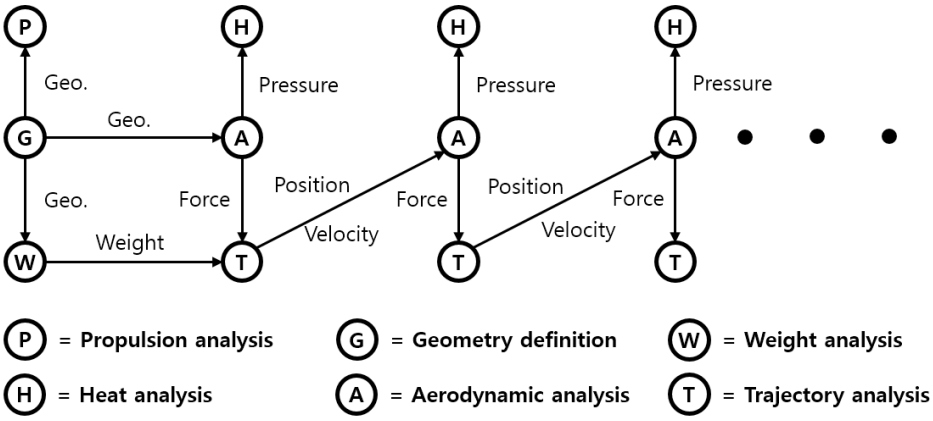

Fig. 2.1 Combined analysis for the heat flux on the KSP-1

The number of the heat-flux calculations were reduced by increasing the time step, which was achieved by multiplying it by a factor C, according to the following equation:

$$\Delta t_{\mathrm{h}} = C\Delta t_{\mathrm{t}} \tag{2.1}$$

Equation (2.1) shows that the time step of the heat flux calculation can be increased by a factor C, where Δt_{h} and Δt_{t} represent the time steps of the heat flux calculation and trajectory, respectively. If the heat flux is computed at all positions in the trajectory, then Δt_{h} is equal to Δt_{t}. By increasing the value of C, the number of heat-flux calculations can be reduced as the time step of the heat flux calculation (Δt_{h}) is increased. Conversely, decreasing the value of C leads to an increase in the number of heat-flux calculations as the time step of the heat flux calculation (Δt_{h}) is decreased.

In this study, to validate the effectiveness of the increased time step according to C, the heat-flux calculations were integrated with trajectory analysis to predict the heat flux on the spacecraft. Furthermore, weight, propulsion, and aerodynamic analyses were combined with the heat flux analysis. To apply and validate the developed efficient method for heat-flux calculation, heat fluxes on the surface of Korea Aerospace Research Institute's KSP-1, shown in Fig. 2.2, which is a three-ton class vehicle with a 7-m fuselage and 4-m span wing, were estimated from mission orbit to landing. The trajectory started at an altitude of 300 km with a speed of 7000 m/s, a flight path angle of 0°, and an incline angle of 80°.

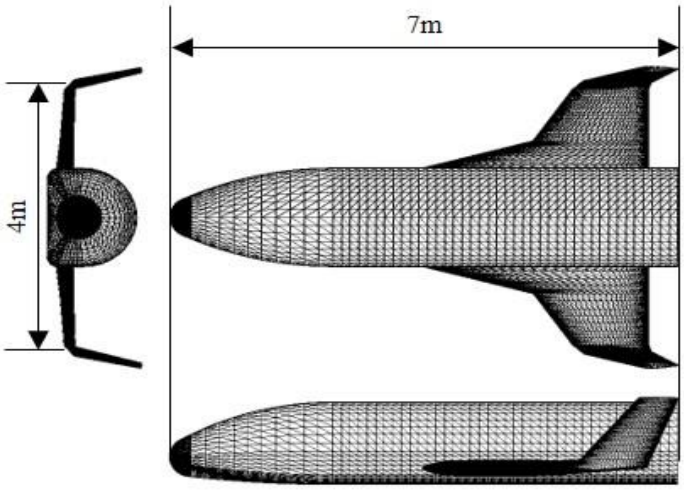

Fig. 2.2 KSP-1 geometry

2.1 Constant C

Initially, a numerical approach was used with a constant value of C. This approach is consistent with previous studies that established a fixed ratio of time steps between individual analyses [24–27]. Table 3 indicated that increasing the value of C led to a decrease in the overall computational expense due to a larger Δt_{h}, which in turn resulted in fewer computations. However, the application of the constant C led to the omission of the time corresponding to the original maximum stagnation heat flux, which in turn led to an inaccurate representation of the maximum stagnation heat fluxes, as can be seen in Table 2.1 and Fig. 2.3. Since the spacecraft's ability to endure heat is largely dependent on the maximum heat flux, this value is of critical importance.

Table 2.1 Total computational cost with constant C

C	Number of computations	Maximum stagnation heat flux [W/m^2]	Total computational cost [s]
1 (original)	1,197	2,133,778	1553.9525
2	600	2,133,778	832.1355
7	174	1,751,234	272.4919
11	111	1,700,364	211.6848
17	72	1,875,972	137.2899
23	54	634,614	114.4419
31	39	1,513,749	103.5552

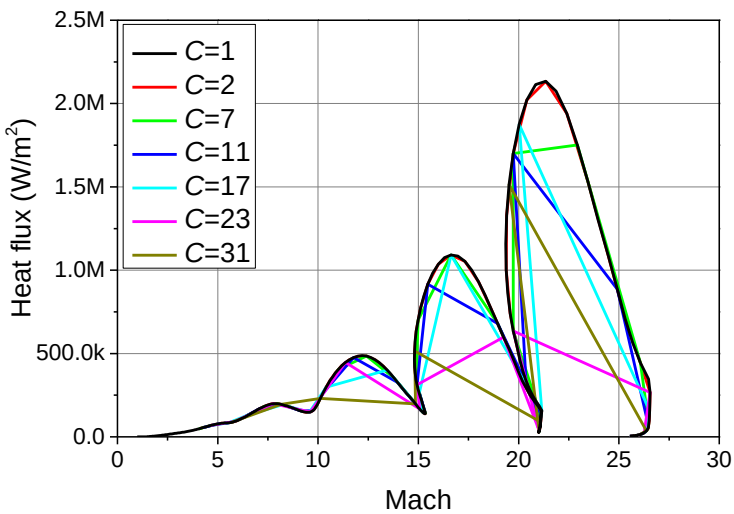

Fig. 2.3 Stagnation heat flux with constant C

2.2 Dynamic C

In the previous section, the use of a constant value of C resulted in the inability to perform heat-flux calculations at the maximum-heat-flux position in the trajectory.

To address this problem, it is necessary to use a small Δt_{h} at high heat flux for accurate calculations and a large Δt_{h} at low heat flux for efficient calculations. Therefore, a dynamic C changed by the current state was adopted, and the heat flux at the stagnation point of the vehicle $\dot{q}_{\mathrm{w,s}}$ was used as the current state. This was because estimating the heat flux at this point did not require the time-consuming streamline calculation, and a stagnation heat flux could represent the characteristics of heat fluxes in certain conditions. It should be noted that the stagnation heat flux may not be maximum due to the shape of the shock wave and the laminar-turbulent flow transition. To define the dynamic factor C, the heat flux at the stagnation point, $\dot{q}_{\mathrm{w,s}}$, was used, and it was expressed as follows:

$$C = \mathrm{round}[S^b \times a] + 1 \tag{2.2}$$

$$S = \frac{\dot{q}_{\mathrm{w,s,\_max}} - \dot{q}_{\mathrm{w,s}}}{\dot{q}_{\mathrm{w,s,max}}} \tag{2.3}$$

Herein, S represents the current state. Equation (2.2) introduced a and b as parameters that control the heat flux calculation time step along the trajectory. The dynamic factor C in Eq. (2.2) was determined based on the difference between the heat flux at a specific moment ($\dot{q}_{\mathrm{w,s}}$) and the maximum heat flux at the stagnation point throughout the trajectory ($\dot{q}_{\mathrm{w,s,max}}$). The maximum heat flux is an essential parameter throughout the trajectory of hypersonic vehicles due to the potential for destruction and damage by high heat flux. Equation (2.2) and (2.3) demonstrates that the heat-flux calculation time step decreased when the heat flux at the stagnation point was high and increased when it was low. This phenomenon indicates that the efficiency of the heat-flux calculation during multidisciplinary analysis improves with an elongated time step under low heat flux conditions. Conversely, detailed

information about heat flux is obtained by shortening the time step under high-heat-flux conditions since periods with high heat flux are critical due to the possibility of vehicle destruction and damage. The maximum time step increases with a larger value of a because the maximum value of C increases. If b increases, the time step decreases at low stagnation heat flux since the value of C is low, as depicted in Fig. 2.4.

In the other words, the term of S as Eq. (2.3) represent the current state in contrast with the maximum value. Therefore, this adaptive time-step method adjusts the time step based on the current state.

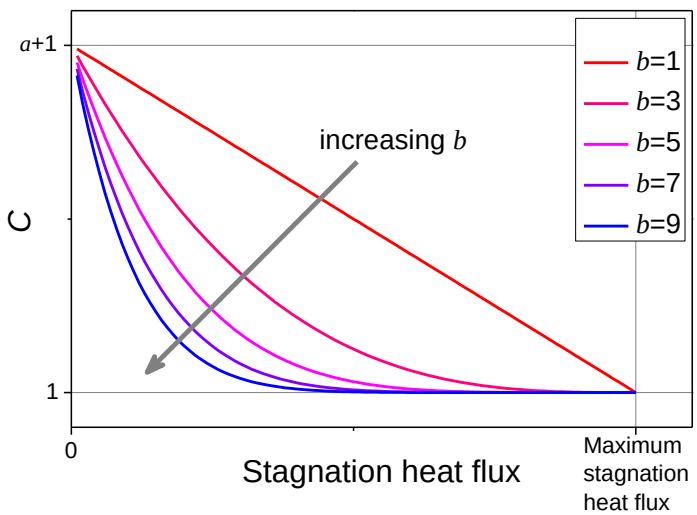

Fig. 2.4 Behavior of the dynamic C with b

To determine the optimal values of a and b in Eq. (2.2), a series of calculations were performed by varying a from 10 to 100 at intervals of 10, and b from 1 to 10 at intervals of 1. Table 2.2 and Fig. 2.5 display the results for some of the iterations for the sake of brevity. The application of Eq. (2.2) reduced the total computational cost by approximately one-tenth, as illustrated in Table 2.2. Moreover, the maximum

heat fluxes remained unchanged compared to the original values, as presented in Table 2.2 and Fig. 2.5, since the time step at high stagnation heat flux was shortened. By keeping b constant and increasing a, the number of computations reduced because the maximum value of C became large. Conversely, by keeping a constant and increasing b, the number of computations increased since a relatively low value of C was maintained at a low stagnation heat flux, as indicated in Fig. 2.4.

Table 2.2 Total computational cost with dynamic C

a	b	Number of calculations	Maximum stagnation heat flux [W/m^2]	Total computational cost [s]
Original		1,197	2,133,778	1553.9525
20	1	75	2,133,778	125.2944
10	2	156	2,133,778	215.9298
20	2	93	2,133,778	139.2946
30	2	72	2,133,778	103.8202
40	2	57	2,133,778	81.8680
20	3	108	2,133,778	132.3144
30	3	81	2,133,778	98.2031
20	4	123	2,133,778	128.7518
30	4	96	2,133,778	85.8918

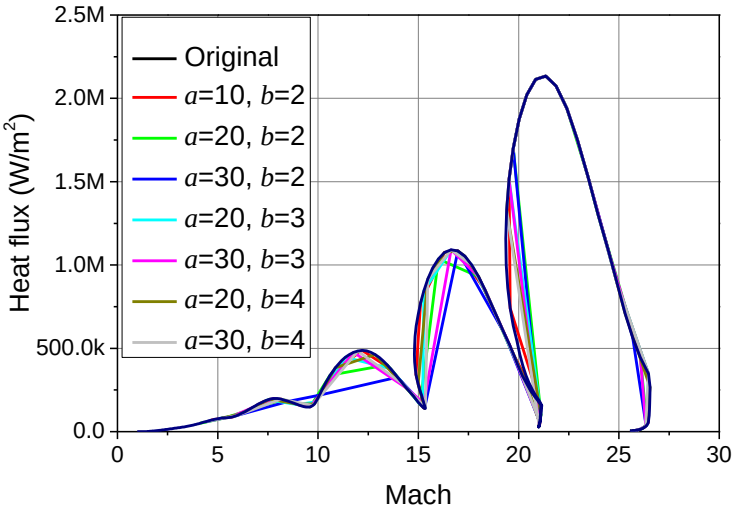

Fig. 2.5 Stagnation heat flux evaluated with changes in the dynamic C

In order to evaluate the performance of Eq. (2.2) with respect to a and b, we have defined two metrics: efficiency and accuracy.

(Efficiency) (2.4)

$$= \frac{\text{(the number of calculation with original)} - \text{(the number of calculation using Eq.((2.2))}}{\text{(the number of calculation with original)}}$$

(accuracy) (2.5)

$$= 1 - \frac{\int_{\text{trajectory}} \left|\text{(heat flux of original)} - \text{(heat flux using Eq.((2.2))}\right| \, d(Mach)}{\int_{\text{trajectory}} \text{(heat flux of original)} \, d(Mach)}$$

When the value of a decreases, the efficiency decreases as C becomes small. Conversely, the efficiency increases when a increases since C becomes large. A decrease in b leads to a decrease in accuracy due to the constant C, while an increase in b results in an increase in accuracy as C approaches one. Figure 2.6 illustrates the relationship between efficiency, accuracy. The shaded region in Fig. 2.6 indicates the area with both efficiencies and accuracies greater than 0.9. Table

2.3 describes three examples located in the region denoted by bold squares in Fig. 2.6. A high efficiency is observed when a and b are 40 and 2, respectively, with relatively low accuracy. Conversely, when a is 20 and b is 3, accuracy is high despite the relatively low efficiency. The remaining sample compromises both efficiency and accuracy. In this study, a and b are set to 20 and 1 for the compromised performance.

Table 2.3 Total computational cost for high efficiency and accuracy

a	b	Number of calculations	Efficiency	Maximum stagnation heat flux [W/m^2]	Accuracy
40	2	57	0.95238	2,133,778	0.91737
20	1	75	0.93042	2,133,778	0.93484
20	3	108	0.90727	2,133,778	0.95610

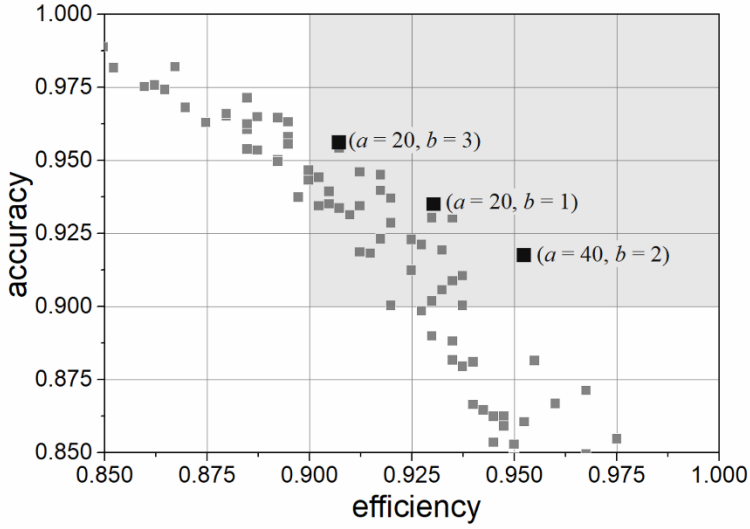

Fig. 2.6 Efficiencies and accuracies about a and b

Chapter 3

Adaptive Design-Space Method

3.1 Method implement

This study develops a design-space adaptation method that involves modifying the design space by comparing the probability densities of an arbitrary control distribution and the actual solution distribution. The control distribution is the arbitrary distribution that is expected as the distribution of the design variables, while the actual distribution is determined based on the ratio of the solutions, which satisfy all constraints, in the subspaces of the design space. This study utilized the standard normal distribution as the control distribution and divided it into n subspaces with a confidence level of η_t, as illustrated in Fig. 3.1(a). The probability densities of the jth subspace for the control distribution were indicated by A_j in Fig. 3.1 (a). To obtain the actual solution distribution, the current design space was partitioned into n subspaces with equal sizes, as depicted in Fig. 3.1 (b). The boundaries of each subspace were represented by $x_{i,j}$, where $x_{i,n}$ and $x_{i,0}$ were the previous upper and lower bounds of the ith variable, respectively. The proportion of solutions in the jth subspace for the ith variable ($p_{i,j}$) was determined by computing the ratio of the number of solutions belonging to the jth subspace to the total number of solutions, as shown in Fig. 3.1 (b).

$$p_{i,j} = \frac{N_{i,j}}{N_{\text{total}}} \tag{3.1}$$

Herein, N_{total} refers to the total number of solutions, and $N_{i,j}$ refers to the number

of solutions in which the ith design variable value ranged between $[x_{i,j-1},\ x_{i,j}]$. The adjustments to the lower and upper bounds of the design variables were determined by comparing A_1, A_2, and $p_{i,1}$ for the lower bound, and A_{n-1}, A_n, and $p_{i,n}$ for the upper bound. For example, if $p_{i,1}$ was smaller than A_1, the lower bound was contracted. Conversely, if $p_{i,1}$ was greater than $(A_1 + A_2)$, the lower bound was expanded. Table 3.1 summarizes the specific criteria for shrinking, retaining, and expanding.

Table 3.1 Conditions for shrinking, retaining, and expanding the design-variable bound

	lower bound	upper bound
Shrinking	$p_{i,1} < A_1$	$p_{i,n} < A_n$
Retaining	$A_1 < p_{i,1} < (A_1 + A_2)$	$A_n < p_{i,n} < (A_{n-1} + A_n)$
Expanding	$p_{i,1} > (A_1 + A_2)$	$p_{i,n} > (A_{n-1} + A_n)$

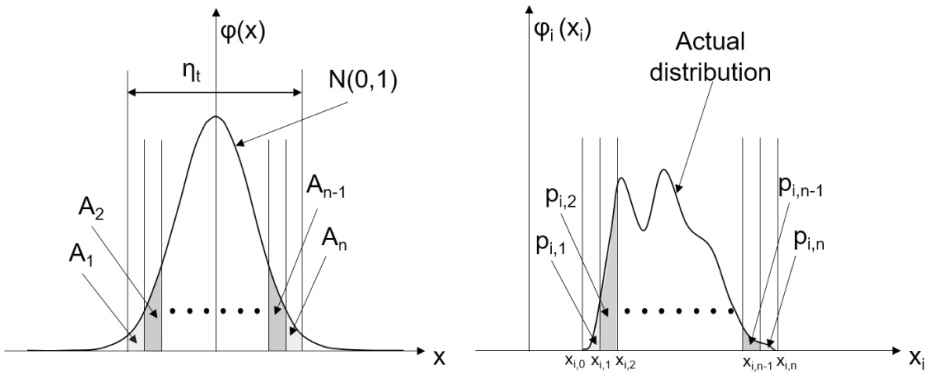

(a) control distribution (b) actual distribution

Fig. 3.1 Proportions of subspace

Once the criteria for shrinking, retaining, and expanding the boundary were established, the design space of the ith variable was modified according to the following equations:

1. Shrinking

$$x_{i,\text{lower}} = \min(x_{i,\{j|p_j > A_1\}}) \tag{3.2}$$

$$x_{i,\text{upper}} = \max(x_{i,\{j|p_j > A_n\}}) \tag{3.3}$$

2. Retaining

$$x_{i,\text{lower}} = x_{i,0} \tag{3.4}$$

$$x_{i,\text{upper}} = x_{i,n} \tag{3.5}$$

3. Expanding

$$x_{i,\text{lower}} = m_i - \left(x_{i,0} - m_i\right)\frac{\text{erf}^{-1}(\eta_t)}{\text{erf}^{-1}\left[2\left(\sum_{j=1}^{n-1} p_{i,j}\right)-1\right]} \tag{3.6}$$

$$x_{i,\text{upper}} = m_i + \left(x_{i,n} - m_i\right)\frac{\text{erf}^{-1}(\eta_t)}{\text{erf}^{-1}\left[2\left(\sum_{j=2}^{n} p_{i,j}\right)-1\right]} \tag{3.7}$$

Here, $x_{i,\text{lower}}$ and $x_{i,\text{upper}}$ denote the lower and upper bounds of the ith design variable, respectively. The median of the ith design variable is represented by m_i, and erf^{-1} is the inverse of the error function.

The upper bound of the largest-j^{th} subspace satisfying $p_{i,j} > A_n$ $(j = 1, \dots, n)$ becomes the new upper bound of the design space when shrinking the upper bound (Eq. (3.3)). When retaining the bound, the upper bound remains the same. To expand the upper bound, since the standard normal distribution is used as the control distribution, the new upper bound is determined using Eq. (3.7). Similar procedures are applied when adapting the lower bound. This method shrinks the bounds of the design space with few solutions and expands the bounds of the design space with many solutions. Therefore, the infeasible space including no feasible samples and the space including few feasible samples are excluded to increase the searchability of the optimization, and the space having the probability of the existence for

solutions is added to find feasible solutions.

In order to enhance the efficiency of the method developed in this study, an initial investigation of the feasible design space is carried out through optimization without adaptation before applying the adaptation process as previously described. The lower and upper bounds of the feasible design space are then determined by employing Eqs. (3.8) and (3.9), respectively.

$$x_{i,\text{lower}} = \min_j x_{i,j} - \left[\max_j x_{i,j} - \min_j x_{i,j}\right] \times 0.05 \tag{3.8}$$

$$x_{i,\text{upper}} = \max_j x_{i,j} + \left[\max_j x_{i,j} - \min_j x_{i,j}\right] \times 0.05 \tag{3.9}$$

In multiobjective optimization, the solutions that are the best for each objective function observed so far are called extreme solutions and are very important. Therefore, the design space where extreme solutions exist should be maintained. However, these space typically has a low probability density of solutions, making them likely to be removed by the developed adaptation method. To prevent the loss of these areas, an extra adjustment of the design space is performed using Eqs. (3.10) and (3.11)

If $x_{i,\text{lower}} > \min(x_{i,\text{extreme}})$,

$$x_{i,\text{lower}} = \min(x_{i,\text{extreme}}) - [x_{i,n} - x_{i,0}] \times 0.05 \tag{3.10}$$

If $x_{i,\text{upper}} < \max(x_{i,\text{extreme}})$,

$$x_{i,\text{upper}} = \max(x_{i,\text{extreme}}) + [x_{i,n} - x_{i,0}] \times 0.05 \tag{3.11}$$

In this context, $x_{i,\text{extreme}}$ refers to the values of the ith design variables found in extreme solutions.

3.2 Application to test problems

3.2.1 ZDT problems

The characteristics and performance of the developed method were examined by implementing it on the Zitzler-Deb-Thiele (ZDT) problems [63]. These problems are commonly used as multiobjective test functions to assess the performance of optimization methods. The ZDT problems consist of six test functions that encompass a range of function types such as convex, concave, discrete, and multi-modal functions. Therefore, these problems were suitable for validating the performance of the developed method and assessing its ability to handle different types of functions. The specific problem settings were as follows:

ZDT problems

Minimize	f_1 and f_2	
Constraint	$0 \leq x_1 \leq 1$	
	$0 \leq x_i \leq 1$	for $i = 2, \ldots, L$ (except ZDT4)
	$-5 \leq x_i \leq 5$	for $i = 2, \ldots, L$ (ZDT4)
Initial space	$-0.1 \leq x_1 \leq 0.9$	
	$0 \leq x_i \leq 1$	for $i = 2, \ldots, L$ (except ZDT4)
	$-5 \leq x_i \leq 5$	for $i = 2, \ldots, L$ (ZDT4)
Side constraint	$0 \leq x_i$	for $i = 2, \ldots, L$ (except ZDT4)
Analytical solutions	$0 \leq x_1 \leq 1$	
	$x_i = 0$	for $i = 2, \ldots, L$

(3.12)

The total number of variables for the Zitzler-Deb-Thiele (ZDT) problems is denoted by Ls, which is set to 30, 30, 30, 10, and 10 for ZDT1–ZDT4 and ZDT6, respectively, by referring to Ref. [63]. The ZDT5 problem was not considered for testing in this study as it is not a real-numbered problem.

The multiobjective genetic algorithm based on the developed method was executed with a population size of 256 individuals in each of the 600 generations. Adaptation of the design space was performed every 100 generations, using the feasible solutions obtained from the last 20 generations. The parameters for adaptation were set as follows: the confidence level was set to 99% (denoted as η_t) and the number of divisions was set to 20 (denoted as n). The process of randomly reinitializing while preserving the extreme solutions was carried out after the design-space adaptation was completed. This ensured that the diversity of the populations was maintained, while the best solution for each objective function was preserved. Figure 3.2 illustrates the procedure.

Moreover, to compare the developed method, two other optimizations were conducted, one with adaptation assuming normal distributions [44] and another with a fixed design space. In the method that assumed normal distributions, the adaptation of the design space was performed using Eqs. (3.13) and (3.14).

$$x_{i,\mathrm{lower}} = \mu_i - \sigma_i \sqrt{2}\,\mathrm{erf}^{-1}(\eta_t) \tag{3.13}$$

$$x_{i,\mathrm{upper}} = \mu_i + \sigma_i \sqrt{2}\,\mathrm{erf}^{-1}(\eta_t) \tag{3.14}$$

The variables μ_i, σ_i, and η_t refer to the mean value, standard deviation, and confidence level of the ith design variable, respectively.

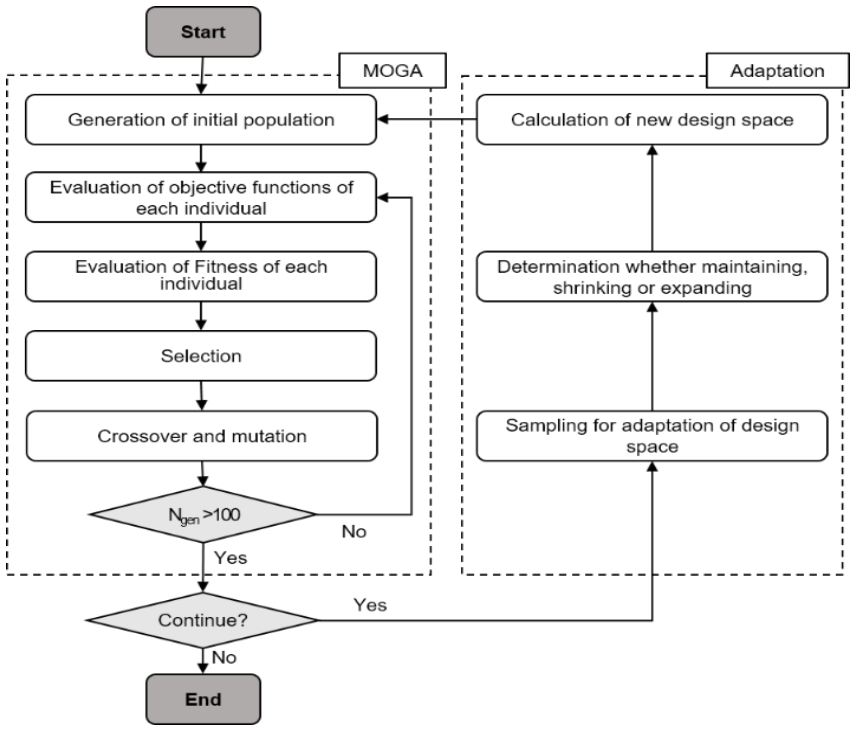

Fig. 3.2 Procedure of the genetic algorithm and the design-space adaptation

The results of the optimization process for the developed method, the method based on normal distribution, and the fixed design space are presented in Fig. 3.3. The results of all three methods are comparable to the analytical solutions. However, the optimization results for the fixed design space were unable to find solutions within the range of $x_1 > 0.9$, as demonstrated in the subplots of Fig. 3.3. This is because the fixed design space does not encompass $0.9 < x_1 < 1.0$. In contrast, the adaptive-design-space method adjusted the design space to encompass the entire solution space. The final adjusted design spaces for the developed method and the method that assumed normal distributions were notably distinct, as presented in Table 3.2 and Fig. 3.4. The design space obtained from the developed method was much closer to the range of analytical solutions than the one obtained from the method that assumed normal distributions.

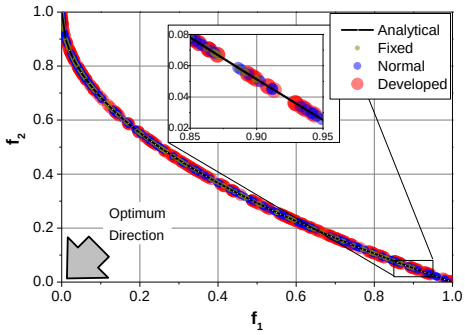

(a) ZDT1

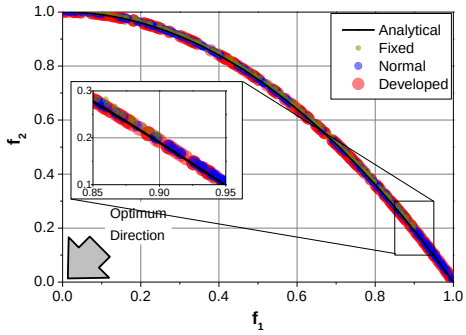

(b) ZDT2

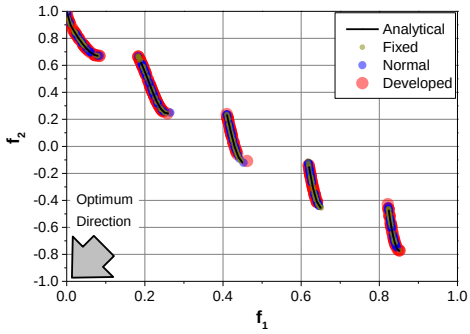

(c) ZDT3

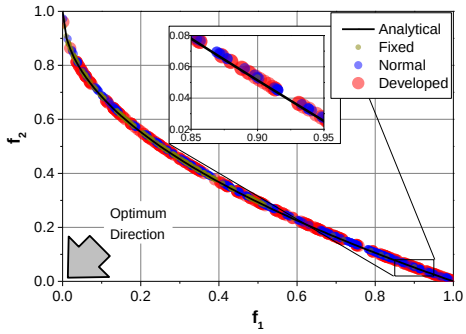

(d) ZDT4

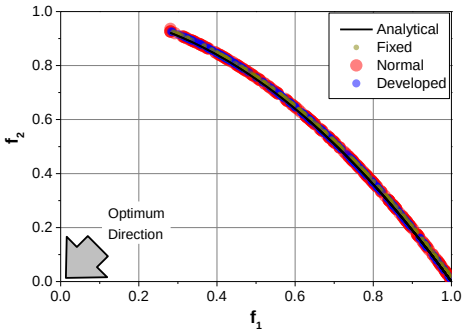

(e) ZDT6

Fig. 3.3 Pareto solutions for ZDT problems

Table 3.2 Adapted design spaces for ZDT problems

	With the method assuming normal distributions			With the developed method		
	$x_{1,\mathrm{lower}}$	$x_{1,\mathrm{upper}}$	Design space for x_1	$x_{1,\mathrm{lower}}$	$x_{1,\mathrm{upper}}$	Design space for x_1
ZDT1	-0.3635	1.1987	1.5621	-0.0007	1.0036	1.0044
ZDT2	-0.1603	1.2882	1.4485	-0.0498	1.0098	1.0596
ZDT3	-0.2864	1.1355	1.4219	-0.0450	0.9446	0.9896
ZDT4	-0.2700	1.2449	1.5149	-0.0243	1.1801	1.2044
ZDT6	0.0071	0.0881	0.0810	0.0045	0.0870	0.0825

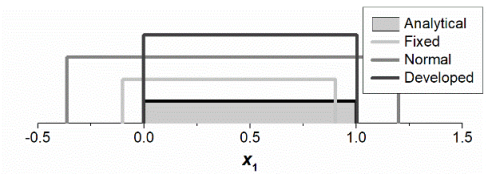

(a) ZDT1

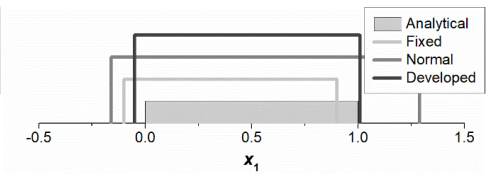

(b) ZDT2

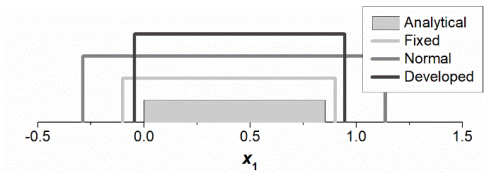

(c) ZDT3

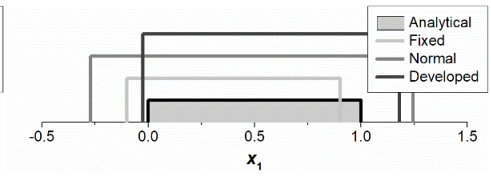

(d) ZDT4

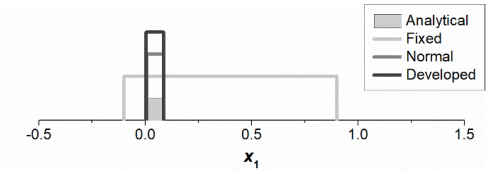

(e) ZDT6

Fig. 3.4 Final design spaces for x_1 in the ZDT problems

In addition, to measure the effectiveness of the developed method quantitatively, the generational distance (GD) was utilized. The GD calculates the average distance between the analytical solutions and the Pareto solutions, and is expressed as follows [64]:

$$\mathrm{GD} = \frac{\sqrt{\sum d_i^2}}{n_p} \tag{3.15}$$

The GD is defined as the average distance between the Pareto solutions and the analytical solutions, where d_i represents the distance between the Pareto solutions and analytical solutions, and n_p is the number of Pareto solutions. The results

showed that the GD of the developed method was much better than the other methods, as shown in Fig. 3.5. This indicates that the efficiency of the MOGA using the developed method was higher than that of the method assuming normal distributions. This was because the developed method properly adjusted the design space to a space where the solution existence probability was high, while excluding the infeasible design space.

The performance of the developed method was further evaluated using the purity metric [65]. This metric can compare the performance of multiple optimization methods. The process of calculating the purity metric is as follows: Firstly, calculate $r_i = |R_1^i|$, where $i = 1,2,\cdots,N$. Herein, N is the number of methods (solution sets), and r_i is the number of Pareto solutions obtained from each optimization. Then, obtain the new Pareto solutions R_1^* by taking the union of all Pareto solutions, as $R^* = \cup_{i=1}^{N}\{R_1^i\}$. Finally, r_i^* denotes the number of Pareto solutions present in R_1^*, which is expressed as:

$$r_i^* = |\{\gamma | \gamma \in R_1^i \text{ and } \gamma \in R_1^*\}| \tag{3.16}$$

The definition of the purity metric for the ith method is as follows:

$$P_i = \frac{r_i^*}{r^i},\ i = 1,2,\cdots,N \tag{3.17}$$

The purity metric has a range of values from 0 to 1, and it represents the ratio of the number of non-dominated Pareto solutions to other Pareto solutions. Therefore, a higher value of the purity metric indicates better quality Pareto solutions.

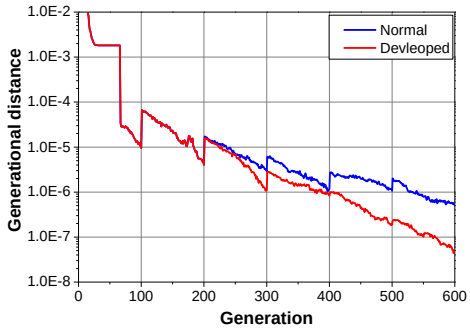

(a) ZDT1

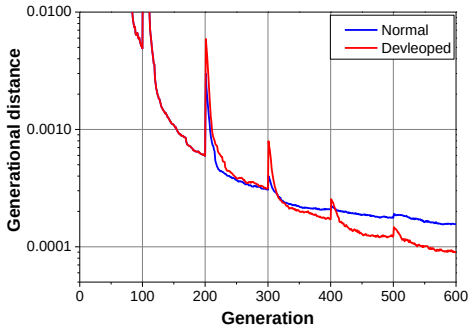

(b) ZDT2

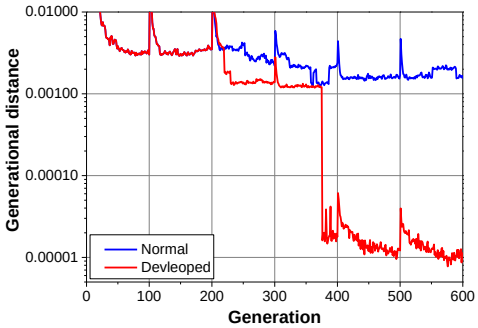

(c) ZDT3

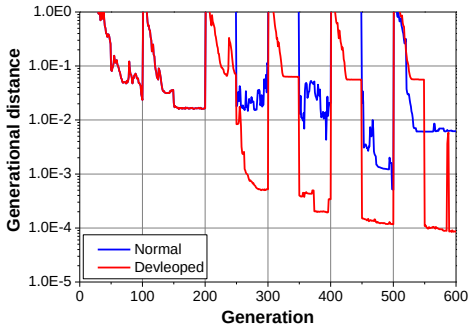

(d) ZDT4

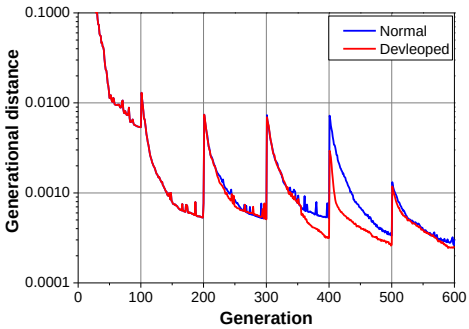

(e) ZDT6

Fig. 3.5 GD evolution trends for the ZDT problems

The purity metric values for the developed method were the same as to those of the method assuming normal distributions up to 200 generations, as shown in Fig. 3.6. This was because the solutions generated by both methods were identical during this period. However, the purity metric values for the developed method was higher than those of the other methods after 200 generations. This indicated that the Pareto solutions produced by MOGA using the developed method were better than those obtained using the normal distribution assumption.

In order to investigate why the method assuming normal distributions resulted in a wider adapted design space, the proportion of points evenly distributed on the analytical Pareto front of ZDT1 was calculated. Figure 3.7 presents the proportions of evenly-divided subspaces. The results showed that the distribution was biased towards $x_1 = 0$ rather than a normal distribution. In this particular case, the mean value and standard deviation of x_1 were 0.4100 and 0.3093, respectively. Consequently, the upper and lower bounds of x_1 obtained using the method assuming normal distributions were -0.3867 and 1.2067, respectively. As a result, this method expanded the design space into the infeasible region. The MOGA using the method assuming normal distributions had limited efficiency improvement because it expanded the design space to include the infeasible region. On the other hand, the developed method adapted the design space based on the actual distribution and did not expand to the infeasible region. Consequently, the developed method was able to adapt the design space appropriately to the space where solutions exist, resulting in higher efficiency of the MOGA using this method compared to the method assuming normal distributions.

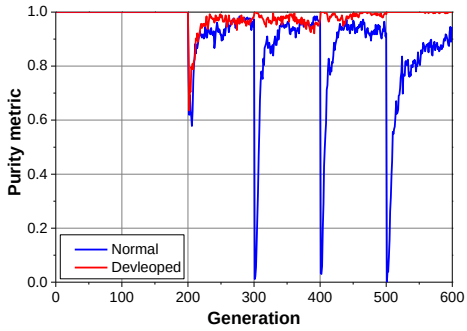

(a) ZDT1

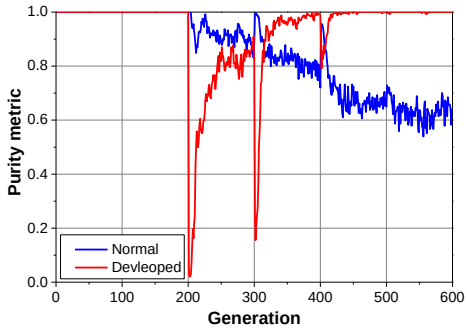

(b) ZDT2

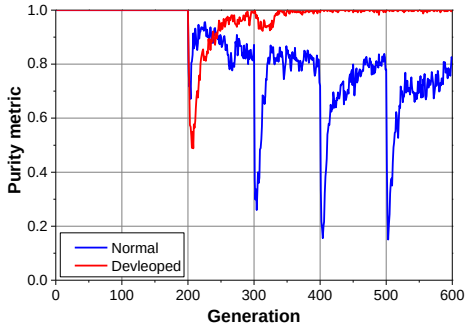

(c) ZDT3

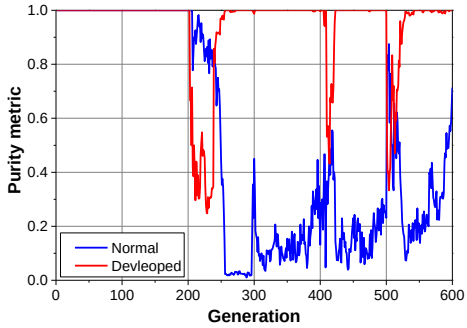

(d) ZDT4

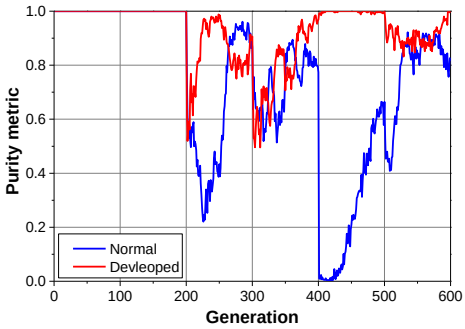

(e) ZDT6

Fig. 3.6 Purity metric evolution trends for the ZDT problems

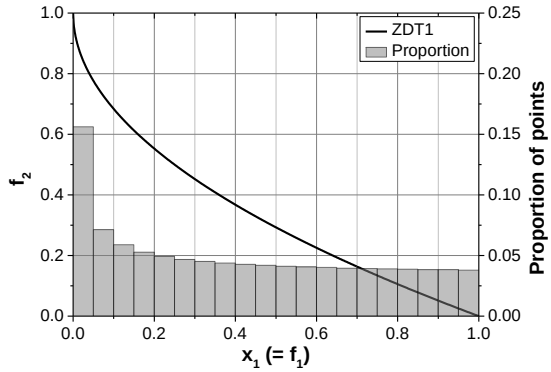

Fig. 3.7 Distribution of solutions in the subspaces

3.2.2 I problems

To evaluate the efficiency of the developed method in three-objective optimization, I problems were utilized [66]. These problems are made up of five functions, denoted as I1 through I5. The I1 problem is a basic and separable function, while the remaining functions become more complex by introducing dependencies between variables. The problems were established in the following manner:

I problems

Minimize	f_1, f_2, and f_3	
Constraint	$0 \leq x_i \leq 1$	for $i = 1, \ldots, L$
Initial space	$-0.1 \leq x_1 \leq 0.9$	
	$-0.1 \leq x_2 \leq 0.9$	
	$0 \leq x_i \leq 1$	for $i = 3, \ldots, L$
Side constraint	$0 \leq x_i$	for $i = 3, \ldots, L$
Analytical solutions	$\sum_{i=1}^{3} f_i = 1$	
	$x_i = 0.35$	for $i = 3, \ldots, L$

(3.18)

In the I problems, the total number of variables is denoted by L, where the variables include both position- and distance-related variables. Typically, the position-related variables determine the positions of objective functions, while the distance-related variables define the distance between the objective functions and the analytical solutions. In this study, two position-related variables and six distance-related variables were used, based on the references [66,67], resulting in a total of eight variables.

To solve the I problems, the real-coded MOGA was employed, using the same settings as those used for the ZDT problems, except for the number of objective functions. For comparison purposes, an optimization with adaptation assuming normal distributions [44] was also carried out. To quantitatively evaluate the performance of the developed method, its GD and purity metric values were compared to those obtained using the method assuming normal distributions.

The adaptive-design-space method was employed to modify the design space. The final adapted design space covered the whole design space of the analytical solutions, as indicated in Tables 3.3 and 3.4 and illustrated in Fig. 3.8. The adapted design space of the developed method was found to be closer to the design space of the analytical solutions than that of the method assuming normal distributions. In addition, Figs. 3.9 and 3.10 demonstrate that the GD and purity metric of the developed method were superior to those of the method assuming normal distributions. These results are consistent with those obtained for two-objective functions. Therefore, the effectiveness of the developed method in three-objective optimization was also confirmed.

Table 3.3 Adapted design spaces of x_1 for I problems

	With the method assuming normal distributions			With the developed method		
	$x_{1,\mathrm{lower}}$	$x_{1,\mathrm{upper}}$	Design space for x_1	$x_{1,\mathrm{lower}}$	$x_{1,\mathrm{upper}}$	Design space for x_1
I1	-0.2182	1.2254	1.4436	-0.0496	1.0500	1.0996
I2	-0.3675	1.2206	1.5881	-0.0339	1.0488	1.0827
I3	-0.0246	1.2464	1.2710	-0.0204	1.0396	1.0600
I4	-0.0919	1.3081	1.4000	-0.0475	1.0499	1.0975
I5	-0.0706	1.3001	1.3707	-0.0158	1.0069	1.0227

Table 3.4 Adapted design spaces of x_2 for I problems

	With the method assuming normal distributions			With the developed method		
	$x_{2,\mathrm{lower}}$	$x_{2,\mathrm{upper}}$	Design space for x_2	$x_{2,\mathrm{lower}}$	$x_{2,\mathrm{upper}}$	Design space for x_2
I1	-0.0455	1.4436	1.4891	-0.0364	1.2844	1.3207
I2	0.0444	1.2413	1.2856	-0.0420	1.0466	1.0886
I3	-0.2675	1.1978	1.4652	-0.0016	1.0444	1.0460
I4	-0.0492	1.3765	1.4257	-0.0496	1.0211	1.0707
I5	-0.3070	1.2718	1.5788	-0.0343	1.0145	1.0487

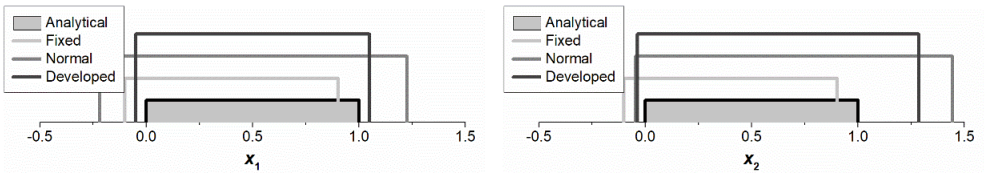

(a) I1

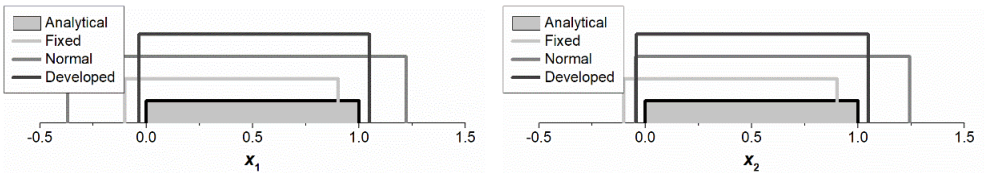

(b) I2

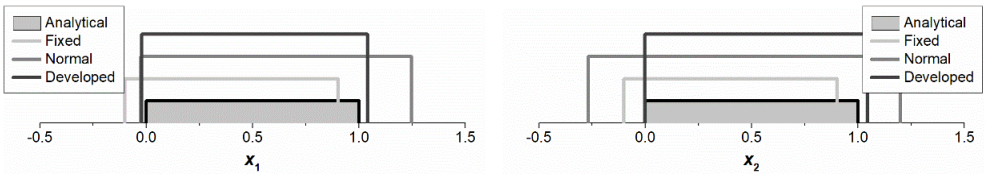

(c) I3

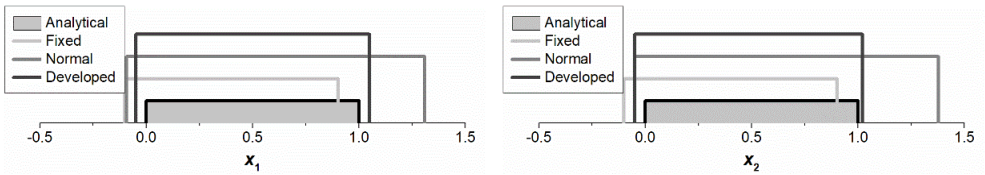

(d) I4

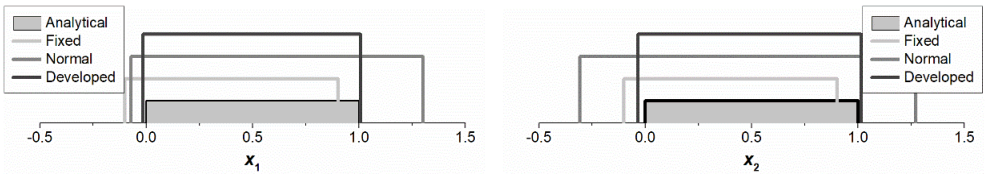

(e) I5

Fig. 3.8 Final design spaces for x_1 and x_2 in the I problems

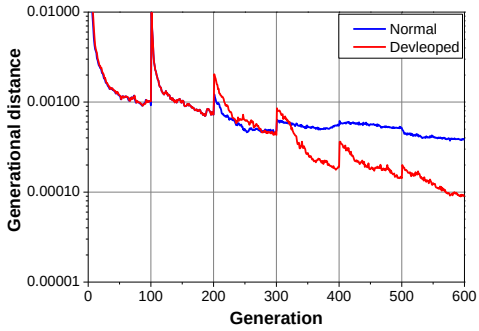

(a) I1

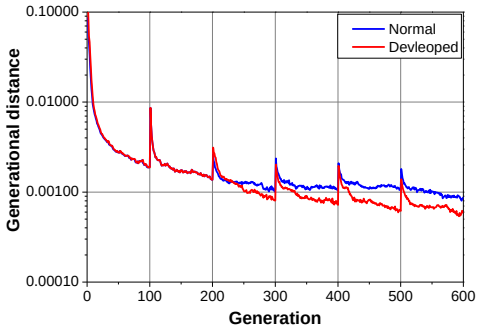

(b) I2

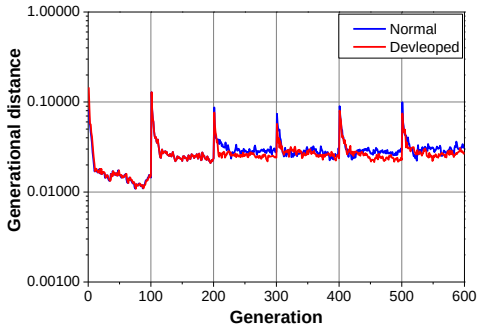

(c) I3

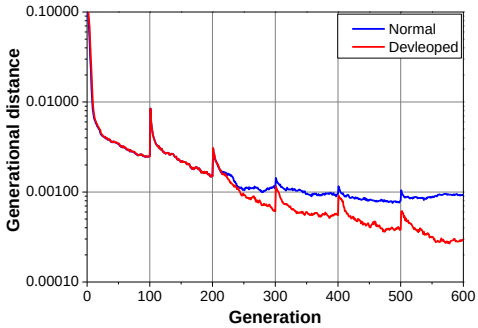

(d) I4

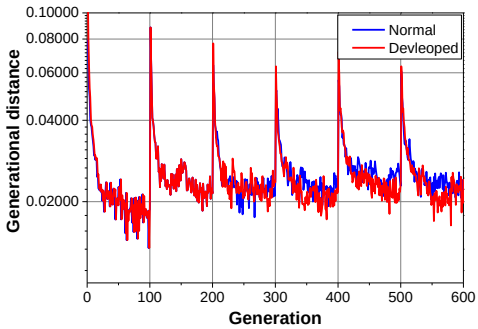

(e) I5

Fig. 3.9 GD evolution trends for the I problems

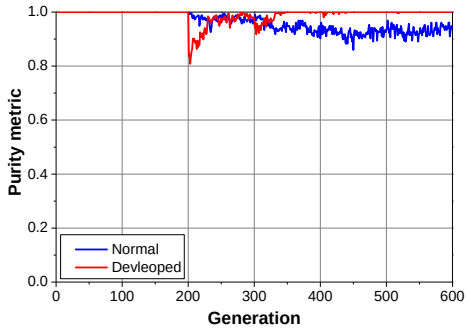

(a) I1

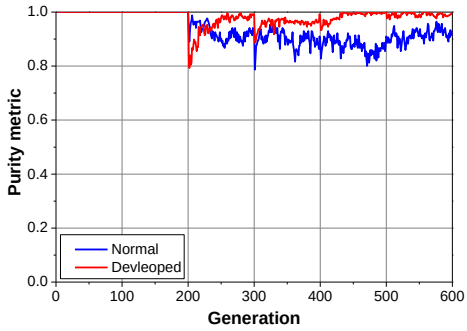

(b) I2

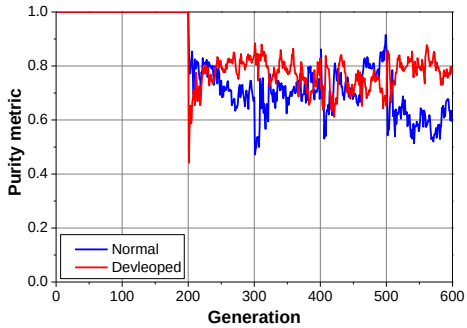

(c) I3

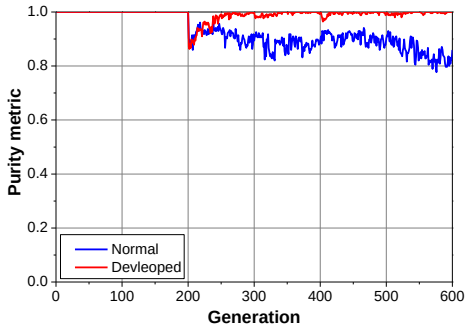

(d) I4

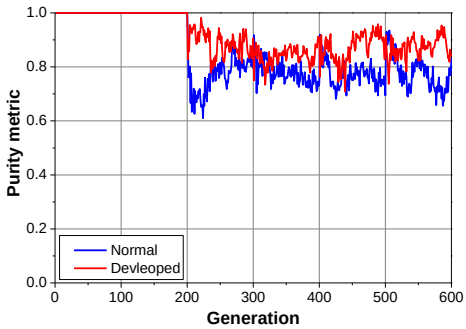

(e) I5

Fig. 3.10 Purity metric evolution trends for the I problems

3.2.3 WFG problems

To evaluate the effectiveness of the developed method in more complicated three-objective optimization, the WFG problems [68] were employed, which are commonly used for evaluating the performance of multi-objective optimization algorithms. The WFG problems consist of nine functions, namely WFG1–9.

The Pareto optimal front of WFG1 exhibits both convex and concave characteristics and contains flat and polynomial mapping functions. WFG2 has a convex and disconnected Pareto optimal front and a non-separable function. The Pareto optimal front of WFG3 is a linear function with a non-separable function. On the other hand, WFG4–9 have concave Pareto optimal fronts, and WFG4–6 are multi-modal, deceptive, and non-separable, respectively. The functions of WFG7 and WFG8 depend on parameters, and WFG9 features a non-separable, multi-modal, deceptive, and parameter-dependent function. The WFG problems are considered appropriate for validation purposes as they demonstrate various characteristics that are commonly observed in real-world multi-objective optimization problems. The problems are specified as follows:

WFG problems

Minimize	f_1, f_2, and f_3		
Constraint	$0 \leq x_i \leq 1$	for $i = 1, \dots, L$	
Initial space	$-0.1 \leq x_1 \leq 0.9$		
	$-0.1 \leq x_2 \leq 0.9$		
	$0 \leq x_i \leq 1$	for $i = 3, \dots, L$	
Side constraint	$0 \leq x_i$	for $i = 3, \dots, L$	
Analytical solutions	$x_i = 0.35$	for $i = 3, \dots, L$	(3.19)

In this study, L refers to the total number of variables used in the WFG problems. The variables in these problems also consist of position- and distance-related variables. Consistent with Ref. [66,67], this study adopted two position-related variables and six distance-related variables, resulting in a total of eight variables, denoted as L.

To solve the WFG problems, the real-coded MOGA was utilized with the same settings as the I problems. An optimization method that assumes normal distributions [44] was also employed to compare results. To quantitatively verify the performance of the developed method, the GD and purity metric were compared between the two methods.

The adapted design space was adjusted using the adaptive-design-space method, covering the whole design space of analytical solutions, as presented in Tables 3.5 and 3.6 and Fig. 3.11. The final adapted design space of the developed method was closer to the design space of the analytical solutions than the method that assumed normal distributions. In addition, Figs. 3.12 and 3.13 show that the GD and the purity metric of the developed method was better than that of the method that assumed normal distributions. These findings correspond with the results obtained for the two-objective functions and I problems. As a result, the performance of the developed method was validated for three-objective functions as well.

Table 3.5 Adapted design spaces of x_1 for WFG problems

	With the method assuming normal distributions			With the developed method		
	$x_{1,\text{lower}}$	$x_{1,\text{upper}}$	Design space for x_1	$x_{1,\text{lower}}$	$x_{1,\text{upper}}$	Design space for x_1
WFG1	-0.3589	0.6892	1.0481	-0.0425	0.5522	0.5947
WFG2	-0.0758	1.1430	1.2188	-0.0472	1.0499	1.0970
WFG3	-0.1266	1.1492	1.2757	-0.0469	1.0499	1.0968
WFG4	-0.1360	0.3901	0.5261	-0.0043	0.3472	0.3515
WFG5	-0.3740	1.2769	1.6509	-0.2399	1.1277	1.3676
WFG6	-0.2108	1.0843	1.2951	-0.0500	1.0499	1.0998
WFG7	-0.2707	1.2946	1.5654	-0.0524	1.0444	1.0969
WFG8	-0.0554	1.2464	1.3018	-0.0204	1.0396	1.0600
WFG9	-0.1599	1.1295	1.2893	-0.0447	1.0205	1.0653

Table 3.6 Adapted design spaces of x_2 for WFG problems

	With the method assuming normal distributions			With the developed method		
	$x_{2,\mathrm{lower}}$	$x_{2,\mathrm{upper}}$	Design space for x_2	$x_{2,\mathrm{lower}}$	$x_{2,\mathrm{upper}}$	Design space for x_2
WFG1	-0.1210	0.2249	0.3460	-0.0218	0.1984	0.2202
WFG2	-0.0844	1.2683	1.3527	-0.0025	1.2084	1.2108
WFG3	-0.2542	1.1574	1.4116	-0.1946	1.0638	1.2584
WFG4	-0.1695	0.4647	0.6342	0.0952	0.3934	0.4886
WFG5	-0.4397	1.4283	1.8680	-0.2895	1.0133	1.3028
WFG6	-0.0482	1.4019	1.4501	-0.0108	1.2598	1.2706
WFG7	-0.0496	1.3588	1.4085	-0.0304	1.1911	1.2215
WFG8	-0.2675	1.1978	1.4652	-0.0016	1.0444	1.0460
WFG9	-0.2365	1.1513	1.3878	-0.1578	1.0292	1.1870

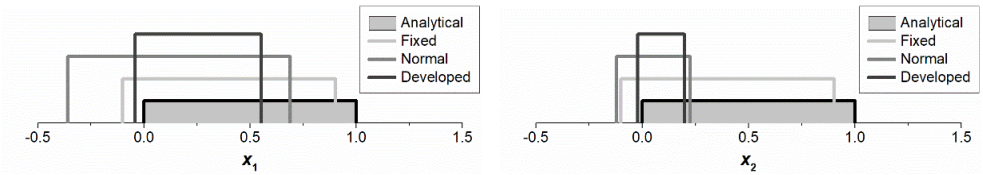

(a) WFG1

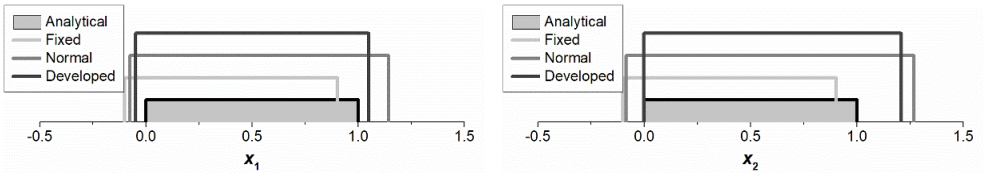

(b) WFG2

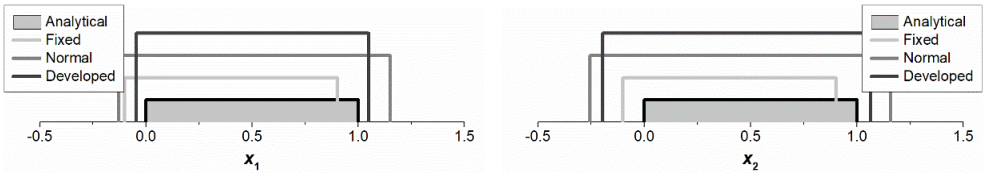

(c) WFG3

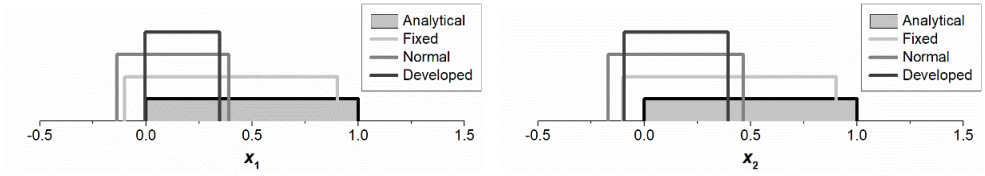

(d) WFG4

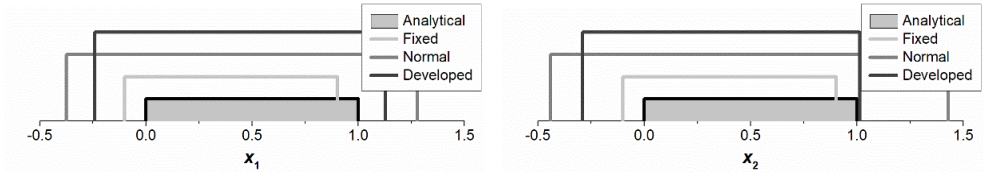

(e) WFG5

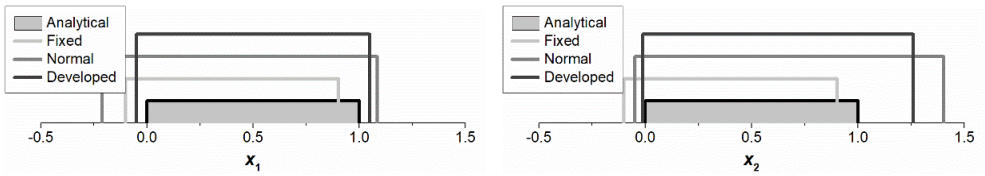

(f) WFG6

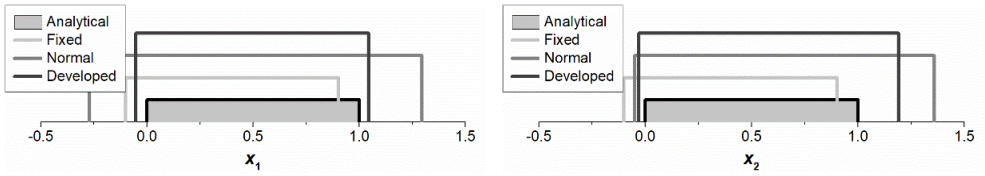

(g) WFG7

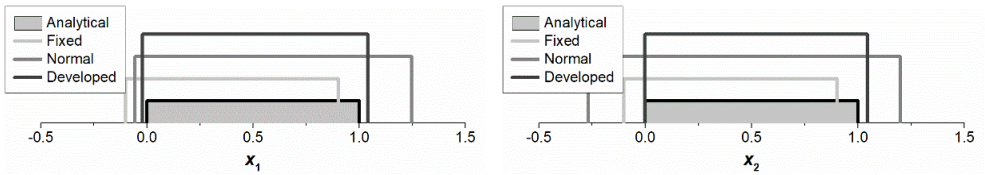

(h) WFG8

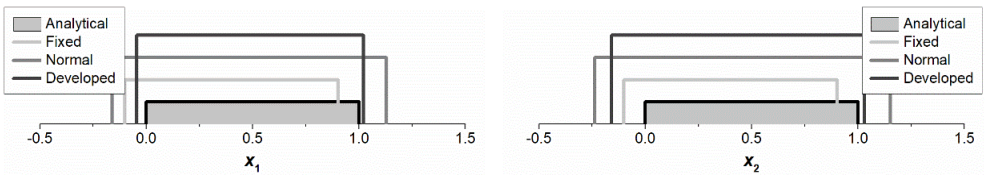

(i) WFG9

Fig. 3.11 Final design spaces for x_1 and x_2 in the WFG problems

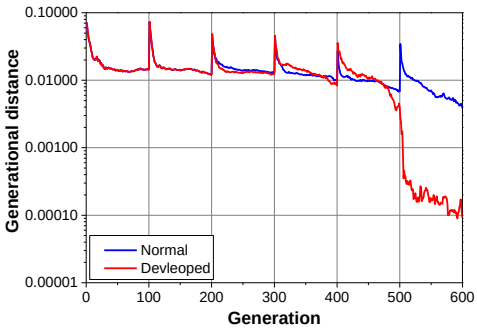

(a) WFG1

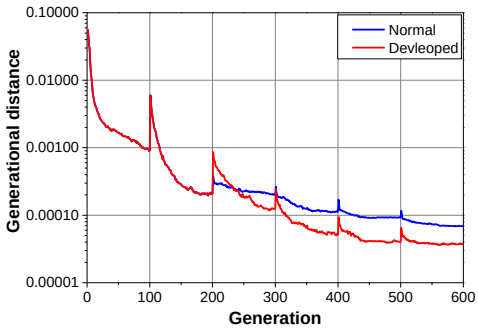

(b) WFG2

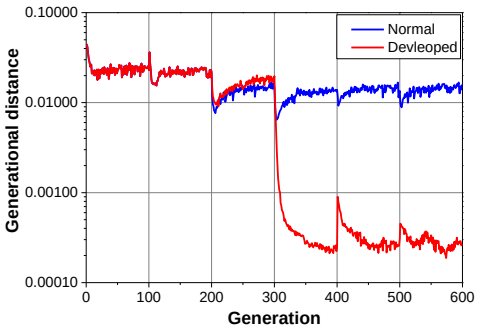

(c) WFG3

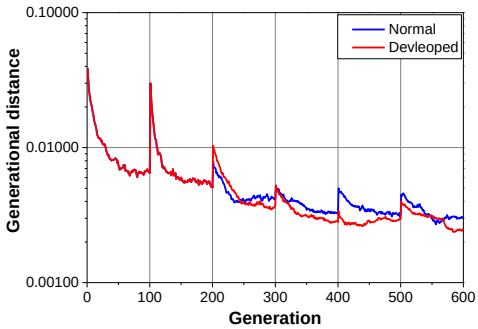

(d) WFG4

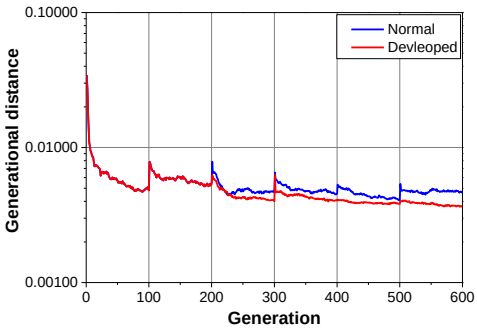

(e) WFG5

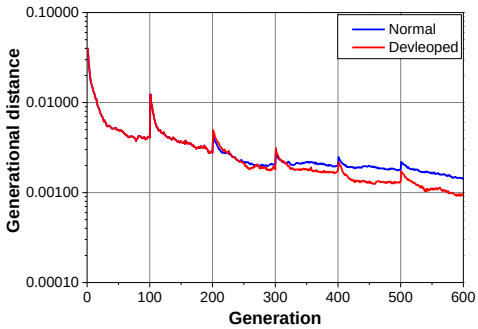

(f) WFG6

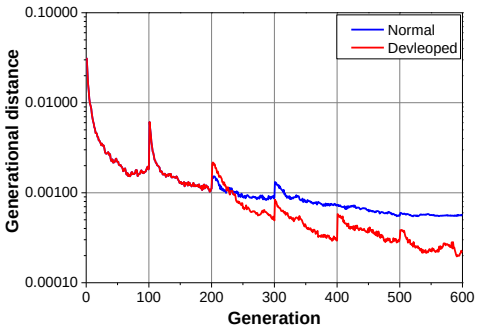

(g) WFG7

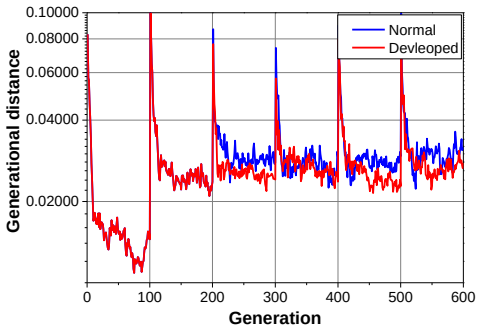

(h) WFG8

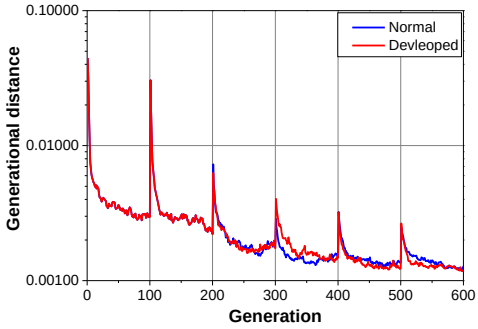

(i) WFG9

Fig. 3.12 GD evolution trends for the WFG problems

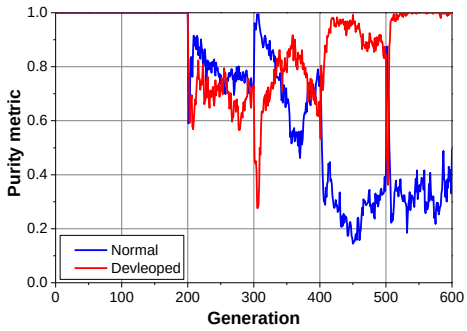

(a) WFG1

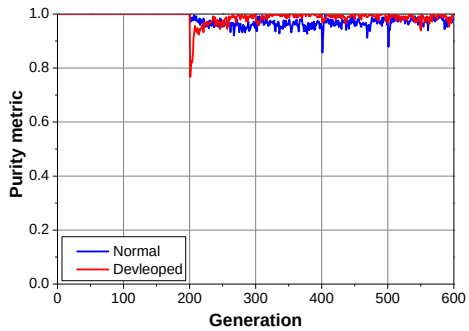

(b) WFG2

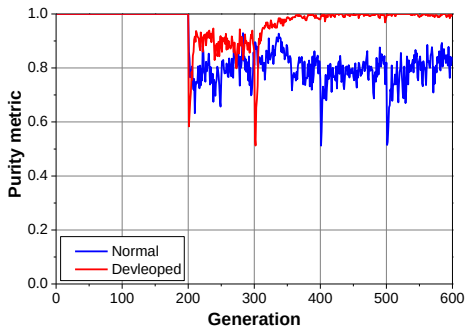

(c) WFG3

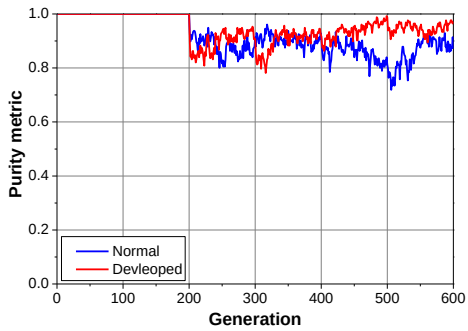

(d) WFG4

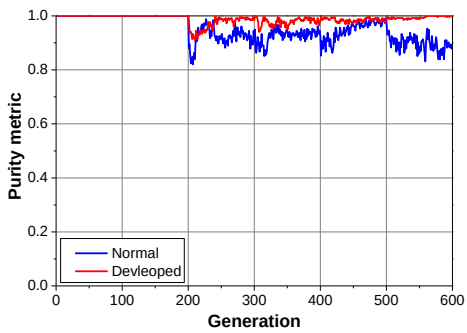

(e) WFG5

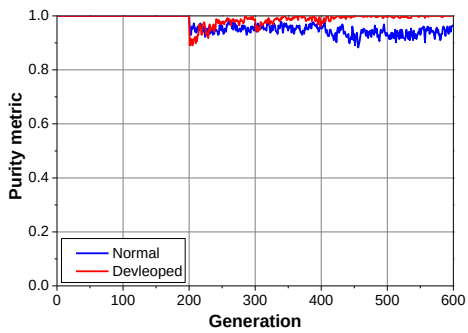

(f) WFG6

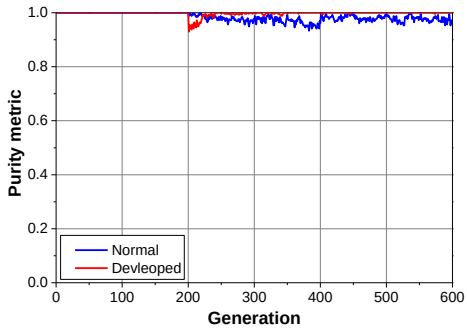

(g) WFG7

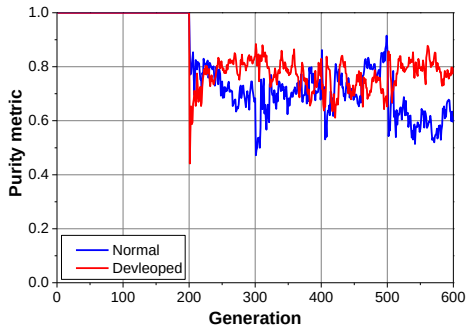

(h) WFG8

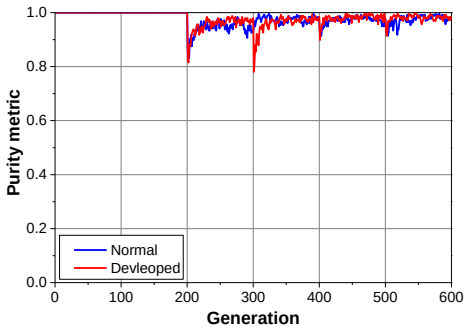

(i) WFG9

Fig. 3.13 Purity metric evolution trends for the WFG problems

Chapter 4

Application to Reusable Unmanned Spacecraft

4.1 Establishment of MDO

To validate the effectiveness of the developed method of adaptive time step and adaptive design space, the developed methods were utilized to the design of unmanned spacecraft involving a multidisciplinary optimization problem, which includes defining the geometry, conducting various analyses (such as weight, propulsion, aerothermodynamics, and trajectory analysis), and optimizing the design using MOGA [8], as shown in Fig. 4.1. As depicted in Fig. 4.2, each discipline in spacecraft design is closely interrelated since the output of one discipline serves as input for another. Therefore, it requires iterations of calculations until converged coupling variables is achieved. Once the coupled variables had converged, the performance of the spacecraft was evaluated based on its geometry, and optimization was subsequently carried out accordingly.

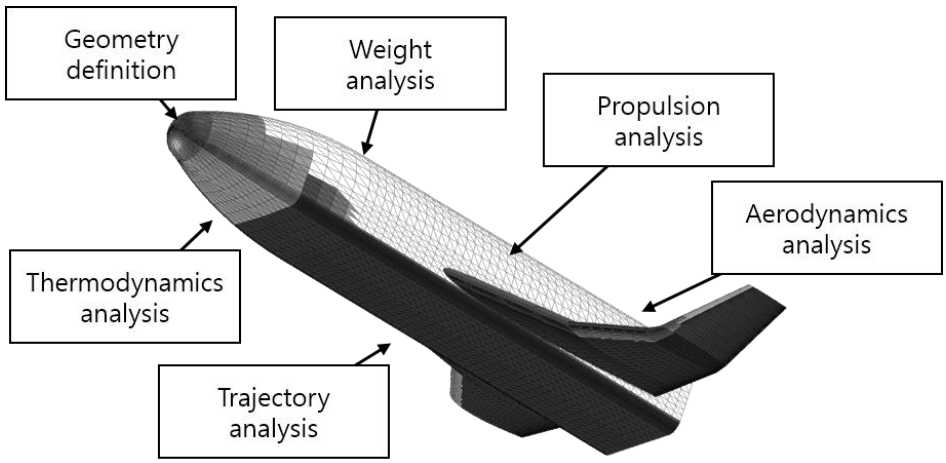

Fig. 4.1 Analyses in MDO

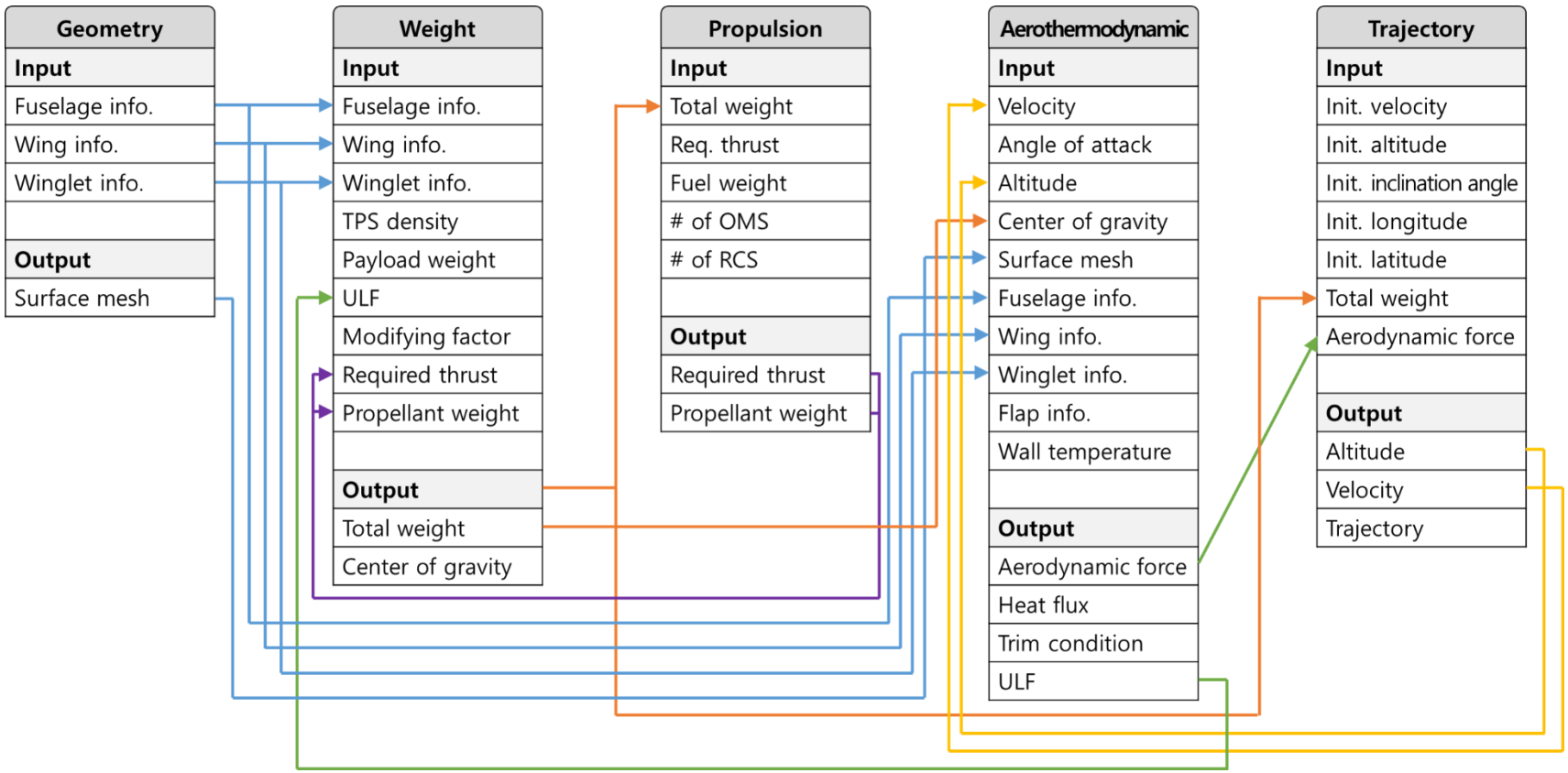

Fig. 4.2 The data flow chart of Multidisciplinary Analysis

4.1.1 Geometry definition

A total of 22 design variables were utilized to determine the geometry of various parts of the spacecraft including the fuselage, wing planform, winglet, and airfoil as illustrated in Fig. 4.3. The nose section of the fuselage was created with a spherically blunted tangent ogive curve, while a rectangular height, corner radius, and width were utilized to define one section. The planform of the wing and winglet were described using ten variables, including the inboard and outboard sweep angle, winglet sweep angle, dihedral angle, winglet dihedral angle, wing span, winglet span, kink position, root chord, and winglet tip chord. In this study, the airfoil was defined as a NACA 4-digit series using the wing-leading-edge radius instead of thickness to directly regulate the heat flux on the wing leading edge. Two variables were used to establish the relative position between the wing and fuselage. The design variables summarized in Table 4.1. Lastly, a rear body flap was present with the same width as the fuselage and 1/8 length of the total length.

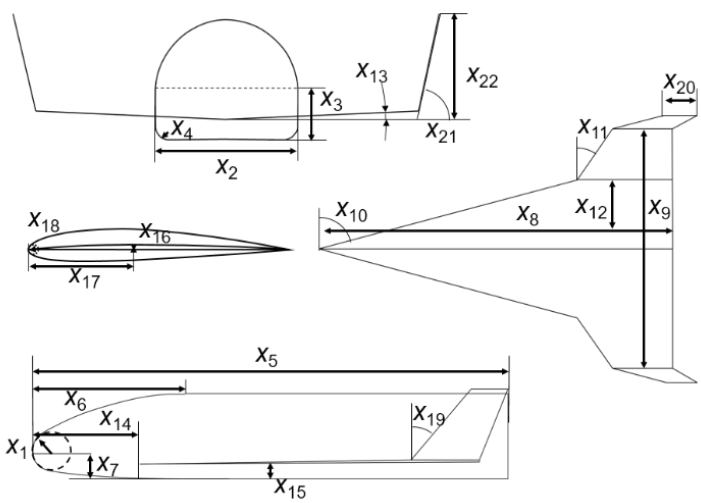

Fig. 4.3 Spacecraft design variables

Table 4.1 Spacecraft design variables

Part	Design variables	Description
Fuselage	x_1	Nose radius [m]
	x_2	Fuselage width [m]
	x_3	Rectangular height of fuselage section [m]
	x_4	Corner radius of fuselage section (radius / (width / 2)) [ ]
	x_5	Total length [m]
	x_6	Nose length (nose length / total length) [ ]
	x_7	Nose height [m]
Wing	x_8	Root chord length [m]
	x_9	Span [m]
	x_{10}	1st sweep angle [°]
	x_{11}	2nd sweep angle [°]
	x_{12}	Kink position (kink position / span) [ ]
	x_{13}	Dihedral angle [°]
	x_{14}	Wing longitudinal position (position / total length) [ ]
	x_{15}	Wing vertical position (position / total height) [ ]
Airfoil	x_{16}	Camber [ ]
	x_{17}	Camber position [ ]
	x_{18}	Leading edge radius [m]
Winglet	x_{19}	Sweep angle [°]
	x_{20}	Tip chord length [m]
	x_{21}	Dihedral angle [°]
	x_{22}	Span [m]

4.1.2 Weight analysis

The weight analysis involves calculating the weight of each component of the spacecraft and determining the center of gravity of the entire vehicle. The dimensions of each part are specified in the vehicle geometry definition, and the propulsion analysis provides the propellant weight and required thrust. This study utilized hypersonic aerospace sizing analysis (HASA) to estimate the weight of each component using statistical techniques [4]. The data flow chart of HASA is illustrated in Fig. 4.4. However, the HASA method was modified to enhance its precision as the statistical equations of the original HASA were developed based on data from 100 ton class vehicles, whereas the focus of this study is on vehicles weighing approximately 2-3 ton [5,69].

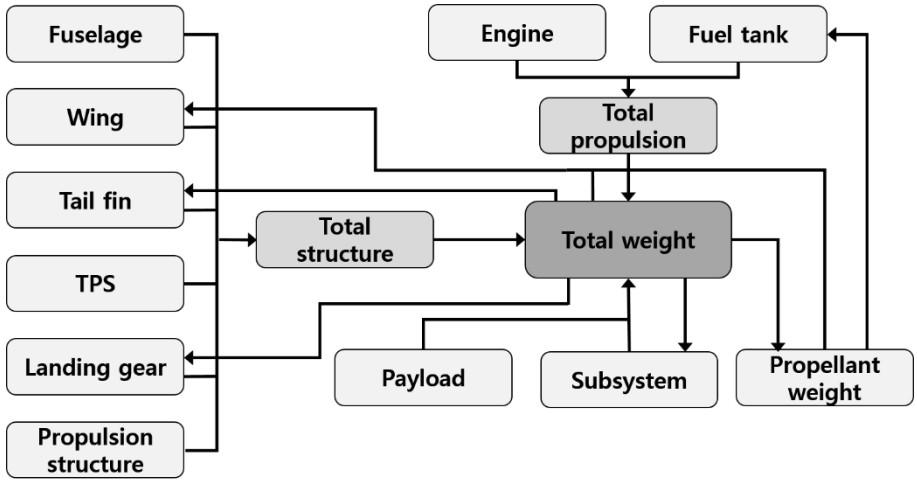

Fig. 4.4 The data flow chart of HASA

Fuselage weight

The weight of the body comprises important structural parts except the propellant tanks and thrust structure. The modifying factor can also consider advancements in

material technology. Figure 4.5 illustrates the modifying factor (mf) with respect to the structural temperature of different materials like aluminum, titanium, and Rene 41. In this study, the modifying factor is 1.148 because the structure temperature was maintained as 300 °C with titanium.

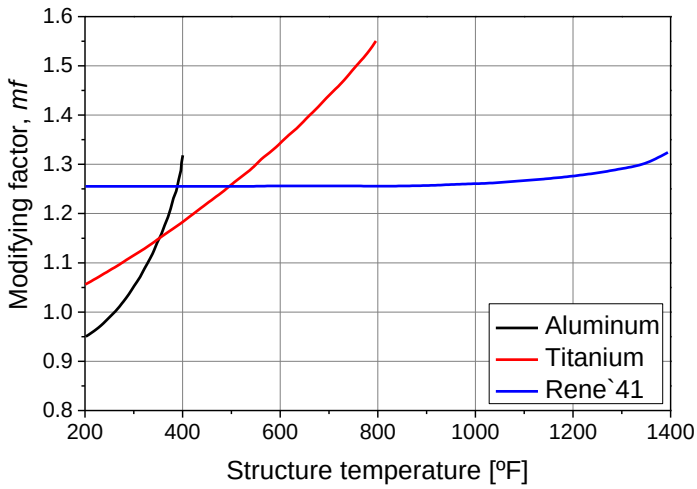

Fig. 4.5 Modifying factor according to structure temperature

The equation for the fuselage weight is as follows:

$$W_{\mathrm{f}} = 0.341(mf)(\sigma)^{1.0} \tag{4.1}$$

$$\sigma = \left|\left(\frac{L_{\mathrm{f}}ULF}{D_{\mathrm{be}}}\right)^{0.15}(q_{\max})^{0.16}(S_{\mathrm{btot}})^{1.05}\right| \tag{4.2}$$

where W_{f}, L_{f}, ULF, $q_{\max}$, and S_{btot} are the fuselage weight, fuselage length, ultimate load factor, maximum dynamic pressure, and fuselage wetted surface area, respectively. The body equivalent diameter (D_{be}) is:

$$D_{\mathrm{be}} = \sqrt{\frac{V_{\mathrm{tot}}}{L_{\mathrm{f}}\frac{\pi}{4}\eta_{\mathrm{vol}}}} \tag{4.3}$$

The vehicle volumetric efficiency (η_{vol}) is typically 0.7.

Wing weight

The equation for wing weight considers the wing box structure, the aerodynamic control surfaces, and the wing carry-through structure. It is dependent on the empty weight of the vehicle and the wing aspect ratio and taper ratio.

The empty weight of the vehicle is defined as:

$$W_{\mathrm{emp}} = W_{\mathrm{gtot}} - W_{\mathrm{prop}} \tag{4.4}$$

Herein, W_{gtot}, W_{emp}, and W_{prop} are the total vehicle gross weight, vehicle empty weight, and total propellant weight. The equation for wing weight is as follows:

$$W_{\mathrm{w}} = 0.2958(mf)\left\{\left|\frac{W_{\mathrm{emp}}ULF}{1000}\right|^{0.52} |S_{\mathrm{ref}}|^{0.7} |AR|^{0.47} \left|\frac{1+\lambda}{t/c}\right|^{0.4} \left|0.3 + \frac{0.7}{\cos(\lambda_{1/2})}\right|\right\}^{1.017} \tag{4.5}$$

where S_{ref}, AR, λ, t/c, and $\lambda_{1/2}$ are reference wing area, aspect ratio, taper ratio, wing thickness to chord ratio, and mid-chord sweep angle.

Thermal protection system weight

To calculate the weight of the thermal protection system (TPS), the density of the TPS and its area were multiplied. The TPS material for each surface was selected based on the space shuttle design. The nose and leading edge were coated with reinforced carbon–carbon (RCC), while the lower surface of the fuselage and wing was coated with high-temperature reusable surface insulation (HRSI), and other areas were coated with fibrous refractory composite insulation (FRSI). The TPS type for each surface is depicted in Fig. 4.6.

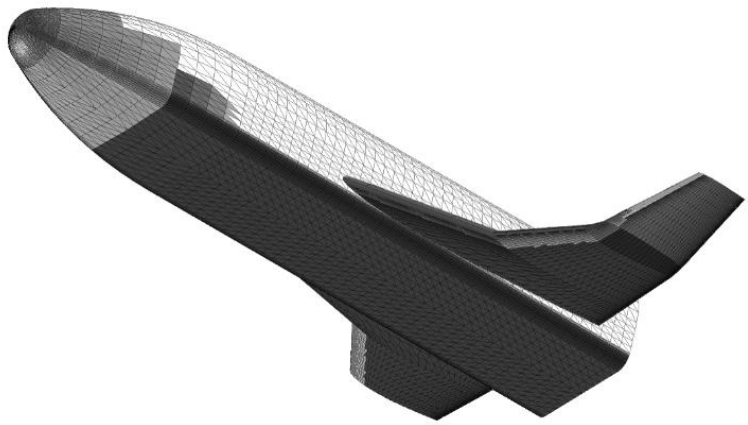

Fig. 4.6 Types of TPS on each surface (gray: RCC, black: HRSI, white: FRSI)

Landing gear weight

The weight of the landing gear consists of the weight of the nose gear, main gear, and associated controls. It varies according to the weight of the vehicle at landing. The calculation for landing gear weight is as follows [5]:

$$W_{\mathrm{gear}} = 0.030 W_{\mathrm{land}} \tag{4.6}$$

where W_{land} is the landing weight of the vehicle

Total structure weight

Thus, the total structural weight is the sum of the fuselage, the wing, the thermal protection system, and the landing gear, as follows:

$$W_{\mathrm{str}} = W_{\mathrm{f}} + W_{\mathrm{w}} + W_{\mathrm{tps}} + W_{\mathrm{gear}} \tag{4.7}$$

Herein, W_{tps} is the TPS weight of the vehicle.

Engine weight

For this study, a main engine is not required for the space vehicle as it is launched into orbit using a separate launch vehicle. However, an orbital maneuvering system and a reaction control system (OMS/RCS) are necessary for the modification of the orbit or attitude of the spacecraft. Based on the required thrust $T_{\mathrm{req_{oms}}}$, $T_{\mathrm{req_p}}$, and $T_{\mathrm{req_v}}$ from propulsion analysis, the OMS/RCS weight is calculated by following equations [5].

OMS engine weight is:

$$W_{\mathrm{oms_{eng}}} = \frac{T_{\mathrm{req_{oms}}}}{R_{\mathrm{oms}}} \tag{4.8}$$

Herein, $W_{\mathrm{oms_{eng}}}$ and $T_{\mathrm{req_{oms}}}$ are OMS engine weight and required thrust, and R_{oms} is the ratio of OMS engine thrust to weight.

$$R_{\mathrm{oms}} = 22 \tag{4.9}$$

The pressurization system for OMS is Ti 6/4 tank with 3000 psia Helium, yield at 400% $P_{\mathrm{oms_{press}}}$, 400 R storage temperature. The weight of the pressurization system for OMS is:

$$W_{\mathrm{oms_{press}}} = 0.0143 P_{\mathrm{oms_{press}}} V_{\mathrm{oms_{press}}}(1 - TRF) + 0.617(V_{\mathrm{oms_{ox}}} + V_{\mathrm{oms_{fuel}}}) \tag{4.10}$$

where $W_{\mathrm{oms_{press}}}$ and $P_{\mathrm{oms_{press}}}$ are the weight and pressure of the pressurization system, and $V_{\mathrm{oms_{press}}}$ are the volume of Helium required as pressurant. TRF is technology reduction factor (in this study, 0.0). $V_{\mathrm{oms_{ox}}}$ and $V_{\mathrm{oms_{fuel}}}$ are the volumes of oxygen and fuel for OMS. $P_{\mathrm{oms_{press}}}$ and $V_{\mathrm{oms_{press}}}$ are given:

$$P_{\mathrm{oms_{press}}} = 3000 \ \ [\mathrm{psia}] \tag{4.11}$$

$$V_{\mathrm{oms_{press}}} = 0.24(V_{\mathrm{oms_{ox}}} + V_{\mathrm{oms_{fuel}}}) \tag{4.12}$$

The installation weight for OMS is:

$$W_{\mathrm{oms_{install}}} = 0.74 W_{\mathrm{oms_{eng}}} \tag{4.13}$$

Thus, the OMS weight is:

$$W_{\mathrm{oms}} = W_{\mathrm{oms_{eng}}} + W_{\mathrm{oms_{install}}} + W_{\mathrm{oms_{press}}} \tag{4.14}$$

RCS thruster weights are:

$$W_{\mathrm{rcs_{pf}}} = N_{\mathrm{pf}} \frac{T_{\mathrm{req_p}}}{R_{\mathrm{p}}} \tag{4.15}$$

$$W_{\mathrm{rcs_{vf}}} = N_{\mathrm{vf}} \frac{T_{\mathrm{req_v}}}{R_{\mathrm{v}}} \tag{4.16}$$

$$W_{\mathrm{rcs_{pa}}} = N_{\mathrm{pa}} \frac{T_{\mathrm{req_p}}}{R_{\mathrm{p}}} \tag{4.17}$$

$$W_{\mathrm{rcs_{va}}} = N_{\mathrm{va}} \frac{T_{\mathrm{req_v}}}{R_{\mathrm{v}}} \tag{4.18}$$

Herein, $W_{\mathrm{rcs_{pf}}}$, $W_{\mathrm{rcs_{vf}}}$, $W_{\mathrm{rcs_{pa}}}$, and $W_{\mathrm{rcs_{va}}}$ are weights of primary and vernier RCS for front and aft of fuselage. N_{pf}, N_{vf}, N_{pa}, and N_{va} are the numbers of primary and vernier RCS for front and aft of fuselage. In this study, N_{pf}, N_{vf}, N_{pa}, and N_{va} are set to 14, 2, 24, and 4 by referring Space Shuttle. $T_{\mathrm{req_p}}$ and $T_{\mathrm{req_v}}$ are the required thrust for primary and vernier RCS, and R_{p} and R_{v} are the thrust to weight of primary and vernier thrusters.

$$R_{\mathrm{p}} = 39.5 \tag{4.19}$$

$$R_{\mathrm{v}} = 9.4 \tag{4.20}$$

The pressurization system for RCS is Ti 6/4 tank with 3000 psia Helium, yield at 400% $P_{\mathrm{rcs_{press}}}$, 400 R storage temperature. The weight of the pressurization system for RCS is:

$$W_{\mathrm{rcs_{press}}} = 0.0143 P_{\mathrm{rcs_{press}}} V_{\mathrm{rcs_{press}}} (1 - TRF) + 0.617(V_{\mathrm{rcs_{ox}}} + V_{\mathrm{rcs_{fuel}}}) \tag{4.21}$$

where $W_{\mathrm{rcs_{press}}}$ and $P_{\mathrm{rcs_{press}}}$ are the weight and pressure of the pressurization system, and $V_{\mathrm{rcs_{press}}}$ are the volume of Helium required as pressurant. TRF is technology reduction factor (in this study, 0.0). $V_{\mathrm{rcs_{ox}}}$ and $V_{\mathrm{rcs_{fuel}}}$ are the volumes of oxygen and fuel for RCS. $P_{\mathrm{rcs_{press}}}$ and $V_{\mathrm{rcs_{press}}}$ are given:

$$P_{\mathrm{rcs_{press}}} = 3000 \ \text{[psia]} \tag{4.22}$$

$$V_{\mathrm{rcs_{press}}} = 0.24(V_{\mathrm{rcs_{ox}}} + V_{\mathrm{rcs_{fuel}}}) \tag{4.23}$$

The installation weight for RCS is:

$$W_{\mathrm{rcs_{install}}} = 0.74(W_{\mathrm{rcs_{pf}}} + W_{\mathrm{rcs_{vf}}} + W_{\mathrm{rcs_{pa}}} + W_{\mathrm{rcs_{va}}}) \tag{4.24}$$

Thus, the RCS weight is:

$$W_{\mathrm{rcs}} = W_{\mathrm{rcs_{pf}}} + W_{\mathrm{rcs_{vf}}} + W_{\mathrm{rcs_{pa}}} + W_{\mathrm{rcs_{va}}} + W_{\mathrm{rcs_{install}}} + \mathrm{W}_{\mathrm{rcs_{press}}} \tag{4.25}$$

The total weight for engine is:

$$W_{\mathrm{eng}} = W_{\mathrm{rcs}} + W_{\mathrm{oms}} \tag{4.26}$$

Tank weight

The tank weight depends on the pressure and volume of the tank. For the weight of OMS and RCS tank is [5]:

$$W_{\mathrm{oms_{tnk}}} = 0.01295 P_{\mathrm{oms_{tnk}}} V_{\mathrm{oms_{tnk}}} \tag{4.27}$$

$$W_{\mathrm{rcs_{tnk}}} = 0.01295 P_{\mathrm{rcs_{tnk}}} V_{\mathrm{rcs_{tnk}}} \tag{4.28}$$

Herein, the pressures of tanks for OMS/RCS ($P_{\mathrm{oms_{tnk}}}$ and $P_{\mathrm{rcs_{tnk}}}$) are set to 195 psia. The total weight of tank is:

$$W_{\mathrm{tnk}} = W_{\mathrm{oms_{tnk}}} + W_{\mathrm{rcs_{tnk}}} \tag{4.29}$$

Total propulsion weight

The total propulsion weight is the weight of the engines plus the weight of the propellant tanks:

$$W_{\mathrm{pros}} = W_{\mathrm{tnk}} + W_{\mathrm{eng}} \tag{4.30}$$

Hydraulic weight

The weight of the hydraulics is defined as:

$$W_{\mathrm{hydr}} = 2.64(\Psi)^{1.0} \tag{4.31}$$

where

$$\Psi = \left| \left(\frac{S_{\mathrm{ref}} Q_{\mathrm{max}}}{1000} \right)^{0.334} \left(L_{\mathrm{b}} + W_{\mathrm{span}} \right)^{0.5} \right| \tag{4.32}$$

Avionics weight

The avionics weight is reduced to 69% of the weight in the original HASA based on the assumption of the advanced avionics system [70]. The weight of the avionics is defined as:

$$W_{\text{tavcs}} = 0.69 \times 66.37\left(W_{\text{gtot}}\right)^{0.361} \tag{4.33}$$

Electrical system weight

The weight of the electrical system is defined as:

$$W_{\text{elect}} = 1.167(\Phi)^{1.0} \tag{4.34}$$

where

$$\Phi = \left|\left(W_{\text{gtot}}\right)^{0.5}(L_{\text{b}})^{0.25}\right| \tag{4.35}$$

Subsystem weight

The total subsystem weight is thus defined as:

$$W_{\text{sub}} = W_{\text{hydr}} + W_{\text{tavcs}} + W_{\text{elect}} \tag{4.36}$$

Payload weight

The payload weight W_{pay} is set to 226.8 kg, and the density of payload is 52.86 kg/m^2 because typical payload densities are about 3.3 lb/ft^3.

Total vehicle gross weight

The total vehicle gross weight is the summation of the total structure, propulsion, subsystem, propellant, and payload weight. Thus, the total vehicle gross weight is defined as:

$$W_{\mathrm{gtot}} = \left(W_{\mathrm{str}} + W_{\mathrm{pros}} + W_{\mathrm{sub}} + W_{\mathrm{prop}} + W_{\mathrm{pay}}\right) \tag{4.37}$$

Herein, the propellant weight W_{prop} is estimated in propulsion analysis.

Weight analysis validation

The weight estimate was compared to that of the Boeing X-37 [71], which contains more fuel than the vehicles designed in this study due to its long-term missions. To ensure a fair comparison, the fuel quantity was set to the actual fuel weight of the X-37. The comparison results are presented in Table 4.2. The original HASA resulted in a large error of 90.3%. In contrast, the modified HASA achieved accurate weight estimation with only a 4.0% error.

Table 4.2 Actual weight of the Boeing X-37 and estimated weight

	Actual weight	Original HASA (error)	Modified HASA (error)
Fuselage weight (kg)		776.6	468.4
Wing weight (kg)		270.8	139.7
Tail wing weight (kg)		183.9	95.0
TPS weight (kg)		122.6	454.8
Landing gear weight (kg)		243.9	99.0
Tank weight (kg)		66.51	187.5
Engine weight (kg)		62.13	808.5
Misc. weight (kg)		5974.3	741.5
Dry weight (kg)		7927.5	3221.2
LH2 weight (kg)		224.9	224.9
LOX weight (kg)		1342.6	1342.6
Gross weight (kg)	4990	9495 (90.3%)	4789 (4.0%)

4.1.3 Propulsion analysis

As described for engine weight, for this study, a main engine is not required for the spacecraft as it is launched into orbit using a separate launch vehicle. However, an orbital maneuvering system and a reaction control system are necessary for the modification of the orbit or attitude of the spacecraft. The OMS/RCS required weights are calculated by following equations [5]:

$$T_{\mathrm{req_{oms}}} = \frac{W_{\mathrm{entry}}}{16} \tag{4.38}$$

$$T_{\mathrm{req_p}} = 870\frac{W_{\mathrm{entry}}L_{\mathrm{f}}}{147141\times143} \tag{4.39}$$

$$T_{\mathrm{req_v}} = 50\frac{W_{\mathrm{entry}}L_{\mathrm{f}}}{147141\times143} \tag{4.40}$$

Herein, $T_{\mathrm{req_{oms}}}$, $T_{\mathrm{req_p}}$, and $T_{\mathrm{req_v}}$ are the required thrust for OMS, primary RCS, and vernier RCS. W_{entry} and L_{f} are the entry weight and fuselage length.

The cryogenic propellant fuel (LOX/LH2) is used for the OMS/RCS, and its weight was determined based on total velocity change possible using OMS/RCS engine and vehicle entry weight. In this study, the specific impulse of OMS and RCS engines (Isp_{oms} and Isp_{rcs}) are set to 246 s and 265 s [5].

The OMS propellant weight for orbit maneuvers is:

$$W_{\mathrm{oms_{prop_{orbit}}}} = W_{\mathrm{entry}}\left[e^{\left(\frac{\Delta V_{\mathrm{oms_{orbit}}}}{Isp_{\mathrm{oms}}\times g}\right)} - 1\right] \tag{4.41}$$

where the total velocity change using OMS for orbit maneuvers is:

$$\Delta V_{\mathrm{oms_{orbit}}} = 50 \ \ [\mathrm{fps}] \tag{4.42}$$

The OMS propellant weight for de-orbit is:

$$W_{\mathrm{oms}_{\mathrm{prop}_{\mathrm{de-orbit}}}} = W_{\mathrm{entry}}\left[e^{\left(\frac{\Delta V_{\mathrm{oms}_{\mathrm{de-orbit}}}}{Isp_{\mathrm{oms}}\times g}\right)} - 1\right] \tag{4.43}$$

where the total velocity change using OMS for de-orbit is:

$$\Delta V_{\mathrm{oms}_{\mathrm{de-orbit}}} = 200 \ \ [\mathrm{fps}] \tag{4.44}$$

The OMS propellant weight for ascent is:

$$W_{\mathrm{oms}_{\mathrm{prop}_{\mathrm{ascent}}}} = W_{\mathrm{entry}}\left[e^{\left(\frac{\Delta V_{\mathrm{oms}_{\mathrm{ascent}}}}{Isp_{\mathrm{oms}}\times g}\right)} - 1\right] \tag{4.45}$$

where the total velocity change using OMS for ascent is:

$$\Delta V_{\mathrm{oms}_{\mathrm{ascent}}} = 650 \ \ [\mathrm{fps}] \tag{4.46}$$

Total OMS propellant weight is with 10% reserve propellant

$$W_{\mathrm{oms}_{\mathrm{prop}}} = 1.1\left(W_{\mathrm{oms}_{\mathrm{prop}_{\mathrm{orbit}}}} + W_{\mathrm{oms}_{\mathrm{prop}_{\mathrm{de-orbit}}}} + W_{\mathrm{oms}_{\mathrm{prop}_{\mathrm{ascent}}}}\right) \tag{4.47}$$

The ratio between oxygen and fuel for OMS propellant was 6:1. Thus,

$$W_{\mathrm{oms}_{\mathrm{ox}}} = 6/7\, W_{\mathrm{oms}_{\mathrm{prop}}} \tag{4.48}$$

$$W_{\mathrm{oms}_{\mathrm{fuel}}} = 1/7\, W_{\mathrm{oms}_{\mathrm{prop}}} \tag{4.49}$$

where, $W_{\mathrm{oms}_{\mathrm{ox}}}$ and $W_{\mathrm{oms}_{\mathrm{fuel}}}$ are the weights of the oxygen and fuel for OMS.

The RCS propellant weight for entry is:

$$W_{\mathrm{rcs}_{\mathrm{prop}_{\mathrm{entry}}}} = W_{\mathrm{entry}}\left[e^{\left(\frac{\Delta V_{\mathrm{rcs}_{\mathrm{entry}}}}{Isp_{\mathrm{rcs}}\times g}\right)} - 1\right] \tag{4.50}$$

where the total velocity change using RCS for entry is:

$$\Delta V_{\mathrm{rcs}_{\mathrm{entry}}} = 40 \ \ [\mathrm{fps}] \tag{4.51}$$

The RCS propellant weight on orbit is:

$$W_{\mathrm{rcs}_{\mathrm{prop}_{\mathrm{orbit}}}} = W_{\mathrm{entry}} \left[e^{\left(\frac{\Delta V_{\mathrm{rcs}_{\mathrm{orbit}}}}{Isp_{\mathrm{rcs}} \times g} \right)} - 1 \right] \tag{4.52}$$

where the total velocity change using RCS on orbit is:

$$\Delta V_{\mathrm{rcs}_{\mathrm{orbit}}} = 200 \ \ [\mathrm{fps}] \tag{4.53}$$

Total RCS propellant weight is also with 10% reserve propellant

$$W_{\mathrm{rcs}_{\mathrm{prop}}} = 1.1 \left(W_{\mathrm{rcs}_{\mathrm{prop}_{\mathrm{entry}}}} + W_{\mathrm{rcs}_{\mathrm{prop}_{\mathrm{orbit}}}} \right) \tag{4.54}$$

The ratio between oxygen and fuel for RCS propellant was 4:1. Thus,

$$W_{\mathrm{rcs}_{\mathrm{ox}}} = 4/5 \, W_{\mathrm{oms}_{\mathrm{prop}}} \tag{4.55}$$

$$W_{\mathrm{rcs}_{\mathrm{fuel}}} = 1/5 \, W_{\mathrm{oms}_{\mathrm{prop}}} \tag{4.56}$$

where, $W_{\mathrm{rcs}_{\mathrm{ox}}}$ and $W_{\mathrm{rcs}_{\mathrm{fuel}}}$ are the weights of the oxygen and fuel for RCS.

The total propellant weight W_{prop} is:

$$W_{\mathrm{prop}} = W_{\mathrm{oms}_{\mathrm{prop}}} + W_{\mathrm{rcs}_{\mathrm{prop}}} \tag{4.57}$$

and The total oxygen and fuel weights are:

$$W_{\mathrm{ox}} = W_{\mathrm{oms}_{\mathrm{ox}}} + W_{\mathrm{rcs}_{\mathrm{ox}}} \tag{4.58}$$

$$W_{\mathrm{fuel}} = W_{\mathrm{oms}_{\mathrm{fuel}}} + W_{\mathrm{rcs}_{\mathrm{fuel}}} \tag{4.59}$$

The tanks for the fuel consist of a cylinder with dome-shaped ends, and their radius is the same as that of the circle tangent to the body section, as depicted in Fig. 4.7.

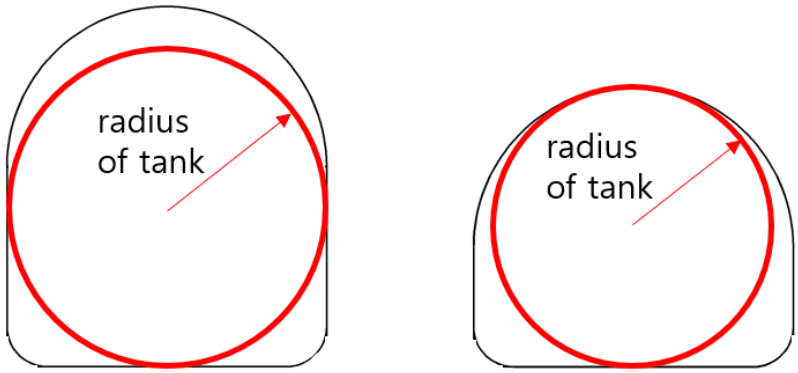

Fig. 4.7 Radius of tank

4.1.4 Aerothermodynamic analysis

Aerodynamics

During the reentry, the spacecraft goes through various speeds ranging from hypersonic to subsonic. The aerodynamic characteristics of the vehicle were determined using modified Newtonian theory for hypersonic and supersonic flight regimes [72], and Digital DATCOM for the subsonic flight regime [73].

The determination of the angle between the direction of free stream velocity and the surface of the vehicle is necessary in the modified Newtonian theory. This angle can be computed using the following equation.

$$\theta = \frac{\pi}{2} - \cos^{-1}\frac{-\boldsymbol{n}\cdot\boldsymbol{V}_\infty}{|\boldsymbol{n}||\boldsymbol{V}_\infty|} \tag{4.60}$$

The equation involves the normal vector $\boldsymbol{n}$ for each surface panel and the free stream velocity vector $\boldsymbol{V}_\infty$. The surface panels are categorized as either windward ($\theta > 0$) or leeward ($\theta < 0$) panels.

The modified Newtonian method is utilized to calculate the windward pressure

coefficients, while $C_{\mathrm{p}} = 0$ is used for the leeward pressure coefficients, as shown in Fig. 4.8. The modified Newtonian formula used is as follows:

$$C_p = C_{p_{max}} \sin^2 \theta \tag{4.61}$$

where $C_{p_{max}}$ is the maximum value of the pressure coefficient by using normal shock relation and isentropic relation, as follows:

$$C_{p_{max}} = \frac{2}{\gamma M_\infty^2}\left[\left\{\frac{(\gamma+1)^2 M_\infty^2}{4\gamma M_\infty^2 - 2(\gamma-1)}\right\}^{\gamma/(\gamma-1)}\left\{\frac{1-\gamma+2\gamma M_\infty^2}{\gamma+1}\right\} - 1\right] \tag{4.62}$$

Herein, γ is the specific heat ratio. This theory determines the surface pressure and computes the magnitude of surface velocity by converting the normal velocity on the surface into pressure. Furthermore, the direction of surface velocity is obtained as follows:

$$\frac{\boldsymbol{V}}{|\boldsymbol{V}|} = \frac{\boldsymbol{n}\times\boldsymbol{V}_\infty\times\boldsymbol{n}}{|\boldsymbol{n}\times\boldsymbol{V}_\infty\times\boldsymbol{n}|} \tag{4.63}$$

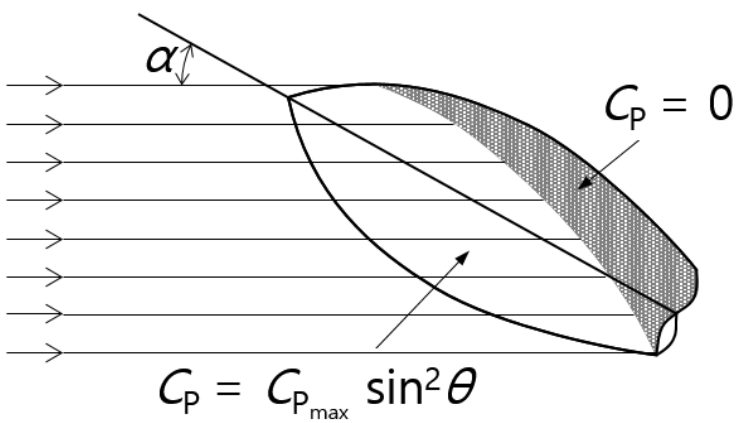

Fig. 4.8 Modified Newtonian theory

The altitude and velocity obtained from the trajectory analysis were utilized to calculate the aerodynamic force. The aerodynamic analysis also assessed the longitudinal stability and trim condition by considering the pitching moments. Ensuring longitudinal stability and trim condition is an important constraint. The pressure distribution and center of gravity, obtained from the weight analysis, were used to determine whether the longitudinal stability and trim condition can be satisfied. The angle of attack, which is used to evaluate the aerodynamic force, varies depending on the Mach number. The angle of attack corresponding to a specific Mach number is depicted in Fig. 4.9 [74].

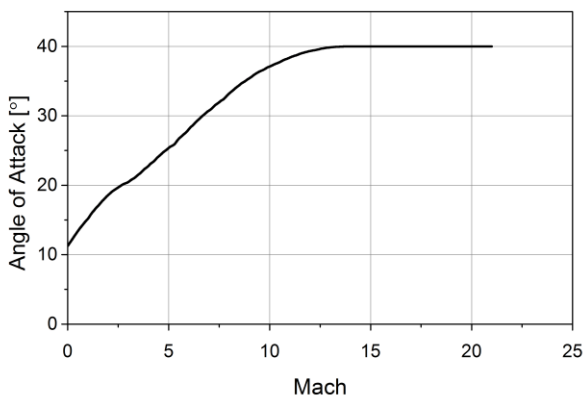

Fig. 4.9 Pre-described angle of attack according to the Mach number

Heat-flux calculation

Using the flow properties, an estimation of the surface heat flux was made using the approximate-convective-heating equation [7,75,76]. The first step in estimating the heat flux using the approximate convective-heating equations involves calculating the streamline. Once the streamline is obtained, the heat flux can be predicted at each point along the streamline from the stagnation point to the endpoint

(seed). To avoid the unrealistic heat flux pattern near the stagnation point, caused by the velocity singularity at that point, a surface curve called the ε-curve was introduced [76]. This curve is perpendicular to the inviscid surface streamlines and encircles the stagnation point. If the point is located inside the ε-curve, the heat flux is determined by interpolating the heat flux at the stagnation point on the ε-curve. However, if the point is located outside the ε-curve, the properties of the boundary layer edge are calculated using the modified Newtonian theory. The streamline metric and momentum thickness are then computed from these properties. Finally, the heat flux at the point is estimated from the computed momentum thickness. Figure 4.10 illustrates this procedure.

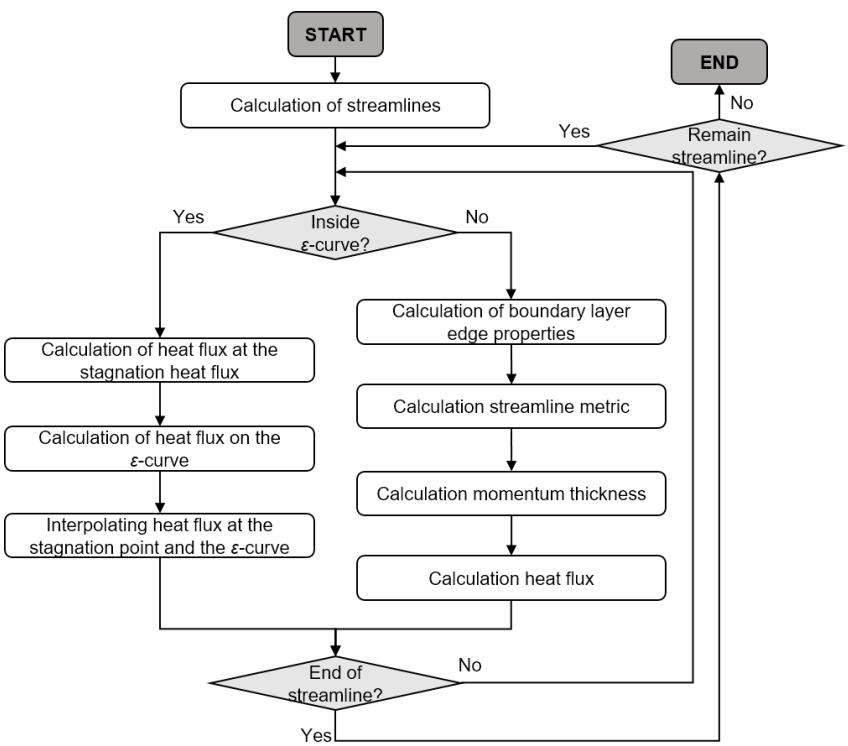

Fig. 4.10 Heat-flux calculation procedure

Streamline calculation

The approximate convective-heating equations estimate the heat flux along a streamline, which necessitates the use of inviscid surface streamlines. To obtain these streamlines, two integration methods are available: forward integration and backward integration. In forward integration, the streamline segments are integrated from the stagnation point along the surface velocity direction, while in backward integration, they are integrated from seeds (starting points of streamline calculation) in the opposite direction to that of surface velocity. The results of both methods are similar for simple geometries such as a sphere, ellipsoid, and spherically blunted cone. However, in complex geometries like wing-body configurations, the streamline using forward integration is not well distributed, as the differences in the well-distributed streamlines are overly small near the stagnation point. Hence, this study employs backward integration.

To calculate the streamline, a candidate point is selected at a short distance from to the endpoint of the streamline in the opposite direction of the surface velocity using Eq. (4.63). If the candidate point falls within the same grid as the endpoint, it replaces the new endpoint. Otherwise, the candidate point is projected onto the plane that contains other grids [77], and it is checked if it falls within the same grid. If the projected point is within the grid, it replaces the endpoint. This process is repeated from the seed point to the stagnation point.

To distribute the streamline over the entire wing and body, the midpoints of all grids that contain the trailing edge of the wing or the aft of the body are selected as seeds for streamline calculation. This approach results in a well-distributed streamline on both the wing and body, as shown in Fig. 4.11.

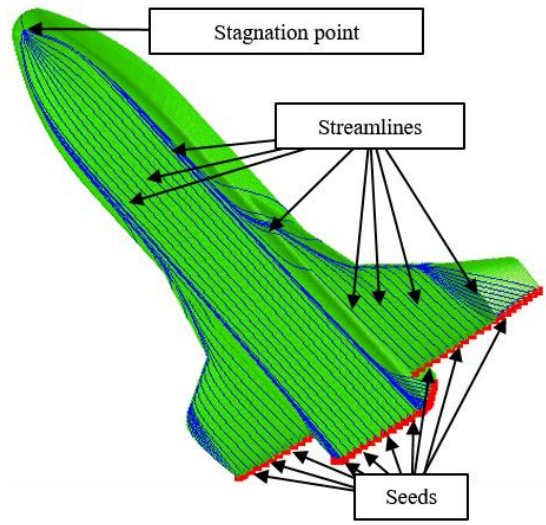

Fig. 4.11 Seeds and streamlines for backward integration

Streamline metrics

The coordinates used on the surface to determine the inviscid streamline were ξ and β, which are illustrated in Fig. 4.12. ξ denotes the position along the streamline, while β represents the position perpendicular to the streamline [7].

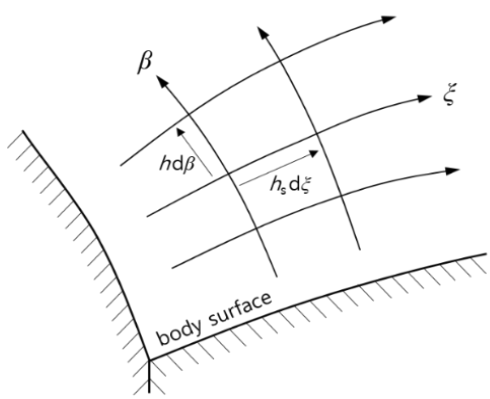

Fig. 4.12 Inviscid surface streamline coordinate system

The differentials of the arc lengths on the surface were expressed as $\mathrm{d}s = h_s\mathrm{d}\xi$ and $\mathrm{d}s_\perp = h\mathrm{d}\beta$, while the differential of the position vector ($\mathrm{d}\boldsymbol{R}$) on the surface was

written as follows:

$$\mathrm{d}\boldsymbol{R} = h_{\mathrm{s}}\mathrm{d}\xi\widehat{\boldsymbol{e}_{\mathrm{s}}} + h\mathrm{d}\beta\widehat{\boldsymbol{e}_{\perp}} \tag{4.64}$$

The equation shows the differential of the position vector on the surface, expressed as $\mathrm{d}\boldsymbol{R}$. The metric coefficients, h_{s} and h, correspond to ξ and β, respectively, while $\widehat{\boldsymbol{e}_{\mathrm{s}}}$ and $\widehat{\boldsymbol{e}_{\perp}}$ are unit vectors in the direction of the streamline and perpendicular to it on the surface. The metric coefficient h represents the convergence or divergence of streamlines, and in the case of an axisymmetric flow, it is equivalent to the local radius of the body.

To apply the axisymmetric analogy [78], the metric of the streamline h needs to be calculated to replace the radius of the equivalent axisymmetric body. An efficient method of calculating h was used, which relied on only two independent variables in Cartesian coordinates (x, y, z) for integration. When selecting (y, z), where $v = v(y, z)$ and $w = w(y, z)$, the streamline metric was computed according to the following formula [76]:

$$h = \frac{|\nabla \boldsymbol{F}|}{\boldsymbol{F}_x|\boldsymbol{V}|}\left[w\left(\frac{\partial y}{\partial \beta}\right)_z\right] \tag{4.65}$$

The surface of the body is represented by $F(x, y, z) = 0$, and the normal vector to the surface is denoted by $\nabla F = \left(F_x, F_y, F_z\right)^{\mathrm{T}}$. The partial derivative can be expressed as a differential equation:

$$\frac{\mathrm{d}}{\mathrm{d}s}\left[w\left(\frac{\partial y}{\partial \beta}\right)_z\right] = \frac{1}{|\boldsymbol{V}|}\left[w\left(\frac{\partial y}{\partial \beta}\right)_z\right]\left[\frac{\partial v}{\partial y} + \frac{\partial w}{\partial z}\right] \tag{4.66}$$

Herein, s is the distance along the streamline on the surface. Equations for the independent variables (x, y) and (x, z) were derived as follow [4].

$$h = \frac{|\nabla \boldsymbol{F}|}{\boldsymbol{F}_z |\boldsymbol{V}|}\left[u\left(\frac{\partial y}{\partial \beta}\right)_x\right] \tag{4.65a}$$

$$\frac{\mathrm{d}}{\mathrm{d}s}\left[u\left(\frac{\partial y}{\partial \beta}\right)_x\right] = \frac{1}{|\boldsymbol{V}|}\left[u\left(\frac{\partial y}{\partial \beta}\right)_x\right]\left[\frac{\partial u}{\partial x} + \frac{\partial v}{\partial y}\right] \tag{4.66a}$$

$$h = \frac{|\nabla \boldsymbol{F}|}{\boldsymbol{F}_y |\boldsymbol{V}|}\left[u\left(\frac{\partial z}{\partial \beta}\right)_x\right] \tag{4.65b}$$

$$\frac{\mathrm{d}}{\mathrm{d}s}\left[u\left(\frac{\partial z}{\partial \beta}\right)_x\right] = \frac{1}{|\boldsymbol{V}|}\left[u\left(\frac{\partial z}{\partial \beta}\right)_x\right]\left[\frac{\partial u}{\partial x} + \frac{\partial w}{\partial z}\right] \tag{4.66b}$$

As the denominator in Eqs. (4.65), (4.65a), and (4.65b) contains a component of the surface normal vector ∇F, the integration variables were selected to maximize this component.

Heating equations

Zoby et al. [6] proposed approximate convective-heating equations to compute heat flux on the surface. In conditions above 50 km altitude, laminar flow is the dominant flow condition [79]. As reentry vehicles spend most of their time above this altitude, the flow is assumed to be mostly laminar under these flight conditions [80,81]. For laminar flow,

$$\dot{q}_{\mathrm{w,L}} = 0.22\left(Re_{\theta,\mathrm{e}}\right)^{-1}\left(\frac{\rho^*}{\rho_\mathrm{e}}\right)\left(\frac{\mu^*}{\mu_\mathrm{e}}\right)\rho_\mathrm{e} u_\mathrm{e}(H_\mathrm{aw} - H_\mathrm{w})(Pr_\mathrm{w})^{-0.6} \tag{4.67}$$

The heat flux on the surface is denoted by $\dot{q}_{\mathrm{w,L}}$, and the momentum thickness Reynolds number and Prandtl number are represented by Re_θ and Pr_w, respectively. Density, viscosity, velocity, and enthalpy are denoted by ρ, μ, u, and H, respectively. Subscripts (e), (w), and (aw) represent estimations at the boundary layer edge, wall, and adiabatic wall, respectively. The superscript (*) indicates that

evaluations are done by Eckert's reference enthalpy relation [82] to consider compressible effects.

The calculation of the laminar momentum thickness θ_{L} was performed using the following equation:

$$\theta_{\mathrm{L}} = 0.664\left(\int_0^s \rho^* \mu^* u_{\mathrm{e}} h^2 \mathrm{d}s\right)^{\frac{1}{2}} / (\rho_{\mathrm{e}} \mu_{\mathrm{e}} h) \tag{4.68}$$

The correction equation proposed by Kemp et al. was used to consider the effect of the velocity gradient on laminar heating in the following equation:

$$\bar{\theta}_{\mathrm{L}} = \frac{\theta_{\mathrm{L}}}{1+0.09\sqrt{\bar{\psi}}} \tag{4.69}$$

Therefore, before computing the laminar heating, the mean momentum thickness, denoted as $\bar{\theta}_{\mathrm{L}}$ in Eq. (4.68), was substituted for θ_{L} in Eq. (4.69). The velocity gradient parameter $\bar{\psi}$ was defined as follows:

$$\bar{\psi} = \frac{2\zeta}{u_{\mathrm{e}}}\left[\left(\frac{\mathrm{d}u_{\mathrm{e}}}{\mathrm{d}s}\right) / \left(\frac{\mathrm{d}\zeta}{\mathrm{d}s}\right)\right] \tag{4.70}$$

The parameter ζ, which was determined by the Lees-Dorodnisyn transformation [83], was represented as follows:

$$\zeta = \int_0^s \rho_{\mathrm{w}} \mu_{\mathrm{w}} u_{\mathrm{e}} h^2 \mathrm{d}s \tag{4.71}$$

Heat flux near the stagnation point

The heat flux at the stagnation point could not be computed using the above-mentioned approximate convective-heating equations since the integration process begins from the stagnation point. Therefore, the heat flux at the stagnation point was determined using the following equation:

$$\dot{q}_{\mathrm{w,s}} = 0.767\sqrt{\frac{\mathrm{d}u_{\mathrm{e}}}{\mathrm{d}x}}(\rho\mu)^{0.5}(H_{\mathrm{s}} - H_{\mathrm{w}})(Pr_{\mathrm{w}})^{-0.6} \tag{4.72}$$

The subscript (s) is used to indicate properties at the stagnation point, and the gradient of velocity at the stagnation point is represented by $\mathrm{d}u_{\mathrm{e}}/\mathrm{d}x$. DeJarnette et al. proposed the following equation to calculate the gradient [84]:

$$\frac{\mathrm{d}u_{\mathrm{e}}}{\mathrm{d}x} = \frac{|V_\infty|}{R}\sqrt{1.85\frac{\rho_\infty}{\rho_{\mathrm{s}}}} \tag{4.73}$$

Near the stagnation point, the assumption of the similar ($\rho^*\mu^*$) and the linear u_{e} and h along a streamline could be utilized. This approximation led to a replacement of the integration for calculating the momentum thickness θ_{L} on the ε-curve with the following expression:

$$\int_0^{s_\varepsilon} \rho^*\mu^* u_{\mathrm{e}} h^2 \mathrm{d}s = (\rho^*\mu^*)_{\mathrm{s}}(u_{\mathrm{e}})_\varepsilon h_\varepsilon^2 \frac{S_\varepsilon}{4} \tag{4.74}$$

To calculate the heat flux on the ε-curve, integration was not necessary as the momentum thickness on the ε-curve was obtained using Eq. (4.74). The heat flux inside the ε-curve was determined by interpolating the heat flux at the stagnation point and the ε-curve.

Heat-flux calculation validation

In order to verify the accuracy of the approximate convective-heating equations applied in this study, a comparison was made between the heat flux on a sphere with a 0.0508-m radius obtained from these equations and the experimental results [85] and a high-fidelity computational fluid dynamics (CFD) approach that utilized the Reynolds-averaged Navier-Stokes (RANS) solver. For the RANS solver, ANSYS Fluent, a commercial CFD software package, was utilized for the laminar and steady-

state flows. The RANS solver was implemented with the implicit AUSM+ flux [86], Green-Gauss node-based gradient [87], and a combination of first- and second-order upwind schemes. The conditions for the sphere's freestream and wall are presented in Table 4.3. The heat flux obtained from the approximate convective-heating equations agreed well with the results obtained from the other methods, as illustrated in Fig. 4.13.

Table 4.3 Freestream and wall conditions for the sphere

	Value
M_∞	9.74
γ	1.4 (Perfect gas)
ρ_∞	0.004272 kg/m^3
T_∞	53.17 K
T_w	300.0 K

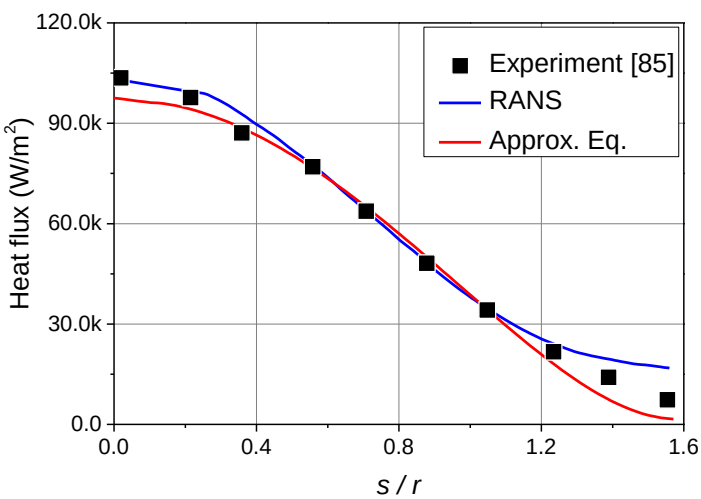

Fig. 4.13 Convective heat flux for the sphere

Additionally, the convective heat fluxes on a wing-body configuration were computed and compared using both the RANS and approximate convective heating equations to examine the accuracy of the latter for more complex geometries. The Korea Aerospace Research Institute's KSP-1 vehicle, which has a 7-m fuselage and 4-m span wing and is depicted in Fig. 4.14, was utilized for this study. The freestream and wall conditions for the KSP-1 were described in Table 4.4. To perform the RANS calculation, an unstructured hybrid mesh with approximately 10,000,000 nodes and 50 prism layers was utilized, as shown in Fig. 4.15. The body surface was discretized into 80 longitudinal and 58 cross-sectional grids, while the wing surface was discretized into 20 span-wise and 128 airfoil grids, for the approximate convective-heating equations calculations.

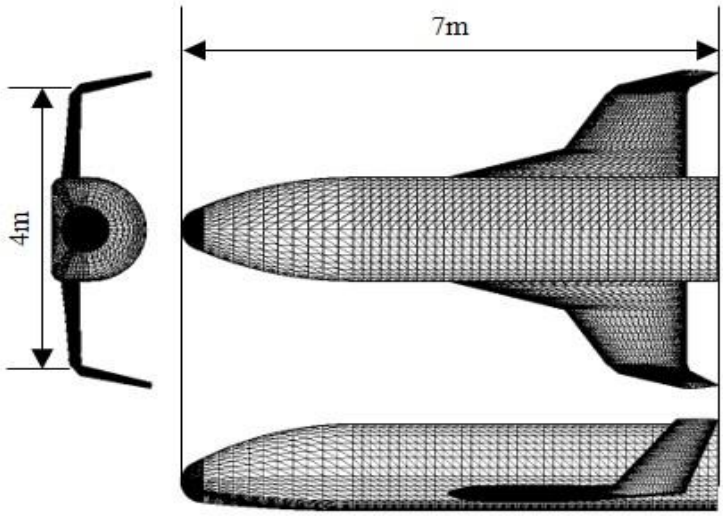

Fig. 4.14 KSP-1 geometry

Table 4.4 Freestream and wall conditions for KSP-1

	Value
M_∞	20.0
γ	1.4
α	40°
ρ_∞	0.000568 kg/m^3
T_∞	260.772 K
T_w	300.0 K

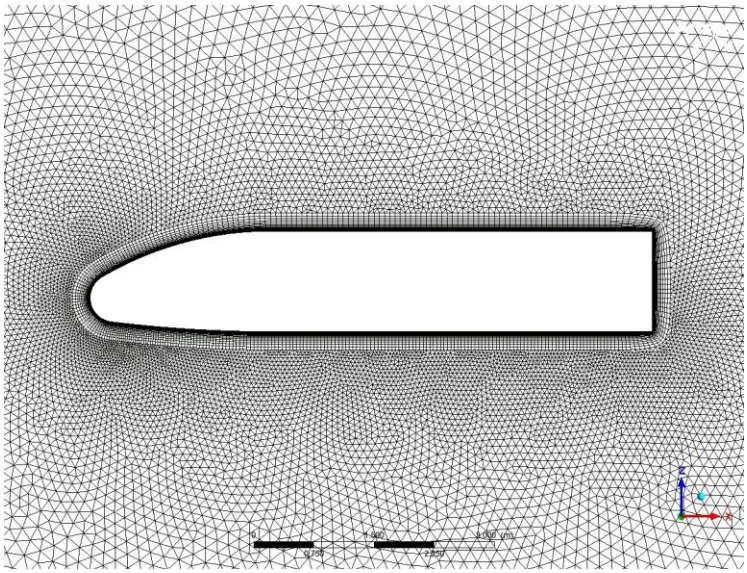

Fig. 4.15 Computational mesh for RANS at the symmetric plane

The results obtained from the RANS and approximate convective-heating equations are comparable, as illustrated in Fig. 4.16. A detailed comparison was conducted by plotting the heat fluxes along the wing section of 1.85 m, as depicted in Fig. 4.17. The peaks of the heat fluxes are in reasonable agreement, and the trends of the heat fluxes with changes in the x-coordinates are comparable. The heat flux

calculations obtained from the sphere and KSP-1 models demonstrate that the approximate convective-heating equations employed in this study are sufficiently accurate for heat flux calculations.

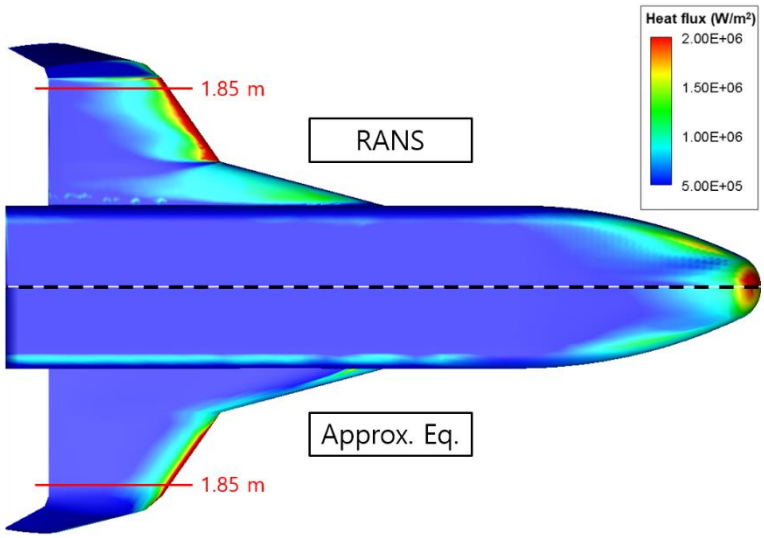

Fig. 4.16 KSP-1 heat fluxes using RANS and the approximate convective-heating equations (the upper portion is RANS, and the lower portion is the approximate convective-heating equations)

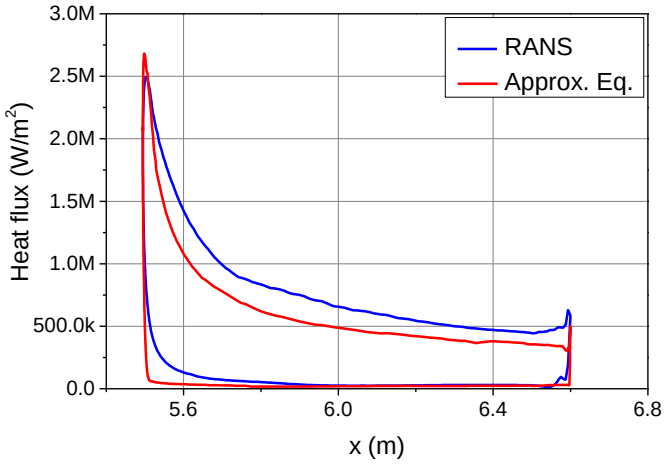

Fig. 4.17 Heat fluxes along the 1.85-m wing section

4.1.5 Trajectory analysis

The trajectory analysis in this study only covers the period from orbit to landing because the launch vehicle is responsible for placing the vehicle into orbit, using a three-degree-of-freedom (3DOF) trajectory analysis [88] incorporating the weight and aerodynamic force of the vehicle.

The gravity and aerodynamic force of the present position were used to determine the next position and velocity. Then, the position and velocity were utilized to calculate the aerodynamic force at the current position. Time integral was carried out using the 4th Runge-Kutta (RK) method, as follows:

$$\dot{X}^{(1)} = f(X^n, t) \tag{4.75a}$$

$$\dot{X}^{(2)} = f(X^n + 0.5\Delta t\dot{X}^{(1)}, t + 0.5\Delta t) \tag{4.75b}$$

$$\dot{X}^{(3)} = f(X^n + 0.5\Delta t\dot{X}^{(2)}, t + 0.5\Delta t) \tag{4.75c}$$

$$\dot{X}^{(4)} = f(X^n + 0.5\Delta t\dot{X}^{(3)}, t + \Delta t) \tag{4.75d}$$

$$X^{n+1} = X^n + \frac{\Delta t\left(\dot{X}^{(1)} + 2\dot{X}^{(2)} + 2\dot{X}^{(3)} + \dot{X}^{(4)}\right)}{6} \tag{4.75}$$

where $X = [u \;\; v \;\; w \;\; x \;\; y \;\; z]^{\mathrm{T}}$ in Earth-centered inertial coordinate.

In this study, four coordinate system was employed for describing motion and position [89,90]. Body-fixed coordinate system (BFCS) is defined using node point as orientation.

The Earth-centered inertial (ECI) coordinate system utilizes Cartesian coordinates with its origin located at the center of mass of Earth and fixed with respect to the stars, as shown in Fig. 4.18. The *x*-*y* plane of the system coincides with Earth's equatorial plane, while the *x*-axis remains permanently fixed in a direction

relative to the celestial sphere that does not rotate as Earth does. The *z*-axis is perpendicular to the equatorial plane and extends through the North Pole. It is noteworthy that while Earth rotates, the ECI coordinate system remains stationary. As remaining stationary using Cartesian coordinate, it is easy to apply the equation of motion.

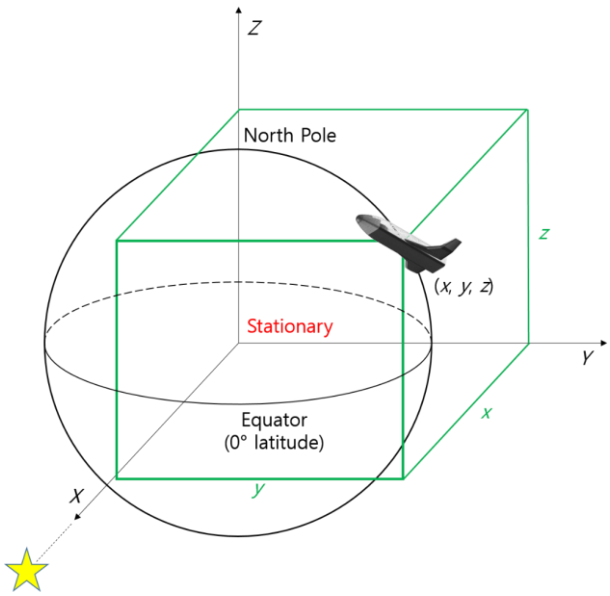

Fig. 4.18 ECI coordinate

The Earth-centered, Earth-fixed coordinate system (ECEF) is a type of Cartesian spatial reference system that represents positions near the Earth using *X*, *Y*, and *Z* measurements from its center of mass, as illustrated in Fig. 4.19. It is commonly used for tracking satellite orbits and in satellite navigation systems for determining locations on the Earth's surface. Unlike ECI, the ECEF is rotating along with the Earth.

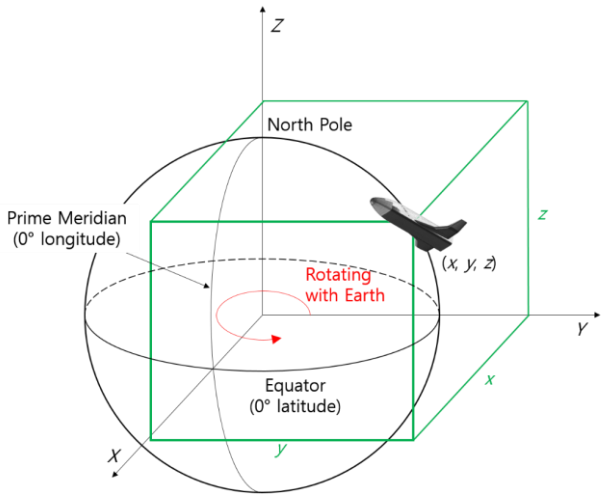

Fig. 4.19 ECEF coordinate

The geographic coordinate system (GCS) is a type of spherical coordinate system used to determine and communicate positions on the Earth using latitude and longitude. It is the most widely used spatial reference system and serves as the foundation for many others. Unlike a Cartesian coordinate system, the geographic coordinate system is not planar because latitude and longitude measurements are angles.

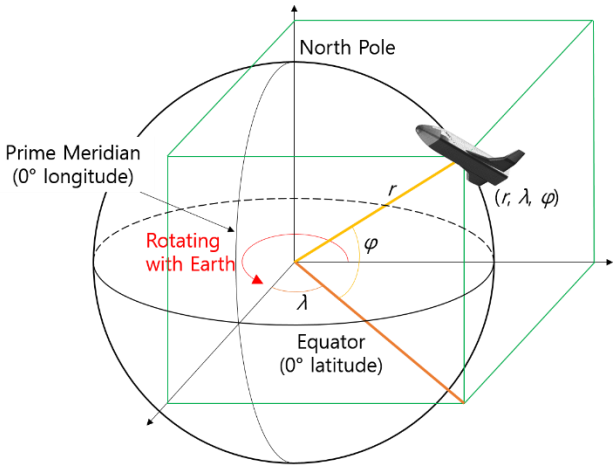

Fig. 4.20 GCS coordinate

The flow chart illustrating the trajectory analysis procedure is shown in Fig. 4.21. The detailed process for trajectory analysis, which includes coordinate conversion, is as follows:

Step 1: Input the initial position and velocity in GCS.

Step 2: Convert the initial properties to ECI to apply them to the equation of motion, as the equation on ECI is more convenient because of stationary Cartesian coordinates.

Step 3: Obtain the aerodynamic force in BFCS based on the position and velocity of the spacecraft through aerothermodynamic analysis.

Step 4: Convert the aerodynamic force to ECI to apply it to the equation of motion.

Step 5: Conduct time integral to calculate the new position and velocity using the 4th orther Runge-Kutta (RK) method.

Step 6: Convert the new position and velocity to ECEF to account for Earth's rotation.

Step 7: Convert the new position and velocity to GCS, as GCS is more familiar by using altitude, longitude, and latitude to describe the position.

Step 8: Repeat step 3–7 until the spacecraft land

To verify the trajectory analysis, the trajectory of KSP-1 was analyzed, beginning at a height of 300 km, with a velocity of 7000 m/s, an inclination angle of 80°, and a flight path angle of 0°. Table 4.5 provides a summary of the initial trajectory conditions. The trajectory was calculated appropriately, as illustrated in Fig. 4.22.

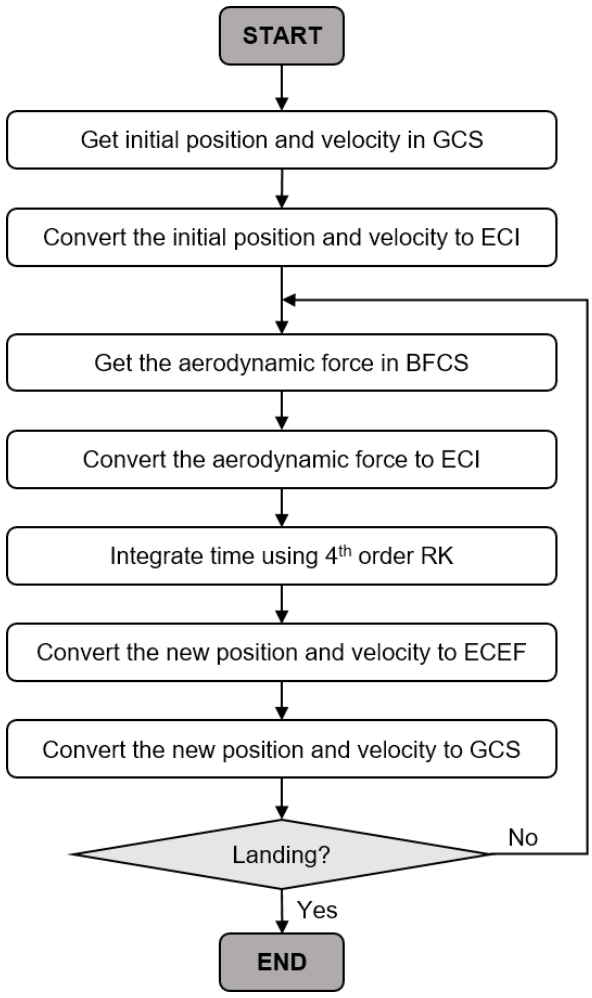

Fig. 4.21 Flow chart of trajectory analysis

Table 4.5 Initial trajectory condition of KSP-1

Initial trajectory condition	Value
Altitude	300 km
Velocity	7000 m/s
Flight path angle	0°
Incline angle	80°

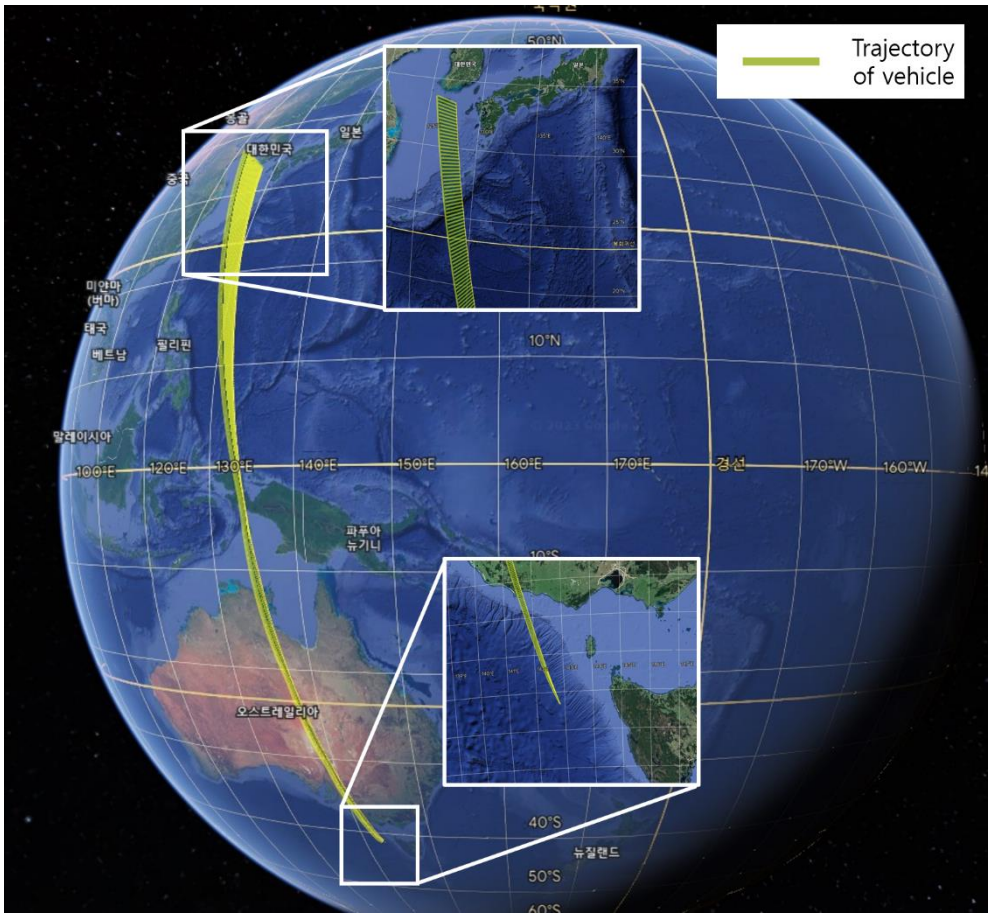

Fig. 4.22 Trajectory of KSP-1

4.2 Problem definition

To evaluate the performance of the spacecraft, multidisciplinary optimization described in Chapter 2 was employed. The spacecraft's trajectory began at a height of 300 km, with a velocity of 7000 m/s, an inclination angle of 80°, and a flight path angle of 0°. Table 4.6 provides a summary of the initial trajectory conditions.

Table 4.6 Initial trajectory condition

Initial trajectory condition	Value
Altitude	300 km
Velocity	7000 m/s
Flight path angle	0°
Incline angle	80°

The optimization problem was set as follows:

Minimize	Weight and standard deviation (SD) of the heat flux
Constraint	Unrealistic geometry
	(i.e., tank length < fuselage length, nose radius > 0.01 m)
	Maximum dynamic pressure < 50 kPa
	Maximum heat flux < 4 MW/m2
	Landing speed < 20 m/s
	Trim condition (the ability to maintain C_m = 0)
	Longitudinal stability (static margin > 0)
Side constraint	Geometrical constraints
	(i.e., wing span < 5 m, total length < 10 m)

(4.76)

The minimization of the weight is to reduce the payload of the launch vehicle that will load the spacecraft. The minimization of the SD of heat flux is for diminishing the heat flux on the spacecraft. If the maximum heat flux of the spacecraft is minimized as an objective function, a specific point (i.e., the stagnation point or the leading edge) of the spacecraft will be affected. However, minimizing of the SD of heat flux can consider a large area that has a high heat flux. Therefore, these two objective functions were selected in this study. The Appendix provides a detailed description of the initial design space and side constraints.

For the optimization process, the MOGA algorithm was run with 256 individuals for 600 generations. The design space was updated every 100 generations using feasible solutions obtained in the last 20 generations, with η_{t} and n set to 99% and 20, respectively. To maintain population diversity, reinitialization was performed while retaining the extreme solutions after adapting the design space. In addition, optimization was conducted with and without reinitialization using the fixed design space to assess the effectiveness of this approach.

4.3 Results

To validate the effectiveness of the developed adaptive time-step method, the numbers of heat-flux calculations were counted for optimization processes. The number of the calculations with the adaptive time-step method is approximately 14 million, while the number of the calculations without the method is 185 million, as shown in Table 4.7. The number of the calculation is reduced over one-tenth with the developed adaptive time-step method.

Table 4.7 The number of heat-flux calculations for the optimizations

	Without adaptive time step for heat flux	With adaptive time step for heat flux
heat-flux calculation (Normal dist.)	185,072,122	14,415,674
heat-flux calculation (developed method)	185,063,669	14,413,916

Figure 4.23 displays the Pareto solutions generated by the method assuming normal distributions, the developed adaptive design-space method, and the fixed design space. The Pareto solutions obtained by the developed method outperformed the other methods. On the other hand, the Pareto solutions produced by the method assuming normal distributions were comparable to those achieved with the fixed design space. Theoretically, the Pareto solutions obtained by any method upon convergence should be the same. However, in a practical problem, the Pareto solutions may differ across the design space due to variations in the probability of finding solutions during the stochastic optimization process. Therefore, adjusting the design space to a region where the probability density of feasible solutions is high can improve the searchability of the MOGA.

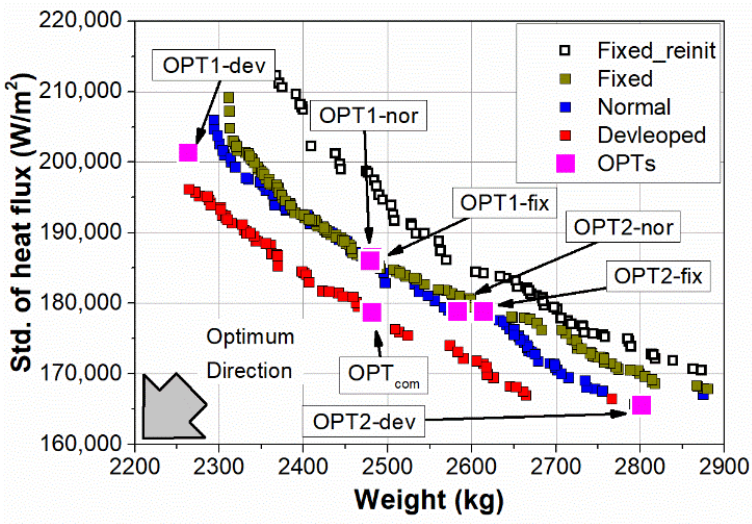

Fig. 4.23 Pareto solutions and OPTs

Figure 4.24 indicates that the majority of the adapted design variable ranges achieved with the developed method were narrower than those obtained with the method that assumes normal distributions. This finding aligns with the characteristics identified through analyses of the test problems. In Fig. 4.24, the adaptive design space of x_{11}, which represents the outboard sweep angle, is depicted as a point. The reason behind low surface pressure at larger sweep angles is the low angle between the flow and the surface. As a result of this low pressure, the optimization leads to a large value of this variable, as it generates a low heat flux on the surface. Additionally, the weight of the wing can be reduced with a larger sweep angle as it results in a smaller tip-chord length. However, there is a geometrical constraint that limits x_{11} to be smaller than 50. Consequently, the adaptive design space of x_{11} converged close to 50. The adaptive design space of x_{19} and x_{22} did not overlap with the initial design space because a large x_{19}, which represents the winglet sweep angle, produces low heat flux as discussed for x_{11}. On the other hand,

a small x_{22}, which represents the winglet length, results in a lighter winglet. Consequently, the adaptive-design-space method can effectively optimize the design space and enhance the performance of unmanned spacecraft.

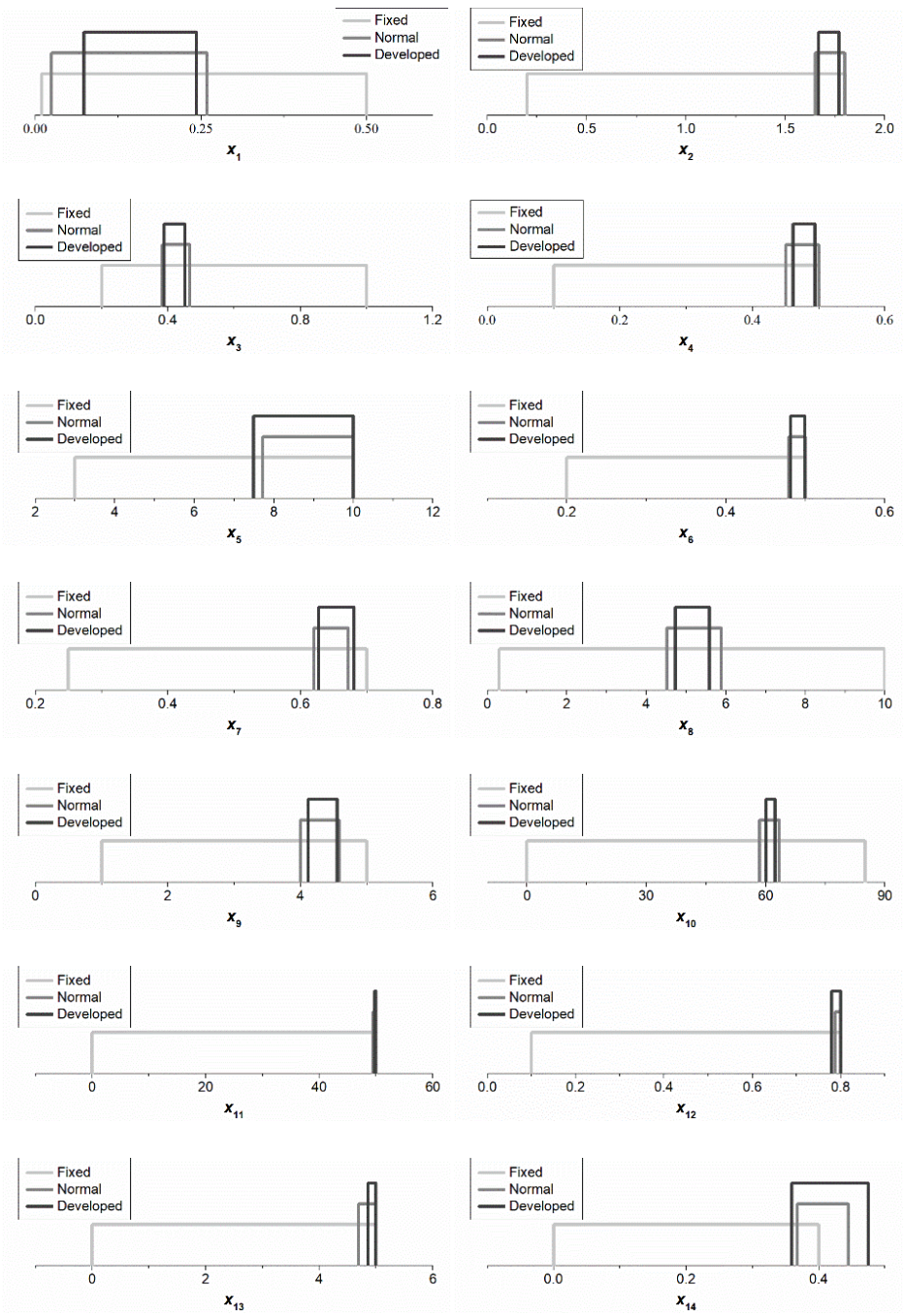

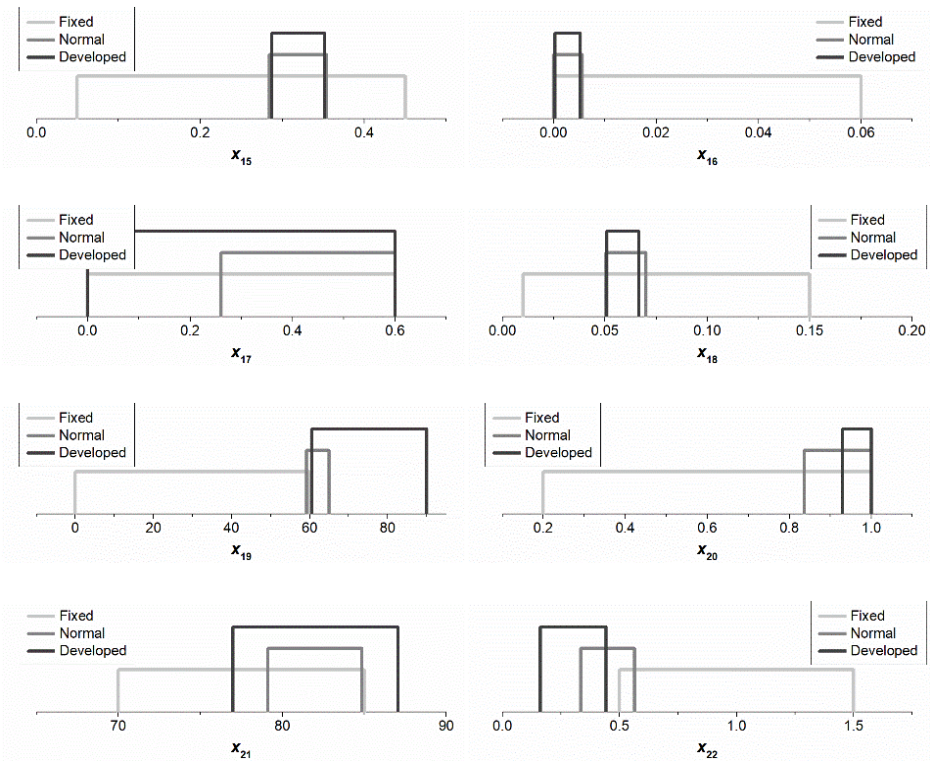

Fig. 4.24 Adapted design spaces for the conceptual design of an unmanned spacecraft

Near the extreme solutions, the positions of samples seem perpendicular to axis because the values for an objective are similar against the different values for the other objective function. To figure out this reason, the constraint values of the samples are depicted in Fig. 4.25. The static margin (SM) of the light weight samples are almost zero. The SMs of the spacecraft should be greater than zero to maintain the longitudinal stability. On the other hand, the landing speed of the low heat flux samples are almost 20 m/s. The landing speeds of the spacecraft should be lower than 20 m/s due to the constraint. In these reasons, the samples near the extreme solutions have similar values with the value of the extreme solutions.

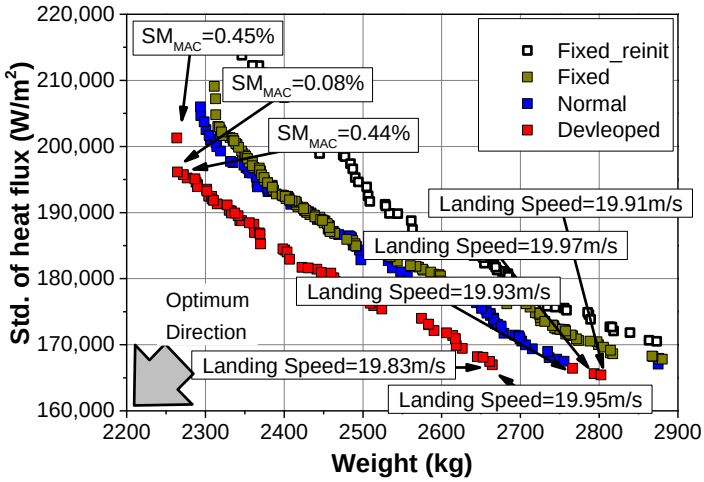

Fig. 4.25 The values of constraints near extreme solutions

The design space adaptation method improved both objective functions more effectively than the other methods, as shown in Fig. 4.26 which displays the trends of the objective functions for the extreme solutions. To evaluate the efficiency of the MOGA and design-space adaptation method, the number of function evaluations (NFE) was computed. The NFE was determined as the sum of the number of individuals (N_{ind}) from 1 to the number of generations (N_{gen}), as follows:

$$\mathrm{NFE} = \sum_{i=1}^{N_{\mathrm{gen}}} N_{\mathrm{ind}} \tag{4.77}$$

Since N_{ind} was fixed in this study, N_{gen} could be used as the efficiency metric. In Fig. 4.26, the developed method showed a more improved performance than the other methods. The developed method required fewer generations to achieve the same values of the objective functions, indicating higher efficiency than other method.

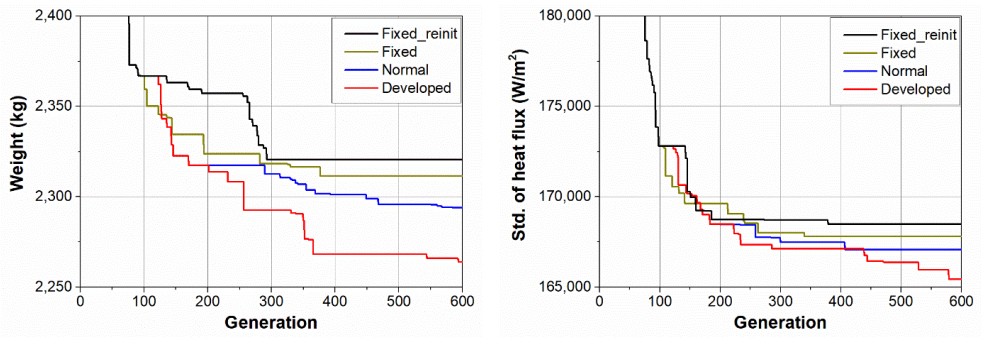

(a) weight (b) Std. of heat flux

Fig. 4.26 The evolution trends of the objective functions as the number of generations increased

Additionally, the purity metric achieved by the developed method is considerably greater than that of the method assuming normal distributions, as demonstrated in Fig. 4.27. These findings indicate that the Pareto solution obtained by the developed method outperforms that of the method assuming normal distributions. Therefore, the performance and efficiency of the MOGA were enhanced by the developed method.

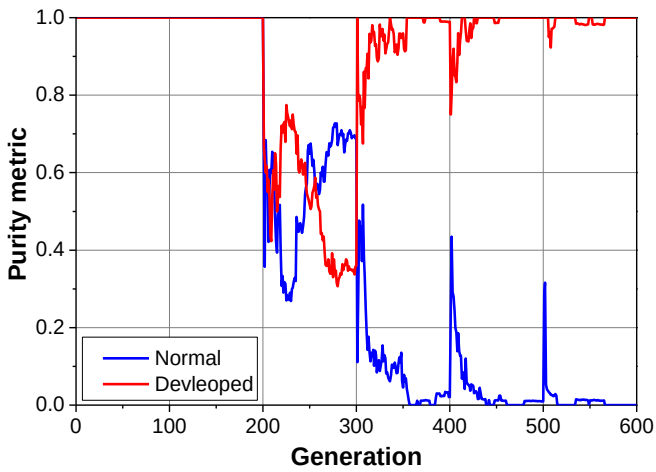

Fig. 4.27 The evolution trends of the purity metric as the number of generations increased

The extreme solutions obtained from the developed method were labeled as "OPT1-dev" and "OPT2-dev" and are depicted in Fig. 4.23. The compromise solution was selected by considering the balance between weight and the SD of heat flux performance and labeled "OPT_{com}." On the other hand, the Pareto solutions obtained with the method assuming normal distributions and the fixed design space were labeled as "OPT1-nor" and "OPT1-fix" or "OPT2-nor" and "OPT2-fix," depending on whether they had similar weights or SDs of heat flux to OPT_{com}.

The objective function values of the named solutions can be found in Table 4.8. The values of the featured design variables and geometries of the labeled solutions are presented in Table 4.9 and Fig. 4.28, respectively.

Table 4.8 Objective functions of the designed unmanned spacecraft

	Weight (kg)	SD of heat flux (W/m^2)
OPT1-dev	2,263.5	198,124
OPT2-dev	2,802.3	165,425
OPT_{com}	2,481.9	178,675
OPT1-nor	2,482.0	186,468
OPT2-nor	2,584.0	178,740
OPT1-fix	2,480.0	185,950
OPT2-fix	2,614.1	178,734

Table 4.9 Values of the feature design variables of the OPTs

	OPT1-dev	OPT2-dev	OPT_{com}	OPT1-nor	OPT1-fix	OPT2-nor	OPT2-fix
Nose radius	0.0944	0.2346	0.1234	0.1163	0.1118	0.1214	0.1153
Total length	8.2179	9.9734	9.2936	9.0153	8.7940	9.3764	9.3341
Wing root chord	4.8416	5.5657	5.1732	5.1683	5.2137	5.3900	5.4722
Wing span	4.1321	4.4850	4.2419	4.2720	4.2544	4.3608	4.3746
Wing area	11.245	14.247	12.572	12.666	12.769	13.527	13.788
Wing leading edge radius	0.0545	0.0648	0.0617	0.0611	0.0636	0.0652	0.0647

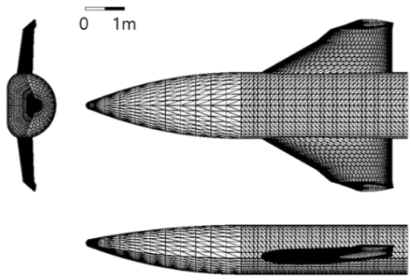

(a) OPT1-dev

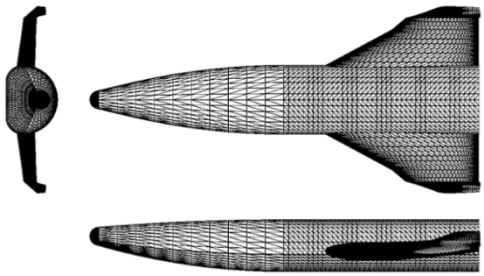

(b) OPT2-dev

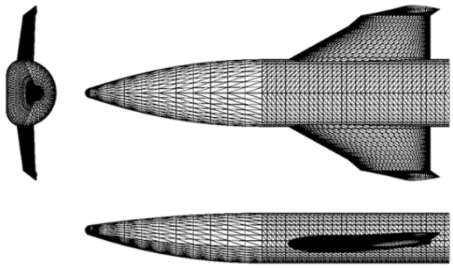

(c) OPT_{com}

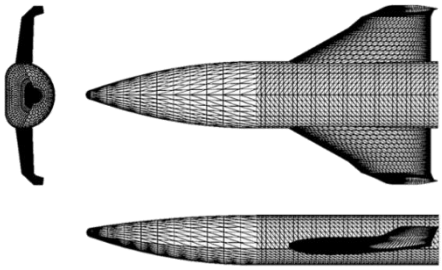

(d) OPT1-nor

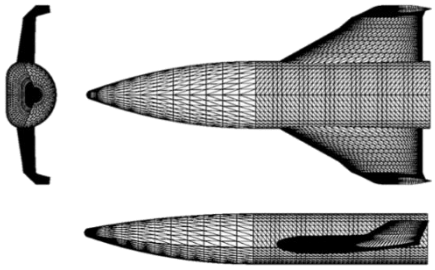

(e) OPT1-fix

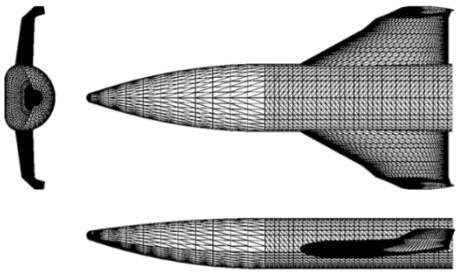

(f) OPT2-nor

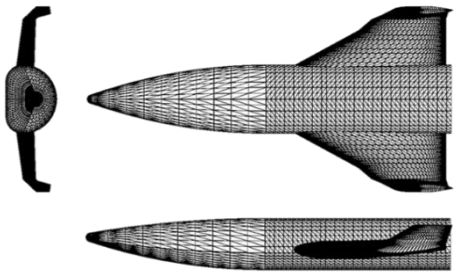

(g) OPT2-fix

Fig. 4.28 Geometries of the OPTs

OPT1-dev has shorter fuselage and smaller wing area than OPT2-dev. This is why the weight of OPT1-dev is lighter than OPT2-dev. On the other hand, OPT2-dev has larger nose radius and wing leading edge radius. With these large radius, OPT2-dev shows small heat flux because a large radius generates low heat flux in hypersonic vehicles.

The SD of the heat flux of OPT_{com} was lower than those of OPT1-nor and OPT1-fix by 4.2% and 3.9%, respectively, despite having similar weights. OPT_{com} had a larger nose radius and total length than OPT1-nor and OPT1-fix. The large nose radius reduced heat flux at the nose stagnation point during hypersonic flight. The large total length created a wide area on the lower surface of the fuselage, which is a pressure surface generating high lift force that increases acceleration in the inverse-gravity direction. As a result, when the maximum heat flux on the stagnation point occurred, the velocity and altitude were relatively low and high, respectively, as shown in Table 4.10. Consequently, it appears that the heat flux on the spacecraft with a large total length was low. Therefore, OPT_{com} achieved a lower heat flux than OPT1-nor and OPT1-fix, resulting in higher survival probability during the mission because a large amount of heat flux can destroy the spacecraft structure. Thus, while all three solutions had similar weights, the survival probability of OPT_{com} was higher than that of OPT1-nor and OPT1-fix.

Table 4.10 Flow conditions, inverse-gravity-direction accelerations induced by aerodynamic force, and heat fluxes at the stagnation point

	Altitude (km)	Velocity (m/s)	Acc. (m/s^2)	Heat flux at stagnation point (W/m^2)
OPT_{com}	58.50	6,751	35.61	2,860,800
OPT1-nor	58.43	6,754	35.53	2,962,300
OPT1-fix	58.33	6,760	35.43	3,047,800

The weight of OPT_{com} was 3.9% and 5.1% lower than those of OPT2-nor and OPT2-fix, respectively, while the SDs of the heat fluxes were comparable. OPT_{com} had smaller total length and root chord compared to OPT2-nor and OPT2-fix. As the fuselage weight was related to the volume and wetted area of the fuselage, a smaller total length decreased the fuselage weight. Similarly, the weight of the wing can be reduced by having a smaller wing area. Consequently, OPT_{com} was lighter than OPT2-nor and OPT2-fix. The weight difference between OPT_{com} and OPT2-nor was nearly 100 kg. Considering that the loading cost of a launch vehicle is more than $5,000 per kilogram [91], this weight difference would save over $500,000 of the budget required to load the spacecraft on a launch vehicle. Thus, the developed method yielded significantly better performance compared to the method assuming normal distributions.

4.4 Data mining

4.4.1 Analysis of variance (ANOVA)

ANOVA is a statistical analysis technique that is widely used to quantify the impact of an input variable (design variable) on an output variable (objective function). It uses the ratio of the variance due to each input variable to the total variance to quantify this influence. ANOVA breaks down the total variance into the variance associated with each design variable [92]. This decomposition is achieved by integrating the output variables of $\hat{y}$.

To determine the total mean ($\hat{\mu}_{\text{total}}$) and variance ($\hat{\sigma}^2_{\text{total}}$) of output variables, as follow:

$$\hat{\mu}_{\text{total}} \equiv \int \cdots \int \hat{y}(x_1, \cdots \cdots, x_L) \ \mathrm{d}x_1 \cdots \mathrm{d}x_L \tag{4.78}$$

$$\hat{\sigma}^2_{\text{total}} \equiv \int \cdots \int [\hat{y}(x_1, \cdots \cdots, x_L) - \hat{\mu}_{\text{total}}]^2 \ \mathrm{d}x_1 \cdots \mathrm{d}x_L \tag{4.79}$$

In this context, L refers to the number of design variables. The primary impact of the x_i variable can be expressed as follows:

$$\hat{\mu}_i(x_i) \equiv \int \cdots \int \hat{y}(x_1, \cdots \cdots, x_L) \ dx_1 \cdots dx_{i-1} dx_{i+1} \cdots dx_L - \hat{\mu}_{\text{total}} \tag{4.80}$$

The value of $\hat{\mu}_i(x_i)$ represents the degree of impact of the design variable x_i on the objective function. On the other hand, the variance related to the design variable x_i can be calculated as follows:

$$\hat{\sigma}_i^2 \equiv \int [\hat{\mu}_i(x_i)]^2 \ \mathrm{d}x_i \tag{4.81}$$

The ratio of the variance attributed to the design variable x_i to the entire variance of $\hat{y}$ can be computed by dividing Eq. (4.81) by Eq. (4.79):

$$\frac{\hat{\sigma}_i^2}{\hat{\sigma}_{\text{total}}^2} \equiv \frac{\int [\hat{\mu}_i(x_i)]^2 \ \mathrm{d}x_i}{\int \cdots \int [\hat{y}(x_1, \cdots\cdots, x_L) - \hat{\mu}_{\text{total}}]^2 \ \mathrm{d}x_1 \cdots \mathrm{d}x_L} \tag{4.82}$$

This numerical result indicates the impact of the design variable x_i on the objective function.

In Fig. 4.29 (a), the results obtained from ANOVA for the weight of the spacecraft are depicted, and the design variables that have a significant impact are presented, namely: total length, nose radius, and root chord. Typically, the weights of the fuselage and wing are connected to the volume and wetted area of the fuselage or the planform area of the wing. The total length represents the length of the fuselage, and the nose radius affects the volume and wetted area of the nose section, while the root chord is a crucial factor in determining the planform area. Hence, it can be concluded that the nose radius, total length, and root chord are highly influential in determining the weight of the spacecraft.

In Fig. 4.29 (b), the results obtained using ANOVA for the SD of heat flux on the spacecraft are illustrated, and the design variables with a substantial influence are shown, which are total length, nose radius, and root chord. The total length and root chord are vital parameters for determining the planform area and the lower surface area of the fuselage, respectively. The heat flux is well-known to be related to the flight velocity and air density, which are affected by the spacecraft's lift. The lift of the spacecraft is influenced by the area of the pressure surface, such as the wing and the lower surface of the fuselage. In addition, the nose radius corresponds to the knowledge of hypersonic flow, where the heat flux on the stagnation point is related to the nose radius. Thus, the nose radius, total length, and root chord are significant variables for the heat flux on the spacecraft.

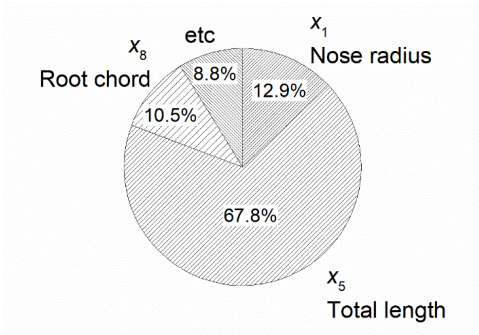

(a) Weight

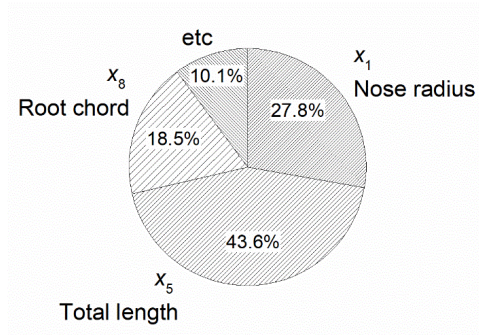

(b) SD of heat flux

Fig. 4.29 The result of ANOVA

4.4.2 Parallel chart

The parallel chart is a technique used to examine high-dimensional datasets visually [61]. It includes several parallel axes, and each axis corresponds to a variable of the samples. In this study, the Pareto solutions obtained from optimization were compared against the samples, while the design variables and objective functions were compared against the variables. The position of each sample on the axis is represented by a vertex, and the vertices are connected by polylines. The value of each variable of the sample corresponds to the position of the vertex on each axis. By coloring the lines according to one objective function value, the distribution of the lines for the design variables can be examined to analyze the qualitative relationships between the objective functions and the design variables.

In Fig. 4.30, the parallel chart is presented with the weight as the color scale. The first two columns indicate that Pareto solutions with low weight (blue line) have a high SD of heat flux, while those with high weight (red line) have a low SD of heat flux, indicating a trade-off relationship between weight and SD of heat flux. Low-weight solutions are associated with smaller spacecraft sizes, consistent with the general understanding that smaller spacecraft are relatively lighter. Notably, these low-weight solutions have small nose radius, total length, and root chord values. In contrast, solutions with a low SD of heat flux (red line) have higher nose radius, total length, and root chord values. By analyzing the distribution of the lines for the design variables, qualitative relationships between the objective functions and the design variables can be established.

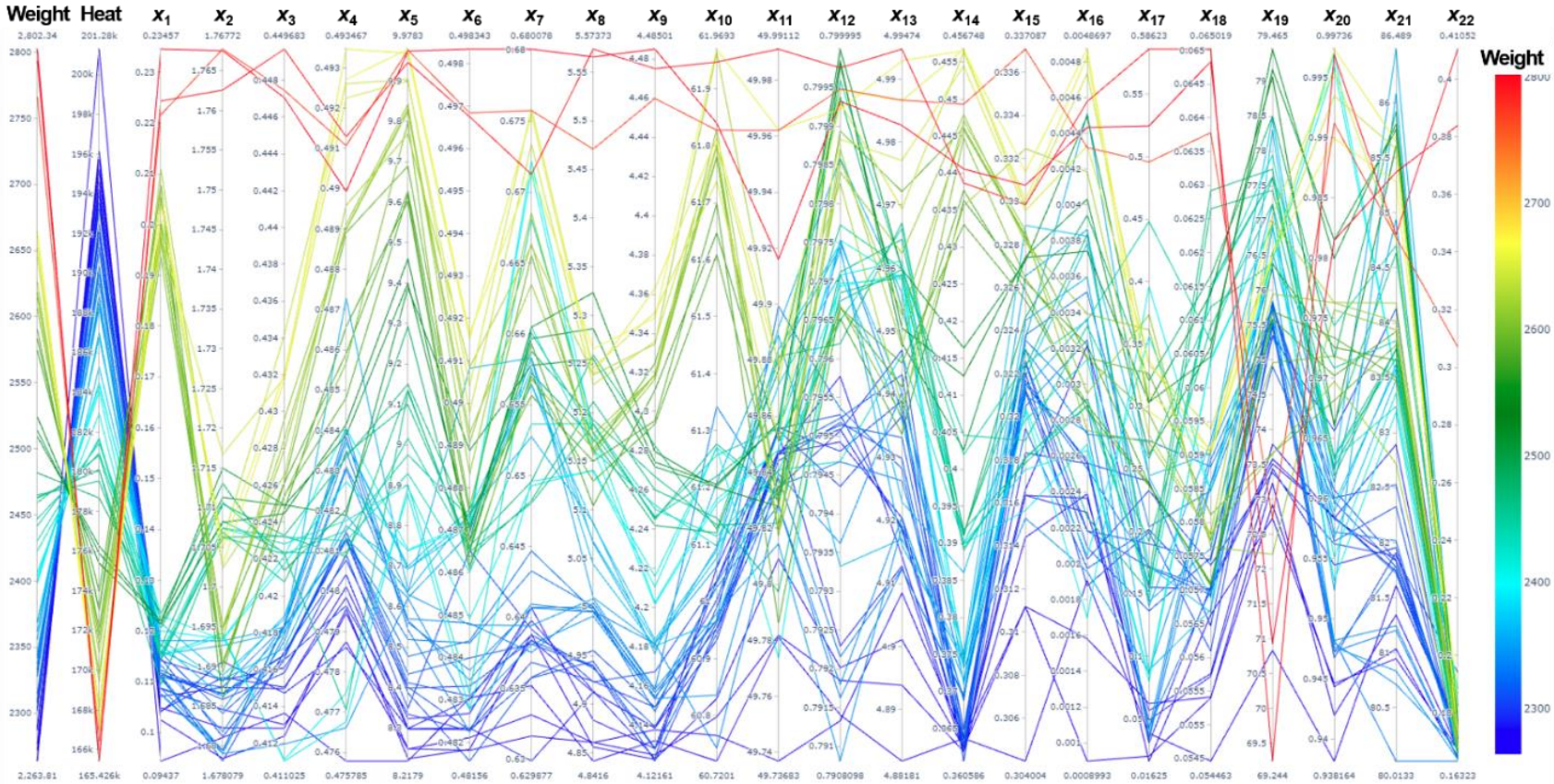

Fig. 4.30 Parallel charts with the results

4.4.3 Self-organizing map (SOM)

The Self-Organizing Map (SOM) is an unsupervised neural network approach that maps high-dimensional data onto a lower-dimensional space. The resulting map is composed of numerous nodes which are clustered based on the similarity of data or solutions. Each node on the map represents a solution, which allows for a qualitative analysis of the relationship between input and output variables or between different input variables by coloring the map according to the value of each variable. More information about the learning algorithm of SOM can be found in references [93,94].

To analyze the relationships between the objective functions and design variables, the color patterns of maps can be compared. In Fig. 4.31, a trade-off relation appears to exist between the weight and the SD of heat flux, as evidenced by the low-weight solutions (blue) in the right-top corner of the map having high heat flux (red), and the high-weight solutions (red) in the left-bottom corner of the map having low heat flux (blue). Similarly, the qualitative relationship between the objective functions and design variables can be analyzed. Nose radius, total length, and root chord are the design variables related to the objective functions, as the color patterns of the maps for these variables are similar or inversely similar to the color patterns of the objective functions. Based on the SOM analysis, it was found that the variables have a positive correlation with the weight, while they have a negative correlation with the heat flux, which is consistent with the findings of the parallel chart.

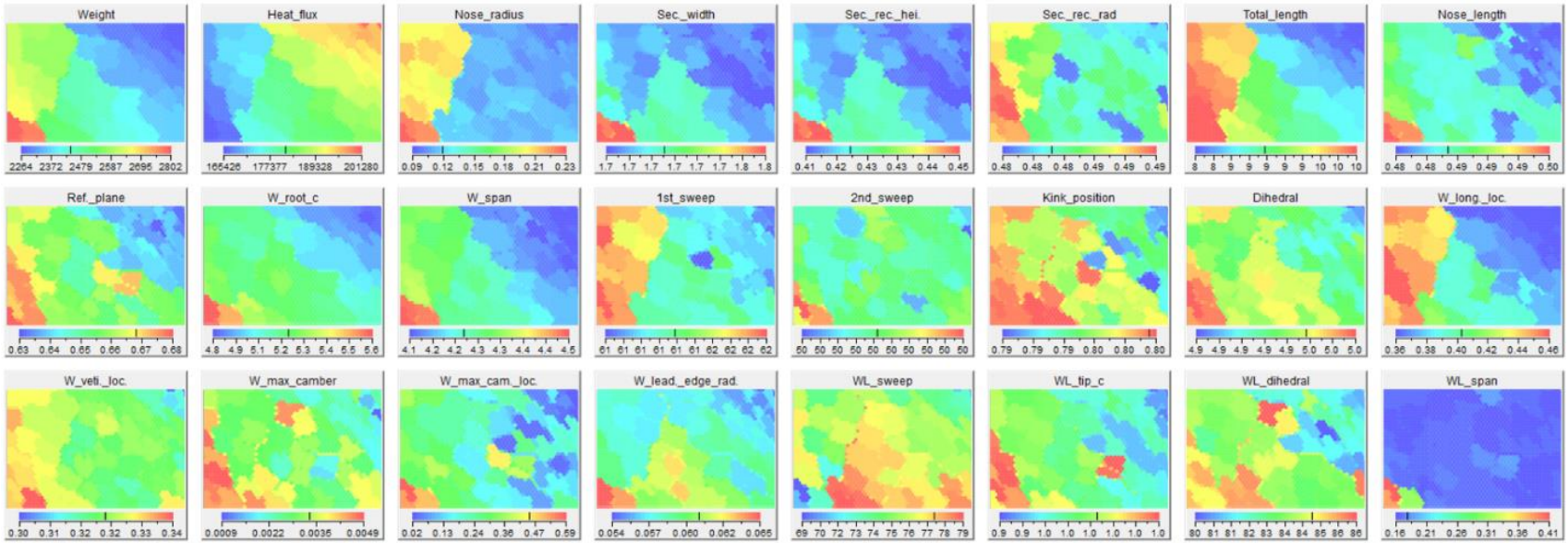

Fig. 4.31 SOM results

4.4.4 Summary of geometric features

Based on the results of ANOVA, parallel chart, and SOM, the critical characteristics of the spacecraft geometry that lead to enhanced performance can be summarized as:

1) The optimal spacecraft design should have a small nose radius, total length, and root chord, leading to a lower weight. By decreasing the nose radius, the weight of the nose section is reduced, while a shorter total length and smaller root chord contribute to a lighter fuselage and wing, respectively.
2) The spacecraft exhibiting a low standard deviation of heat flux possess a larger nose radius, total length, and root chord. This finding aligns with the knowledge of hypersonic flow, which suggests that a large nose radius decreases the heat flux at the stagnation point. In addition, a large total length and root chord result in a broad lower surface of the fuselage and wing, which is a pressure surface. The latter generates a high lift force that increases the acceleration in the direction opposite to gravity. Consequently, the spacecraft with a greater pressure surface exhibits relatively slower velocity and higher altitude compared to the spacecraft with a smaller pressure surface at the same altitude. Hence, the spacecraft having a larger total length displays lower heat flux than those with smaller total lengths.

Chapter 5

Conclusion

This study developed efficient methods that can be applied to multidisciplinary optimization to design reusable unmanned spacecraft, which has become increasingly in demand in these days. The methods involved the adaptive time-step method for an analysis in MDO based on the current state. To achieve this, a dynamic factor was introduced to adjust the time step between each heat flux evaluation. The dynamic factor was determined based on the current state. To validate this method, this method was applied to reduce the number of heat-flux evaluations required along a flight trajectory of spacecraft. For heat-flux calculation, the dynamic factor was varied based on the difference between the heat flux at an instant and the maximum heat flux over the entire trajectory. By shortening the time step when the heat flux was high, detailed information on heat flux was obtained, while increasing the time step under low-heat-flux conditions improved the efficiency of the heat-flux calculations. The dynamic factor was used to adaptively determine the time step, which improved efficiency with accuracy, making it an effective method for enhancing the efficiency of MDA. As a result, the number of heat-flux calculations decreased approximately one-tenth in with over 90% accuracy.

Further, this study introduced a new method that adaptively adjusted the design space by considering the actual distribution of solutions, as opposed to the conventional method that assumes the solution distribution to be normal distributions. The actual solution distribution was estimated by calculating the proportion of

solutions in each subspace, which divided the design space evenly. Moreover, the developed method preserved the area of the design space where the extreme solutions, being the best solutions for each objective function, existed.

In order to evaluate the effectiveness and efficiency of the developed adaptive design-space method, it was applied to nineteen widely used multiobjective test functions, namely the ZDT problems, I problems, and WFG problems. The results showed that the design space adapted by the developed adaptive design-space method was much closer to the analytical solution range compared to the conventional method that assumed normal distributions. The study found that the adaptive design-space method was able to adjust the design space appropriately to raise the probability of solution existence, leading to improved efficiency and performance of MOGA compared to the method that assumed normal distributions.

To validate the effectiveness of the developed methods for adjusting time step for heat-flux calculation and adjusting design space, this study utilized the developed efficient methods for heat-flux calculation and adaptive design space to perform MDO for reusable unmanned spacecraft. The MDO was established with weight, propulsion, aerothermodynamics, and trajectory analyses to address diverse spacecraft analysis technologies. The weight of the spacecraft was predicted using the modified HASA, while the required thrust and weight of engines were estimated based on the entry weight. Aerodynamic properties were calculated using the modified Newtonian theory and Digital DATCOM, and the approximate convective-heating equations were used for heat-flux calculation. The spacecraft trajectory was modeled using three design-of-freedom equations of motion. To facilitate multi-disciplinary optimization, the these analyses was integrated with a multi-objective

genetic algorithm.

The optimization for the reusable unmanned spacecraft was performed by the established MDO with the developed method of adaptive time step for heat-flux calculations and adaptive design space. According to the results obtained by optimization, it was found that the Pareto solutions generated by the developed adaptive design-space method outperformed those obtained from the conventional methods. Therefore, it can be inferred that the developed adaptive design-space method could be beneficially implemented in solving complex real-world optimization problems, offering better efficiency and performance.

Furthermore, this research conducted data mining to comprehend why the optimized shapes demonstrate better performance by identifying the geometric features that affect the performance of unmanned spacecraft. The analysis of variance (ANOVA), parallel chart, and self-organizing map (SOM) methods were utilized as data mining techniques. All three techniques produced consistent results. The outcomes revealed the weight and heat flux trade-off relationship. The nose radius, total length, and root chord were identified as significant variables for spacecraft performance. A smaller geometry size reduced the weight, whereas a larger total length, nose radius, and root chord decreased the heat flux by operating at low velocity at high altitudes, where air density is low, and by generating high lift due to a large total length and root chord. In hypersonic flight, a large nose radius resulted in a low heat flux at the nose stagnation point, corresponding to hypersonic flow knowledge.

Appendix

This appendix presents information on the initial design space and the constraints on the problem that was studied in this study.

Conceptual design of the unmanned spacecraft

Initial space $0.05 \leq x_1 \leq 0.34$

$1.53 \leq x_2 \leq 1.82$

$0.35 \leq x_3 \leq 0.55$

$0.34 \leq x_4 \leq 0.5$

$8.08 \leq x_5 \leq 10$

$0.45 \leq x_6 \leq 0.5$

$0.56 \leq x_7 \leq 0.71$

$4.15 \leq x_8 \leq 5.92$

$4.20 \leq x_9 \leq 5$

$47.7 \leq x_{10} \leq 65.6$

$48 \leq x_{11} \leq 50$

$0.49 \leq x_{12} \leq 0.8$

$2.99 \leq x_{13} \leq 5$

$0.37 \leq x_{14} \leq 0.4$

$0.11 \leq x_{15} \leq 0.45$

$0 \leq x_{16} \leq 0.009$

$0.29 \leq x_{17} \leq 0.6$

$0.016 \leq x_{18} \leq 0.078$

$52.7 \leq x_{19} \leq 60.3$

$0.43 \leq x_{20} \leq 1$

$70.1 \leq x_{21} \leq 85.6$

$0.48 \leq x_{22} \leq 0.98$

Side constraint $0.05 \leq x_1 \leq 0.34$

$1.53 \leq x_2$

$0.35 \leq x_3$

$x_4 \leq 0.5$

$x_5 \leq 10$

$x_6 \leq 0.5$

$x_9 \leq 5$

$x_{11} \leq 50$

$x_{12} \leq 0.8$

$2.99 \leq x_{13} \leq 5$

$0 \leq x_{16} \leq 0.009$

$0.29 \leq x_{17} \leq 0.6$

$0.016 \leq x_{18}$

$52.7 \leq x_{19}$

$x_{20} \leq 1$

$70.1 \leq x_{21}$

References

[1] Euroconsult. *Space Economy Report*. 2021.

[2] Euroconsult. *Space Economy Report*. 2022.

[3] Morgan Stanley. Space: Investing in the Final Frontier. https://www.morganstanley.com/ideas/investing-in-space.

[4] Harloff, G. J., and Berkowitz, B. M. *HASA-Hypersonic Aerospace Sizing Analysis for the Preliminary Design of Aerospace Vehicles*. Cleveland, Ohio, USA, 1988.

[5] Rohrschneider, R. R. "Development of a Mass Estimating Relationship Database for Launch Vehicle Conceptual Design." *Technology*, 2002.

[6] Zoby, E. V., Moss, J. N., and Suttont, K. "Approximate Convective-Heating Equations for Hypersonic Flows." *Journal of Spacecraft and Rockets*, Vol. 18, No. 1, 1981, pp. 64–70. https://doi.org/10.2514/3.57788.

[7] Zhao, J., Gu, L., and Ma, H. "A Rapid Approach to Convective Aeroheating Prediction of Hypersonic Vehicles." *Science China Technological Sciences*, Vol. 56, No. 8, 2013, pp. 2010–2024. https://doi.org/10.1007/s11431-013-5258-6.

[8] Jung, J., Yang, H., Kim, K., Yee, K., You, K., Park, K., and Jeong, S. "Conceptual Design of a Reusable Unmanned Space Vehicle Using Multidisciplinary Optimization." *International Journal of Aeronautical and Space Sciences*, Vol. 19, No. 3, 2018, pp. 743–750. https://doi.org/10.1007/s42405-018-0079-2.

[9] Wu, Z., and Liu, Y. “Integrated Optimization Design Using Improved Pigeon-Inspired Algorithm for a Hypersonic Vehicle Model.” *International Journal of Aeronautical and Space Sciences*, 2022. https://doi.org/10.1007/s42405-022-00492-1.

[10] Lee, D.-S., and Sung, H.-G. “Performance Design of a Turbofan Engine Using Multi-Objective Particle Swarm Optimization (MOPSO).” *International Journal of Aeronautical and Space Sciences*, Vol. 23, No. 3, 2022, pp. 533–545. https://doi.org/10.1007/s42405-022-00451-w.

[11] Arshad, A., Rodrigues, L. B., and López, I. M. “Design Optimization and Investigation of Aerodynamic Characteristics of Low Reynolds Number Airfoils.” *International Journal of Aeronautical and Space Sciences*, Vol. 22, No. 4, 2021, pp. 751–764. https://doi.org/10.1007/s42405-021-00362-2.

[12] Birken, P., Quint, K. J., Hartmann, S., and Meister, A. “A Time-Adaptive Fluid-Structure Interaction Method for Thermal Coupling.” *Computing and Visualization in Science*, Vol. 13, No. 7, 2010, pp. 331–340. https://doi.org/10.1007/s00791-010-0150-4.

[13] Press, W. H., and Teukolsky, S. A. “Adaptive Stepsize Runge-Kutta Integration.” *Computers in Physics*, Vol. 6, No. 2, 1992, p. 188. https://doi.org/10.1063/1.4823060.

[14] Tremblay, J. C., and Carrington, T. “Using Preconditioned Adaptive Step Size Runge-Kutta Methods for Solving the Time-Dependent Schrödinger Equation.” *The Journal of Chemical Physics*, Vol. 121, No. 23, 2004, pp. 11535–11541. https://doi.org/10.1063/1.1814103.

[15] Gustafsson, K. “Control Theoretic Techniques for Stepsize Selection in

Explicit Runge-Kutta Methods." *ACM Transactions on Mathematical Software*, Vol. 17, No. 4, 1991, pp. 533–554. https://doi.org/10.1145/210232.210242.

[16] Gustafsson, K. "Control-Theoretic Techniques for Stepsize Selection in Implicit Runge-Kutta Methods." *ACM Transactions on Mathematical Software*, Vol. 20, No. 4, 1994, pp. 496–517. https://doi.org/10.1145/198429.198437.

[17] Gustafsson, K., Lundh, M., and Söderlind, G. "A PI Stepsize Control for the Numerical Solution of Ordinary Differential Equations." *BIT*, Vol. 28, No. 2, 1988, pp. 270–287. https://doi.org/10.1007/BF01934091.

[18] Kushner, H. J., and Yang, J. "Analysis of Adaptive Step-Size SA Algorithms for Parameter Tracking." *IEEE Transactions on Automatic Control*, Vol. 40, No. 8, 1995, pp. 1403–1410. https://doi.org/10.1109/9.402231.

[19] Söderlind, G. "Automatic Control and Adaptive Time-Stepping." *Numerical Algorithms*, Vol. 31, Nos. 1–4, 2002, pp. 281–310. https://doi.org/10.1023/A:1021160023092.

[20] Walter, D., Petrov, V., Manera, A., and Kendrick, B. K. A Control Theory Approach to Adaptive Stepsize Selection for Coupled CFD and Crud Chemistry Simulations. No. 2, 2015, pp. 926–939.

[21] Valli, A. M. P., Carey, G. F., and Coutinho, A. L. G. A. "Control Strategies for Timestep Selection in Finite Element Simulation of Incompressible Flows and Coupled Reaction-Convection-Diffusion Processes." *International Journal for Numerical Methods in Fluids*, Vol. 47, No. 3,

2005, pp. 201–231. https://doi.org/10.1002/fld.805.

[22] Valli, A. M. P., Carey, G. F., and Coutinho, A. L. G. A. "Control Strategies for Timestep Selection in Simulation of Coupled Viscous Flow and Heat Transfer." *Communications in Numerical Methods in Engineering*, Vol. 18, No. 2, 2002, pp. 131–139. https://doi.org/10.1002/cnm.475.

[23] Cueto-Felgueroso, L., and Peraire, J. "A Time-Adaptive Finite Volume Method for the Cahn–Hilliard and Kuramoto–Sivashinsky Equations." *Journal of Computational Physics*, Vol. 227, No. 24, 2008, pp. 9985–10017. https://doi.org/10.1016/j.jcp.2008.07.024.

[24] Chen, F., Liu, H., and Zhang, S. "Time-Adaptive Loosely Coupled Analysis on Fluid–Thermal–Structural Behaviors of Hypersonic Wing Structures under Sustained Aeroheating." *Aerospace Science and Technology*, Vol. 78, 2018, pp. 620–636. https://doi.org/10.1016/j.ast.2018.05.015.

[25] Zhang, S., Chen, F., and Liu, H. "Time-Adaptive, Loosely Coupled Strategy for Conjugate Heat Transfer Problems in Hypersonic Flows." *Journal of Thermophysics and Heat Transfer*, Vol. 28, No. 4, 2014, pp. 635–646. https://doi.org/10.2514/1.T4278.

[26] Chen, F., Liu, H., and Zhang, S. "Coupled Heat Transfer and Thermo-Mechanical Behavior of Hypersonic Cylindrical Leading Edges." *International Journal of Heat and Mass Transfer*, Vol. 122, 2018, pp. 846–862. https://doi.org/10.1016/j.ijheatmasstransfer.2018.02.037.

[27] Somarathne, S., Seymour, M., and Kolokotroni, M. "Dynamic Thermal CFD Simulation of a Typical Office by Efficient Transient Solution Methods." *Building and Environment*, Vol. 40, No. 7, 2005, pp. 887–896.

https://doi.org/10.1016/j.buildenv.2004.09.016.

[28] Frenzel, J. F. “Genetic Algorithms.” *IEEE Potentials*, Vol. 12, No. 3, 1993, pp. 21–24. https://doi.org/10.1109/45.282292.

[29] Poli, R., Kennedy, J., and Blackwell, T. “Particle Swarm Optimization: An Overview.” *Swarm Intelligence*, Vol. 1, No. 1, 2007, pp. 33–57. https://doi.org/10.1007/s11721-007-0002-0.

[30] Jung, J., Yee, K., Misaka, T., and Jeong, S. “Low Reynolds Number Airfoil Design for a Mars Exploration Airplane Using a Transition Model.” *Transactions of the Japan Society for Aeronautical and Space Sciences*, Vol. 60, No. 6, 2017, pp. 333–340. https://doi.org/10.2322/tjsass.60.333.

[31] Hashimoto, A., Jeong, S., and Obayashi, S. “Aerodynamic Optimization of Near-Future High-Wing Aircraft.” *Transactions of the Japan Society for Aeronautical and Space Sciences*, Vol. 58, No. 2, 2015, pp. 73–82. https://doi.org/10.2322/tjsass.58.73.

[32] Singh, R. K., Ahmed, M. R., Zullah, M. A., and Lee, Y. H. “Design of a Low Reynolds Number Airfoil for Small Horizontal Axis Wind Turbines.” *Renewable Energy*, Vol. 42, 2012, pp. 66–76. https://doi.org/10.1016/j.renene.2011.09.014.

[33] Jeong, S., Sasaki, T., Chae, S., Yee, K., and Aoyama, T. “Design Exploration of Helicopter Blades for HSI Noise and Aerodynamic Performance.” *Transactions of the Japan Society for Aeronautical and Space Sciences*, Vol. 54, No. 184, 2011, pp. 153–159. https://doi.org/10.2322/tjsass.54.153.

[34] Jeong, S., Obayashi, S., and Minemura, Y. “Application of Hybrid

Evolutionary Algorithms to Low Exhaust Emission Diesel Engine Design." *Engineering Optimization*, Vol. 40, No. 1, 2008, pp. 1–16. https://doi.org/10.1080/03052150701561155.

[35] Jeong, S., and Kim, H. "Development of an Efficient Hull Form Design Exploration Framework." *Mathematical Problems in Engineering*, Vol. 2013, 2013. https://doi.org/10.1155/2013/838354.

[36] Yang, S., Lee, S., and Yee, K. "Inverse Design Optimization Framework via a Two-Step Deep Learning Approach: Application to a Wind Turbine Airfoil." *Engineering with Computers*, 2022. https://doi.org/10.1007/s00366-022-01617-6.

[37] Amirjanov, A. "A Changing Range Genetic Algorithm." *International Journal for Numerical Methods in Engineering*, Vol. 61, No. 15, 2004, pp. 2660–2674. https://doi.org/10.1002/nme.1175.

[38] Amirjanov, A. "The Development of a Changing Range Genetic Algorithm." *Computer Methods in Applied Mechanics and Engineering*, Vol. 195, Nos. 19–22, 2006, pp. 2495–2508. https://doi.org/10.1016/j.cma.2005.05.014.

[39] Amirjanov, A. "Investigation of a Changing Range Genetic Algorithm in Noisy Environments." *International Journal for Numerical Methods in Engineering*, Vol. 73, No. 1, 2008, pp. 26–46. https://doi.org/10.1002/nme.2053.

[40] Amirjanov, A., and Sadikoglu, F. "Linear Adjustment of a Search Space in Genetic Algorithm." *Procedia Computer Science*, Vol. 120, 2017, pp. 953–960. https://doi.org/10.1016/j.procs.2017.11.331.

[41] Amirjanov, A. “The Parameters Setting of a Changing Range Genetic Algorithm.” *Natural Computing*, Vol. 14, No. 2, 2015, pp. 331–338. https://doi.org/10.1007/s11047-014-9420-2.

[42] Amirjanov, A. “Modeling the Dynamics of a Changing Range Genetic Algorithm.” *Procedia Computer Science*, Vol. 102, No. August, 2016, pp. 570–577. https://doi.org/10.1016/j.procs.2016.09.444.

[43] Chen, Z., Cao, H., Ye, K., Zhu, H., and Li, S. “Improved Particle Swarm Optimization-Based Form-Finding Method for Suspension Bridge Installation Analysis.” *Journal of Computing in Civil Engineering*, Vol. 29, No. 3, 2015, p. 04014047. https://doi.org/10.1061/(ASCE)CP.1943-5487.0000354.

[44] Jeong, S., Obayashi, S., and Yamamoto, K. “A Kriging-Based Probabilistic Optimization Method with an Adaptive Search Region.” *Engineering Optimization*, Vol. 38, No. 5, 2006, pp. 541–555. https://doi.org/10.1080/03052150600627073.

[45] Kitayama, S., Yamazaki, K., and Arakawa, M. “Adaptive Range Particle Swarm Optimization.” *Optimization and Engineering*, Vol. 10, No. 4, 2009, pp. 575–597. https://doi.org/10.1007/s11081-009-9081-7.

[46] Arakawa, M., and Hagiwara, I. “Development of Adaptive Real Range (ARRange) Genetic Algorithms.” *JSME International Journal Series C*, Vol. 41, No. 4, 1998, pp. 969–977. https://doi.org/10.1299/jsmec.41.969.

[47] Arakawa, M., and Hagiwara, I. “Nonlinear Integer, Discrete and Continuous Optimization Using Adaptive Range Genetic Algorithms.” *Volume 2: 23rd Design Automation Conference*, 1997.

https://doi.org/10.1115/DETC97/DAC-3728.

[48] Oyama, A., Obayashi, S., and Nakahashi, K. “Real-Coded Adaptive Range Genetic Algorithm and Its Application to Aerodynamic Design.” *JSME International Journal Series A*, Vol. 43, No. 2, 2000, pp. 124–129. https://doi.org/10.1299/jsmea.43.124.

[49] Oyama, A., Obayashi, S., and Nakamura, T. “Real-Coded Adaptive Range Genetic Algorithm Applied to Transonic Wing Optimization.” *Applied Soft Computing*, Vol. 1, No. 3, 2001, pp. 179–187. https://doi.org/10.1016/S1568-4946(01)00017-5.

[50] Oyama, A., Obayashi, S., and Nakahashi, K. Wing Design Using Real-Coded Adaptive Range Genetic Algorithm. No. 4, 1999, pp. 475–480.

[51] Sasaki, D., and Obayashi, S. “Efficient Search for Trade-Offs by Adaptive Range Multi-Objective Genetic Algorithms.” *Journal of Aerospace Computing, Information, and Communication*, Vol. 2, No. 1, 2005, pp. 44–64. https://doi.org/10.2514/1.12909.

[52] Obayashi, S., and Sasaki, D. Multi-Objective Optimization for Aerodynamic Designs by Using ARMOGAs. 2004.

[53] Skinner, S. N., and Zare-Behtash, H. “State-of-the-Art in Aerodynamic Shape Optimisation Methods.” *Applied Soft Computing*, Vol. 62, 2018, pp. 933–962. https://doi.org/10.1016/j.asoc.2017.09.030.

[54] Jung, S., Choi, W., Martins-Filho, L. S., and Madeira, F. “An Implementation of Self-Organizing Maps for Airfoil Design Exploration via Multi-Objective Optimization Technique.” *Journal of Aerospace Technology and Management*, Vol. 8, No. 2, 2016, pp. 193–202.

https://doi.org/10.5028/jatm.v8i2.585.

[55] Chiba, K., Yoda, H., Ito, S., and Kanazaki, M. Visualization of Design-Space Constitution for Single-Stage Hybrid Rocket with Rigid Body in View of Extinction-Reignition. 2015.

[56] Pohl, J., Thompson, H. M., Schlaps, R. C., Shahpar, S., Fico, V., and Clayton, G. A. "Innovative Turbine Stator Well Design Using a Kriging-Assisted Optimization Method." *Journal of Engineering for Gas Turbines and Power*, Vol. 139, No. 7, 2017, pp. 1–9. https://doi.org/10.1115/1.4035288.

[57] Choi, W., and Park, H. "Optimized Design and Analysis of Composite Flexible Wing Using Aero-Nonlinear Structure Interaction." *Composite Structures*, Vol. 225, No. January, 2019, p. 111027. https://doi.org/10.1016/j.compstruct.2019.111027.

[58] Horii, H. "Multi-Objective Optimization of Vehicle Occupant Restraint System by Using Evolutionary Algorithm with Response Surface Model." *International Journal of Computational Methods and Experimental Measurements*, Vol. 5, No. 2, 2017, pp. 163–170. https://doi.org/10.2495/CMEM-V5-N2-163-170.

[59] Luchun, Y., Xuebin, L., Lei, Z., Chi, H., and Changjie, W. "Application of Multiobjective Optimization and Multivariate Analysis in Multiple Energy Systems: A Case Study of CGAM." *International Transactions on Electrical Energy Systems*, Vol. 30, No. 7, 2020, pp. 1–19. https://doi.org/10.1002/2050-7038.12368.

[60] Jones, D. R., Schonlau, M., and W. J. Welch. "Efficient Global

Optimization of Expensive Black-Box Functions," , Vol. 13, No. 4, Pp. 455-492, 1998." *Journal of Global Optimization*, Vol. 13, 1998, pp. 455–492.

[61] Inselberg, A. "The Plane with Parallel Coordinates." *The Visual Computer*, Vol. 1, No. 2, 1985, pp. 69–91. https://doi.org/10.1007/BF01898350.

[62] Kohonen, T. *Self-Organizing Maps*. Springer Berlin Heidelberg, Berlin, Heidelberg, 1997.

[63] Zitzler, E., Deb, K., and Thiele, L. "Comparison of Multiobjective Evolutionary Algorithms: Empirical Results." *Evolutionary computation*, Vol. 8, No. 2, 2000, pp. 173–195. https://doi.org/10.1162/106365600568202.

[64] Deb, K. *Multi-Objective Optimization Using Evlotionary Algorithms*. West Sussex, England, 2001.

[65] Bandyopadhyay, S., Pal, S. K., and Aruna, B. "Multiobjective GAs, Quantitative Indices, and Pattern Classification." *IEEE Transactions on Systems, Man and Cybernetics, Part B (Cybernetics)*, Vol. 34, No. 5, 2004, pp. 2088–2099. https://doi.org/10.1109/TSMCB.2004.834438.

[66] Huband, S., Barone, L., While, L., and Hingston, P. A Scalable Multi-Objective Test Problem Toolkit. 2005.

[67] Custódio, A. L., Madeira, J. F. A., Vaz, A. I. F., and Vicente, L. N. "Direct Multisearch for Multiobjective Optimization." *SIAM Journal on Optimization*, Vol. 21, No. 3, 2011, pp. 1109–1140. https://doi.org/10.1137/10079731X.

[68] Huband, S., Hingston, P., Barone, L., and While, L. "A Review of Multiobjective Test Problems and a Scalable Test Problem Toolkit." *IEEE*

Transactions on Evolutionary Computation, Vol. 10, No. 5, 2006, pp. 477–506. https://doi.org/10.1109/TEVC.2005.861417.

[69] Mccroskey, W. J. "A Critical Assessment of Wind Tunnel Results for the NACA 0012 Airfoil." *NASA technical Memorandum 100019 USAAVSCOM Technical Report 87-A-5*, 1987.

[70] Yokoyama, N., Suzuki, S., Tsuchiya, T., Taguchi, H., and Kanda, T. "Multidisciplinary Design Optimization of Space Plane Considering Rigid Body Characteristics." *Journal of Spacecraft and Rockets*, Vol. 44, No. 1, 2007, pp. 121–131. https://doi.org/10.2514/1.19969.

[71] June Malone. *X-37 Demonstrator to Test Future Launch Technologies in Orbit and Reentry Environments*. NASA FS-2003-05-65-MSFC, 2003.

[72] Anderson Jr, J. *Modern Compressible Flow with Historical Perspective*. McGraw-Hill, NewYork, NY, USA, 2004.

[73] Williams, J. E., Murray, S. C., Mehlick, G. J., and Sellers, T. B. *The USAF Stability and Control Digital Datcom Volume 1: Users Manual*. St. Louis, Missouri, USA, 1979.

[74] Gamble, J. D., Cooke, D. R., Underwood, J. M., Stone, H. W., and Schlosser, D. C. Development and Application of Aerodynamic Uncertainties; and Flight Test Verification for the Space Shuttle Orbiter. 1985.

[75] Hamilton, H. H., Weilmuenster, K. J., and Dejarnette, F. R. "Improved Approximate Method for Computing Convective Heating on Hypersonic Vehicles Using Unstructured Grids." *Collection of Technical Papers - 9th AIAA/ASME Joint Thermophysics and Heat Transfer Conference*

Proceedings, Vol. 2, No. June, 2006, pp. 1306–1326. https://doi.org/10.2514/6.2006-3394.

[76] Hamilton, H. H., Weilmuenster, K. J., and DeJarnette, F. R. "Approximate Method for Computing Laminar and Turbulent Convective Heating on Hypersonic Vehicles Using Unstructured Grids." *41st AIAA Thermophysics Conference*, 2009, pp. 1–26. https://doi.org/10.2514/6.2009-4310.

[77] Lo, S. H. "Automatic Mesh Generation over Intersecting Surfaces." *International Journal for Numerical Methods in Engineering*, Vol. 38, No. 6, 1995, pp. 943–954. https://doi.org/10.1002/nme.1620380605.

[78] Cooke, J. C. *An Axially Symmetric Analogue for General Three-Dimensional Boundary Layers*. 1961.

[79] Bertin, J. J., and Cummings, R. M. "Fifty Years of Hypersonics: Where We've Been, Where We're Going." *Progress in Aerospace Sciences*, Vol. 39, Nos. 6–7, 2003, pp. 511–536. https://doi.org/10.1016/S0376-0421(03)00079-4.

[80] Brchnelova, M., and Mooij, E. "Re-Entry Shape Optimisation Using the Axisymmetric Analogue Method with Modified Newtonian Technique Resolved Inviscid Flow Field." *AIAA Scitech 2021 Forum*, No. January, 2021, pp. 1–23. https://doi.org/10.2514/6.2021-0171.

[81] Bouslog, S., An, M., Hartmann, L., and Derry, S. Review of Boundary Layer Transition Flight Data on the Space ShuttleOrbiter. 1991.

[82] Ernst, E. "Survey on Heat Transfer at High Speed." *U.S Air Force*, Vol. ARL 189, 1961.

[83] Kemp, N. H., Rose, P. H., and Detra, R. W. "Laminar Heat Transfer around

Blunt Bodies in Dissociated Air." *Journal of the Aerospace Sciences*, Vol. 26, No. 7, 1959, pp. 421–430. https://doi.org/10.2514/8.8128.

[84] de Jarnette, F. R., Harris Hamilton, H., James Weilmuenster, K., and McNeil Cheatwood, F. "A Review of Some Approximate Methods Used in Aerodynamic Heating Analyses." *Journal of Thermophysics and Heat Transfer*, Vol. 1, No. 1, 1987, pp. 5–12. https://doi.org/10.2514/3.1.

[85] Hamilton, H. H., Millman, D. R., and Greendyke, R. B. "Finite-Difference Solution for Laminar or Turbulent Boundary Layer Flow over Axisymmetric Bodies with Ideal Gas, CF4, or Equilibrium Air Chemistry." *NASA Technical Paper 3271*, 1992.

[86] Liou, M.-S. "A Sequel to AUSM: AUSM+." *Journal of Computational Physics*, Vol. 129, No. 2, 1996, pp. 364–382. https://doi.org/10.1006/jcph.1996.0256.

[87] Rausch, R., Yang, H., and Batina, J. Spatial Adaption Procedures on Unstructured Meshes for Accurate Unsteady Aerodynamic Flow Computation. 1991.

[88] Etkin, B., and Reid, L. D. *Dynamics of Flight: Stability and Control*. Wiley, Danvers, 1995.

[89] Bate, R., Mueller, D., and White, J. *Fundamentals of Astrodynamics*. Dover Publications, New York, 1971.

[90] Sim, H., and Kim, K. "Reentry Survival Analysis of Tumbling Metallic Hollow Cylinder." *Advances in Space Research*, Vol. 48, No. 5, 2011, pp. 914–922. https://doi.org/10.1016/j.asr.2011.04.036.

[91] Mohney, D. The Coming U.S. Small Launch Crash, Thanks to SpaceX

Rideshare. *Spaceitbridge*. https://www.spaceitbridge.com/the-coming-u-s-small-launch-crash-thanks-to-spacex-rideshare.htm.

[92] Jeong, S., Chiba, K., and Obayashi, S. "Data Mining for Aerodynamic Design Space." *Journal of Aerospace Computing, Information, and Communication*, Vol. 2, No. 11, 2005, pp. 452–469. https://doi.org/10.2514/1.17308.

[93] Chiba, K., and Obayashi, S. "Data Mining for Multidisciplinary Design Space of Regional-Jet Wing." *Journal of Aerospace Computing, Information, and Communication*, Vol. 4, No. 11, 2007, pp. 1019–1036. https://doi.org/10.2514/1.19404.

[94] Oyama, A., Okabe, Y., Shimoyama, K., and Fujii, K. "Aerodynamic Multiobjective Design Exploration of a Flapping Airfoil Using a Navier-Stokes Solver." *Journal of Aerospace Computing, Information, and Communication*, Vol. 6, No. 3, 2009, pp. 256–270. https://doi.org/10.2514/1.35992.

국문 초록

증가하는 재사용 무인우주비행체에 대한 수요에 대응하기 위하여, 본 연구에서는 재사용 무인 우주비행체의 개념설계에 적용 가능한 효율적인 기법을 개발하였다. 우주비행체 개념설계를 위한 다양한 해석 중에서, 형상정의, 중량추정, 추진분석 등은 계산이 적은 횟수로 이루어지는 반면, 공력 및 열전달량, 궤도 계산은 궤도의 각 위치에서 계산이 수행되어야 하므로 수많은 계산이 필요하다. 그리므로 본 연구에서는 궤도에서의 현재 상태에 기반하여 각 분석에서 사용되는 시간 간격을 조절할 수 있는 기법을 개발하였다. 개발된 기법은 열전달량 해석에 적용하여 효용성을 검증하였다. 시간 간격을 조절하기 위하여 동적 요소를 도입하였으며, 이를 토대로 열전달량이 낮을 경우 시간 간격을 증가시켰다. 그 결과, 90% 이상의 정확도를 유지하면서 열전달량 계산 횟수가 약 1/10으로 감소하였다. 이와 같이 개발된 동적 요소에 따라 시간 간격을 조절할 경우, 높은 정확도를 유지하면서 열전달량 계산 효율을 증가시킬 수 있다.

이와 더불어, 기존 설계 공간 조절 기법은 변수 분포를 정규분포로 가정하였으나 실제 문제에서는 변수 분포가 정규분포를 따를 경우가 매우 드물다. 이와 같은 기존 설계 공간 조절 기법의 단점을 보완하기 위하여 실제 변수 분포를 이용한 설계 공간 조절 기법을 개발하였다. 개발된 설계 공간 조절 기법의 효능성을 검증하기 위하여, 최적 기법의

성능을 판단할 때 널리 사용되는 19개 테스트 문제에 대하여 개발된 기법을 적용하였다. 그 결과, 개발된 기법은 해가 존재할 가능성이 높은 적절한 공간으로 조절하였으며, 이를 기반으로 개발된 기법을 이용한 최적화 성능이 기존 기법을 이용한 경우보다 높았다.

본 연구에서 개발된 기법들의 효용성을 검증하기 위하여, 재사용 무인 우주비행체에 대한 다학제간 최적 설계에 적용하였다. 우주비행체의 중량은 수정된 Hypersonic Aerospace Sizing Analysis (HASA)를 이용하여 추정하였으며, 재진입 중량을 이용하여 요구 추력 및 엔진 중량을 계산하였다. 수정된 Newtonian 이론 및 Digital DATCOM을 이용하여 공력 특성을 구하였으며, Approximate convective-heating equation을 이용하여 열전달량을 추정하였다. 우주비행체의 궤적은 3자유도 운동방정식을 이용하여 해석하였다. 이와 같이 우주비행체를 해석하기 위하여, 다양한 분석들을 결합하고 다목적 유전 알고리즘을 이용하여 다학제간 최적 설계를 실시하였다. 그 결과 테스트 문제에서와 같이, 개발된 설계 공간 조절 기법을 이용한 다학제간 최적 설계 결과가 기존의 기법을 사용한 것 보다 뛰어남을 확인하였다.

재사용 무인우주비행체 성능에 영향을 끼치는 형상 정보를 추출하여 최적 형상이 높은 성능을 나타내는 이유를 분석하기 위하여, 분산 분석 및 Parallel chart, 자기 조직화 지도와 같은 데이터 마이닝(Data mining) 기법을 사용하였다. 데이터 마이닝 결과를 토대로, 중량과 열전달량은 Trade-off 관계에 있는 것을 확인하였으며 기수 반경 및 전체 길이, 뿌리

시위 길이가 우주비행체 성능에 영향이 큰 변수임을 확인하였다.

주요어 : 재사용 무인 우주비행체, 개념설계, 다학제간 최적설계, 다학제간 분석, 시간 간격 조절, 설계 공간 조절

학 번 : 2017-38109